APPLICATION OF NANOCARBON MATERIALS FOR LONG-TERM RELIABILITY IMPROVEMENT OF COPPER METALLIZATION

PLOYBUSSARA GOMASANG
Student ID: NB17508
Major: Functional Control Systems

Supervisor
Prof. Dr. Kazuyoshi Ueno

A thesis submitted in fulfilment of
the requirements for the award of the degree of
Doctor of Philosophy

Shibaura Institute of Technology

CANDIDATE’S DECLARATION

It is hereby declared that this thesis or any part of it has not been submitted elsewhere for the award of any degree or diploma.

Signed: ______________________

(Ploybussara Gomasang)

Student No.: NB17508

Certified by: ______________________

(Prof. Dr. Kazuyoshi Ueno)

Dedicated

To

My family and my supervisor

Acknowledgements

Undertaking a Ph.D. at Shibaura Institute of Technology (SIT), Japan, has been a truly life-changing experience for me and here I sincerely thank many people without their support and guidance this work would not archived smoothly.

Above all, I would like to express the deepest appreciation to my supervisor, ***Prof. Dr. Kazuyoshi Ueno****, Department of Electronic Engineering (SIT), Japan, for all the support and advice that he provided me during this period, while I have taken this research at SIT and also the time I spent in Japan. Without his guidance and constant feedback, this Ph.D. would not have been achievable.*

Also, I would like to express my deepest gratitude to ***Prof. Shinji Yokogawa*** *(The University of Electro-Communications, UEC),* ***Prof. Hiroki Ago and his group*** *(Kyushu University),* ***Prof. Susumu Okada and his group*** *(University of Tsukuba), and* ***Dr. Nataliya Nabatova-Gabain and Ms. Yoko Wasai*** *(Horiba Techno Service) for their collaborations and fruitful discussions on some topics related to my research.*

I am grateful to ***Prof. Hiroyasu Ishikawa*** *(SIT),* ***Prof. Tadashi Maeda*** *(SIT),* ***Prof. Kentaro Kyuno*** *(SIT),* ***Prof. Eiichi Kondoh*** *(University of Yamanashi), and* ***Prof. Shinji Yokogawa*** *(UEC) for their kind review of my dissertation.*

Also, I would like to express my gratitude to ***Assoc. Prof. Dr. Rardchawadee Silapunt*** *(King Mongkut's University of Technology Thonburi) for being such an inspiration and all the support throughout my education.*

I gratefully acknowledge the funding which I received towards my doctoral course at SIT from ***the Hybridge Twinning program*** *(SIT, for the 1st year),* ***the Ministry of Education, Culture, Sports, Science and Technology*** *(MEXT) scholarship from Japanese government,* ***Core Research for Evolutional Science and Technology*** *(CREST) Grant Number JPMJCR1532 from the Japan Science and Technology Agency (JST), and* ***SIT Research Center for Green Innovation.***

I am thankful to ***Mrs. Mikiko Nikami****,* ***all members of Nanoelectronic Laboratory*** *(SIT),* ***all friends****,* ***and all concerned*** *for their help during my studying.*

Special thanks to ***my parents****, my beloved* ***Tony****, and the lovely* ***Kalour group*** *for continuous encouragement provided to me.*

Finally, thanks to myself for all the continued efforts in undertaking this research.

Abstract

Semiconductor memory (SM) devices, which can be used as storage media in various applications, have been extensively developed. Because of the rapid increase of digital recording in the world, SM devices are also expected to use for long-term storage of valuable digital data over 100 years. Regarding advanced SM technologies, copper (Cu) has been widely used as interconnect and bond pad material in place of Al to enhance the electrical conductivity and current endurance. Therefore, the long-term reliability of Cu used in SMs is a serious concern for the long-term storage application (>100 years). A potential cause for the failure of long-term data storage is Cu oxidation due to moisture. To avoid Cu oxidation, an impermeable thin film coat can be used. Nanocarbon materials, such as graphene and amorphous carbon (a-C) composites, are excellent candidates due to their small atomic radius of carbon. In the beginning, high-quality large-grained graphene was studied its potential and issues in preventing the Cu surface from oxidation in principle because its forming temperature is still high and not compatible with the current LSIs fabrication. Then, the properties of room-temperature nitrogen-doped a-C (a-C:N) were investigated and expected as a practical method to maintain the Cu surface from oxidation for more than 100 years. Before improving the long-term resistance of Cu against oxidation due to moisture, the effects of Cu oxidation on the sheet resistance were studied under accelerated conditions using a temperature humidity storage (THS) test. In addition, the dependency of Cu oxidation on the temperature and humidity was studied, then, the prediction model of Cu lifetime and its important parameters were derived. The Cu lifetime against humidity was estimated based on the proposed prediction model.

Large-grain single-layer graphene (SLG) was deposited by high-temperature chemical vapor deposition (CVD) for coating on the Cu surface. SLG was demonstrated the potential as an atomic-layer barrier against moisture. The THS test shows that large-grain SLG protects large areas of the Cu surface and only areas with grain boundaries and defects were oxidized.

To avoid the Cu oxidation in areas with grain boundaries and defects, stacked SLG layers, that is, double-layer graphene (DLG) and triple-layer graphene (TLG), were fabricated. The DLG- and TLG-coated Cu samples were tested and compared with bare Cu without a barrier and SLG-coated Cu samples. The results of the Raman and X-ray photoelectron spectroscopy (XPS) measurements indicate that the SLG grain boundaries and defects enhance the Cu oxidation due to

the formation of galvanic cells during long-term THS tests. However, DLG can be used to solve this issue. It can be used to cover the areas of SLG grain boundaries and prevent galvanic corrosion during the THS test. In addition, TLG can be used to protect the Cu surface, ensuring the efficiency of graphene in protecting the sample surface from oxidation due to moisture.

However, it is still difficult to apply graphene as moisture barrier of Cu metallization in current LSIs fabrication because of the high-temperature deposition of graphene. Therefore, a-C:N was studied as an alternative nanocarbon material that can be simply deposited by sputtering at room temperature. The THS test results show that a-C:N with an Ar:N_2 ratio of 90:10 can preserve the sheet resistance of an a-C:N/Cu sample for ~400 years (at 27°C/60% RH) based on the proposed prediction model. The XPS depth profiles obtained after the THS test confirm the excellent efficiency of a-C:N in preventing Cu oxidation due to moisture.

This work provides promising guidelines for the improvement of the long-term reliability of Cu metallization used in advanced SM devices and thus increase their lifetime for the storage of valuable digital data over 100 years.

Contents

Chapter

List of Figures

List of Tables

List of Publications

[Journal papers]

1. **P. Gomasang** and K. Ueno, “Efficient moisture barrier of nitrogen-doped amorphous-carbon layer by room temperature fabrication for copper metallization,” Jpn. J. Appl. Phys. **59**, SLLD03 (2020).
2. T. Murota, T. Mimura, **P. Gomasang**, S. Yokogawa, and K. Ueno, “Humidity reliability of commercial flash memories for long-term storage,” Jpn. J. Appl. Phys. **59**, SLLC01 (2020).
3. **P. Gomasang**, K. Kawahara, K. Yasuraoka, M. Maruyama, H. Ago, S. Okada, and K. Ueno, “A novel graphene barrier against moisture by multiple stacking large-grain graphene,” Sci. Rep. **9**, 3777 (2019).
4. **P. Gomasang**, S. Ogiue, S. Yokogawa, and K. Ueno, “Lifetime prediction model of Cu-based metallization against moisture under temperature and humidity accelerations,” Jpn. J. Appl. Phys. **58**, SBBC01 (2019).
5. **P. Gomasang**, T. Abe, K. Kawahara, Y. Wasai, N. Nabatova-Gabain, N. T. Cuong, H. Ago, S. Okada, and K. Ueno, “Moisture barrier properties of single-layer graphene deposited on Cu films for Cu metallization,” Jpn. J. Appl. Phys. **57**, 04FC08 (2018).

[International conference papers]

1. **P. Gomasang**, T. Murota, and K. Ueno, “Nitrogen-doped amorphous-carbon as efficient moisture barrier on copper,” Ext. Abstr. Advanced Metallization (ADMETA) Conference, Tokyo, Japan, October 2019, p. 100.
2. T. Murota, T. Mimura, **P. Gomasang**, S. Yokogawa, and K. Ueno, “Humidity reliability of commercial flash memories for long-term storage,” Ext. Abstr. Advanced Metallization (ADMETA) Conference, Tokyo, Japan, October 2019, p. 86.
3. **P. Gomasang** and K. Ueno, “Amorphous-carbon barrier against moisture for copper metallization and effects of CF_4 plasma treatment,” Ext. Abstr. International Conference on Solid State Devices and Materials (SSDM), Nagoya, Japan, September 2019, p. 717.

4. **P. Gomasang**, K. Kawahara, H. Ago, and K. Ueno, “Stacked graphene layers for efficient moisture barrier in Cu metallization,” Ext. Abstr. Advanced Metallization (ADMETA) Conference, Beijing, China, October 2018, p. 9-2.
5. **P. Gomasang**, S. Ogiue, S. Yokogawa, and K. Ueno, “Temperature and humidity accelerations to establish lifetime prediction model for Cu-based metallization,” Ext. Abstr. International Conference on Solid State Devices and Materials (SSDM), Tokyo, Japan, September 2018, p. 447.
6. **P. Gomasang**, S. Ogiue, S. Yokogawa, and K. Ueno, “Oxidation structure change of copper surface depending on accelerated humidity,” Ext. Abstr. IEEE International Interconnect Technology Conference (IITC), Santa Clara, USA, June 2018, p. 112.
7. **P. Gomasang**, T. Abe, S. Ogiue, H. Ura, S. Yokogawa, and K. Ueno, “High temperature and high humidity accelerations to estimate the lifetime of Cu metallization for LSIs,” Abstr. The 13th International Conference on Ecomaterials (ICEM), Bangkok, Thailand, November 2017, p. 90.
8. **P. Gomasang**, K. Kawahara, H. Ago, and K. Ueno, “Moisture barrier properties of single-layer and double-layer graphene on Cu film,” Ext. Abstr. Advanced Metallization (ADMETA) Conference, Tokyo, Japan, October 2017, p. 124.

[Domestic conference papers]

1. **P. Gomasang**, T. Murota, and K. Ueno “Moisture barrier properties of nitrogen-doped amorphous-carbon coating on Cu film surface” 7th Green Innovation Symposium, Tokyo, February 2020, p. 163.
2. **P. Gomasang** and K. Ueno “Amorphous-carbon barrier against moisture for Cu metallization,” The 80th JSAP autumn meeting, Sapporo, September 2019. p. 15-116.
3. **P. Gomasang**, K. Kawahara, H. Ago, and K. Ueno, “The improved moisture barrier of graphene coating on Cu film surface,” Tokyo, 6th Green Innovation Symposium, February 2019, p. 95.
4. **P. Gomasang**, S. Ogiue, S. Yokogawa, and K. Ueno, “Lifetime prediction of humidity resistance on Cu-based metallization for long-term storage,” Tokyo, ADMETA satellite workshop, November 2018. p. 66

[Awards]

1. **Silver Poster Award** in 7th Green Innovation Symposium held at Shibaura Institute of Technology, February 18, 2020.
2. **Outstanding Oral Presentation Award** in 13th International Conference on Ecomaterials held at Knowledge Exchange for Innovation Center, Bangkok, Thailand, November 19-23, 2017.

CHAPTER 1

INTRODUCTION

1.1. Overview

In the era of information technology (IT), most of the information, including images, music, videos, and books or magazines, is published and preserved in digital form, leading to the rapid growth of the demand for digital data storage. Therefore, various types of storage media have been developed and are expected to be used for the long-term storage of digital data. Electronic data storage devices, known as the semiconductor memory (SM) devices, are being developed to meet the growing needs of consumers. Because of their advantages, these devices have been applied in various electronics and are expected to be used in place of traditional magnetic storage devices for the long-term storage of digital data. Thus, it is important to improve the long-term storage reliability of SM devices.

This work focuses on the improvement of the long-term reliability of copper (Cu) metallization because they have been used as conductive materials in place of conventional Al metallization [1–4]. The main objective of this research is to prevent the Cu oxidation due to moisture by applying a nanocarbon material coating on the Cu surface as a moisture barrier. This approach has been implemented in this research to reach the goal of long-term protection of the Cu surface from oxidation. This approach is promising regarding the improvement of the long-term reliability of SM devices.

In this chapter, the background, including the history of digital data storage, problems, and critical issues, is provided, and the methods are introduced. Moreover, the essential properties of nanocarbon materials are discussed to explain why they can be adopted to reach the goal of this study.

1.2. History of digital data storage

Figure 1.1 shows a typical nonvolatile memory including magnetic, optical, and semiconductor memories. Beginning from the magnetic hard disk drive (HDD) memory, it was developed and launched for the first time over half of a century ago by IBM in 1965 [5]. The HDD can store and retrieve digital data by controlling the magnetization direction of magnetic media. It was developed for operation in personal computers in 1980 [6]. Subsequently, the performances of HDDs have continuously been improved and the areal storage density has been updated based on magnetic recording, which is commonly used for the long-term storage of digital data on desktop computers and computer servers as well as for the preservation of data for external use on portable HDDs.

Subsequently, optical memories were developed to record and transfer digital data in a more convenient way and increase the number of users that can access data storage technology at a cheaper price. Data can be stored on optical discs by means of laser irradiation of a plastic plate coated with an optical recording material. There are various types of optical discs such as compact discs (CDs) including write-once media, read-only memory (CD-ROM) and rewritable media; digital video discs including read-only and erasable types; Blu-ray discs. The CD was firstly launched in 1982 for the distribution of music and was continually developed for other applications [7]. Nowadays, CD-ROMs are rarely used to store computer software because the new generation of laptops does not provide an optical drive.

HDD

Optical media

Semiconductor memory

Figure 1.1. Nonvolatile storage devices

In today’s modern electronics, the use of SM devices, also known as memory chips, is rapidly increasing on the entire IT market to meet the demands of digital data storage. The existing design in which several transistors are combined on a single integrated circuit (IC) can be classified into as large-scale integrated (LSI) or very-large-scale integrated (VLSI) memories depending on the number of transistors (>1,000 or >100,000 per chip, respectively). The great evolution of ICs in terms of the size is based on Moore’s law. Nonvolatile SMs can be categorized into two types: mask-programmed read-only memory with data programmed during manufacturing and programmable read-only memory (PROM) with data programmed once by the user. Moreover, two types of erasable PROMs have been developed by using ultraviolet light and electrical charge (EEROM) to erase data. The further development of EEROMs led to the invention of the flash memory, which was introduced in 1980 [8]. The flash memory can be electrically rewritten and erased. At present, it has been widely used in various applications such as in universal serial bus flash drives, secure digital (SD) memory cards used to store data in digital cameras and cellphones, and solid-state drives (SSDs), representing the newest flash memory type used in the new generation of laptops and many other applications.

Based on the comparison between the SM and traditional HDD, the SM overcomes all limitations of the HDD with respect to noise, speed, size, and power consumption, except for the capacity and cost [9]. Because the SM requires no complex mechanical systems to store and access data, it will be easier to read the stored data electrically even the read/write system will be lost in the future like “β-system” in the past magnetic recording. The SM devices are used in a variety of small electronic products because of their small size. However, commercial SM devices are very expensive (per GB) because they are newer and harder to manufacture than traditional HDDs. Based on reports on the life expectancy (LE) of data, HDDs have the LE of ~1–7 years depended on the manufacturer [10,11]. The LE of SM devices, including flash drives and SSDs, measured in terms of the mean time to data loss (MTTDL) is ~10–12 years; subsequently, the data start to evaporate [9,11]. The comparison between the SM and HDD is shown in Table 1.1.

Because the storage capacity of SM devices has continually been increased, these devices are expected to replace traditional HDDs as media for the long-term storage of digital data. Therefore, the long-term storage reliability of SM devices should be analyzed and improved.

Table 1.1. Feature comparison between SM and HDD

Parameter	Semiconductor memory (SM)	Hard disk drive (HDD)
Record	Electrical	Magnetic
Recording system	Relatively simple	Mechanically complex
Speed	Faster	Slower
Size	Smaller/thinner	Larger
Power consumption	Lower	Higher
Cost	More expensive per GB	Cheaper per GB
Capacity	Smaller	Bigger
Life expectancy	~10–12 years (mean time to data loss)	~1–7 years

1.3. Cu metallization used in SM devices: background and issues

An IC chip used in SM devices contains numerous layers including the front-end-of-line (FEOL) and back-end-of-line (BEOL) layers, as shown in Fig. 1.2 [12]. The FEOL is the first portion of ICs including individual components, such as transistors, capacitors, resistors fabricated on a wafer. These components are connected to each other through the stacked layer via metal interconnect (Al, Cu, or W) in the BEOL portion of, as shown in Fig. 1.2. This layer includes contacts, metal interconnects, and dielectric layers. The use of Cu as interconnection and bonding pad material in ICs in place of traditional Al has been extensively studied since 1997 to reduce the resistance of BEOL interconnects and improve the electromigration (EM) reliability based on the metals’ higher electrical conductivity and current endurance of Cu [1–4]. Figure 1.3 shows technology regarding the use of gold wires-Cu pad bonds in an advanced packaging platform [10,11].

Although the storage of digital data on the SMs is becoming more advanced and convenient, the long-term preservation of valuable data is a serious concern. A potential cause of the failures of long-term data storage is Cu oxidation due to moisture [13], leading to an increase in the Cu sheet resistance. To avoid Cu oxidation, an impermeable thinner film coating can be applied to the Cu surface as a moisture barrier.

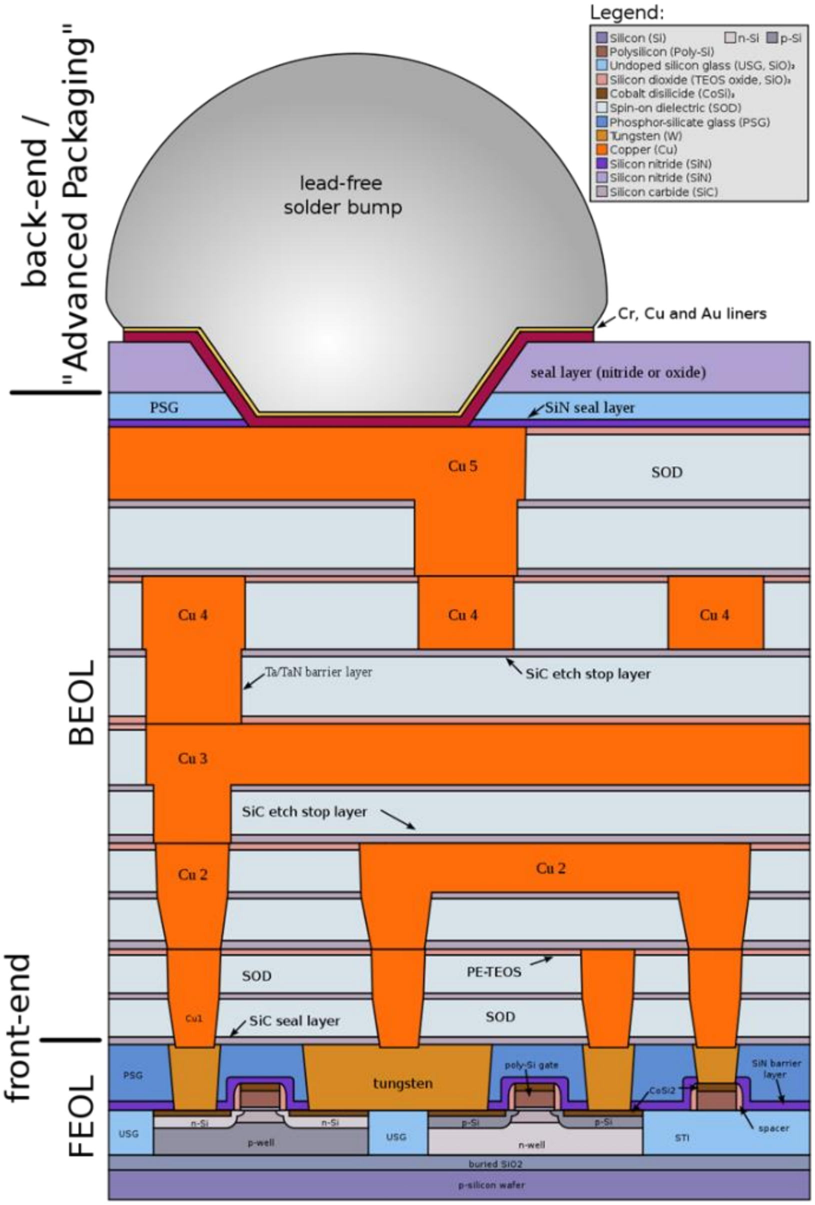

Figure 1.2. Schematic of a chip cross-section with copper interconnect including the FEOL and BEOL layers [12].

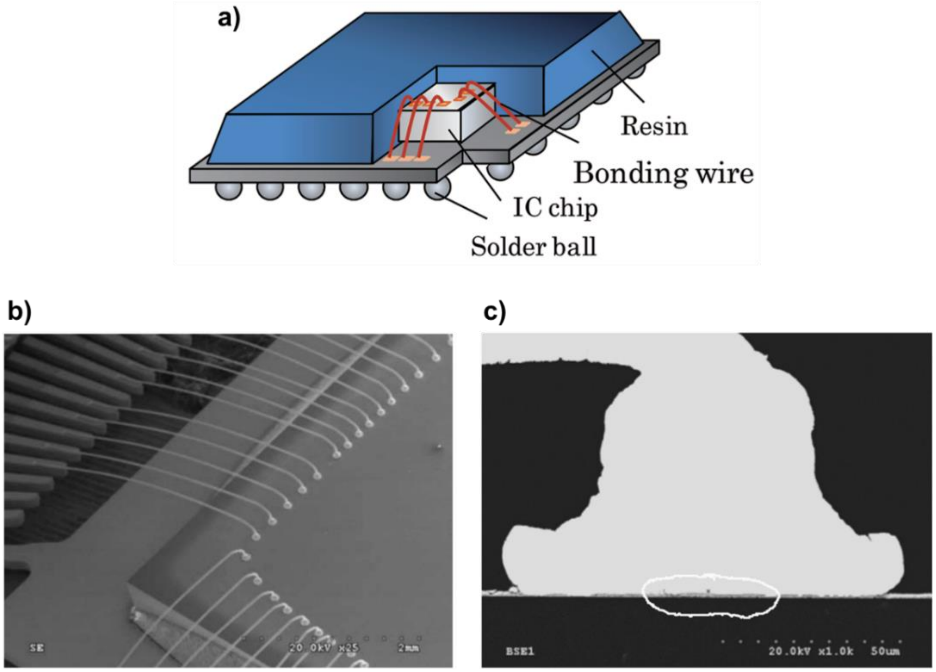

Figure 1.3. (a) Schematic of an LSI package with wire bonding [14] and scanning electron micrographs showing the (b) top view and (c) the cross section of gold wire bonded to the copper pads [15].

1.4. Overall objective

An impermeable thin film coat on the Cu surface can potentially be used to solve the issues described in the previous section. Nanocarbon materials are promising candidates for such a coat on the Cu surface, which is used to improve the long-term resistance of Cu to oxidation due to moisture. Based on previous reports, research on the improvement of the Cu resistance mostly focused on the reliability during operation such as EM and stress-induced voiding [16,17]. However, the long-term storage reliability has rarely been studied and the resistance to humidity has only been reported for Al metallization.

Thus, the first aim of this work is to investigate the effects of temperature and humidity on the change of the Cu surface and study the characteristics of Cu oxidation. In addition, a model for the prediction of the Cu lifetime is proposed and factors affecting failure are discussed.

To improve the long-term storage of SMs and thus preserve digital data for over 100 years, one must study how the Cu oxidation can be avoided. Therefore, the goal of this study is to identify an impermeable thin film coating for the application on the Cu surface to prevent the Cu oxidation. Nanocarbon materials, such as graphene and amorphous carbon (a-C) composite, are the excellent candidates because they have been extensively used in many applications [18–23]. High-quality large-grained graphene has been adopted to investigate the intrinsic moisture barrier properties for coating on the Cu surface in principle and compare them with a Cu surface without coating. However, the deposition of large-grained graphene requires a high temperature (~1000°C), it is not compatible for the current state of LSI fabrication. Then, the application of a-C composite film, which can be deposited at room temperature, has been studied to achieve the goal. The moisture barrier properties of these materials are investigated and compared with a Cu surface without coating.

These studies provide promising guidelines for the improvement of the long-term reliability of Cu used in advanced SM devices to increase their lifetimes over 100 years for the storage of valuable digital data.

1.5. Review of nanocarbon materials: fabrication and properties

According to the small atomic radius of carbon, nanocarbon materials including graphene and a-C composite, can be used as thin barriers in form of coating on the Cu surfaces. Figure 1.4 shows the different structures of graphene and a-C [24]. Graphene is the first candidate, which is used in this work to protect the Cu surface from oxidation due to moisture because of its impermeability and small atom thickness. Other candidates used in this work are a-C and nitrogen (N)-dope a-C (a-C:N) materials. Although a-C and a-C:N materials do not exhibit a crystalline structure such as graphene, they have been used as diffusion barriers in other applications and are compatible with the thermal budget of the present fabrication process.

In this section, the fundamental properties and deposition methods of graphene, a-C, and a-C:N films are introduced and the feasibility of these materials in protecting the Cu surface from oxidation due to moisture is discussed.

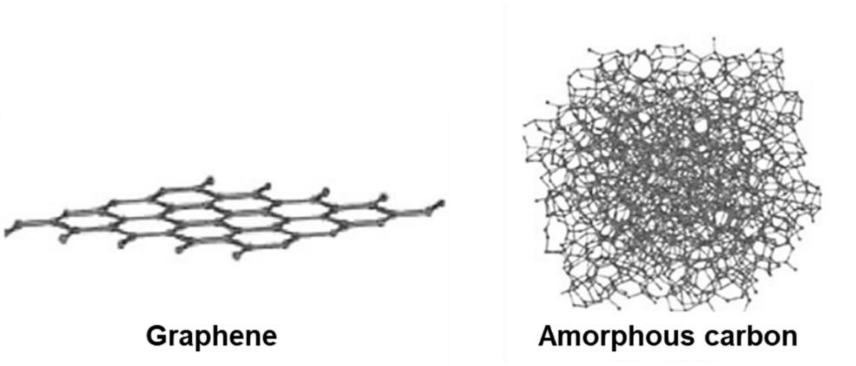

Figure 1.4. Structures of graphene and amorphous carbon [24].

1.5.1. Graphene

Graphene is an allotrope of carbon (C) arranged in a two-dimensional layer of the hexagonal lattice (thickness of one C atom is ~0.34 nm). Graphene can be synthesized with various methods including mechanical and chemical exfoliation from graphite, and (thermal) chemical vapor deposition (CVD) from C-containing gas on a catalytic metal surface. [25–28]. All of synthesis methods have their own advantages and disadvantages depending on the application. The CVD can be used to deposit high-quality graphene films at a relatively high temperature (~1000°C) and ambient or low pressure from various C precursors, such as methane, ethane, and propane, using catalyst metals such as Cu, Ni, and Co [28–30].

Graphene has been used in various applications due to its excellent properties such as the strength, transparency, and electronic properties, etc. Graphene sheets are stronger than steel based on the comparison of materials with in the same thickness and harder than diamonds [31,32]. Despite their strength, they are very flexible and can be stretched by up to 25% and folded [33]. They are highly transparent with white-light adsorption of only 2.3% [34]. Moreover, they exhibit remarkably high thermal and electrical conductivities [35,36]. It has been reported that the impermeability of graphene film prevents even the diffusion of gases [37].

Based on these significant properties, graphene can be used to improve the performance of materials and to replace conventional materials, thus driving the development of new technologies or industries in several fields such as electronics, food, medical, and textile industries. [38–44]. For example, graphene is one of the candidates for interconnect materials because of its lower resistance and higher current endurance against EM compared with Cu [45,46]. It potentially can also be used as an atomically thin barrier against Cu diffusion in Cu interconnects to improve the reliability of time-dependent dielectric breakdown (TDDB) [47].

Based on the fact that they are impermeable and can be used as barriers against gases [37], graphene sheets might be appropriate thin moisture barriers for coating on Cu surfaces to prevent oxidation. Although the high-temperature synthesis approach of graphene is still not compatible with the current BEOL thermal budget, graphene samples with large grains should be deposited at high temperature and investigated to evaluate their potential and principle issues regarding the barrier.

1.5.2. Amorphous carbon and nitrogen-doped amorphous carbon

The a-C is an allotrope of carbon, which form a random network. It contains a mixture composition of diamond-like sp^3 and graphite-like sp^2 bonds and the hydrogen (H) depending on the fabrication process, leading to difference in its physical properties. Figure 1.5 shows a phase diagram including different a-C types [48]. Based on the ratio of sp^2/sp^3 bonds in Fig. 1.5, the dominant sp^3-hybridized bond has a high resistivity, chemical resistance, optical transparency, and high hardness, but is brittle [49,50]. On the other hand, the dominant sp^2-hybridized bond is highly conductive and exhibits properties similar to those observed in graphene.

The a-C layer can be prepared with various methods such as magnetron sputtering from a graphite target, plasma-enhanced CVD, and ion beam deposition. [51–53]. The sputtered a-C in Fig. 1.5 has an sp^2 content of up to 90% (along with sp^3) and it can induce properly higher conductivity than those of other methods. Sputtered a-C has also been reported as a Cu diffusion barrier for advanced Cu interconnects [54].

The a-C:N can be synthesized by applying N gas flow during the a-C fabrication. The a-C:N has been widely studied to improve the a-C properties such as the electrical properties of the a-C layer used in semiconductors and optoelectronic devices and extend to a variety of other applications [55,56]. It has been reported that a-C:N film can be used as diffusion barrier for power device applications [56]. In addition, the use of an a-C:N layer as a diffusion barrier against fluorine (F) atoms has recently been reported based on first-principle simulations [57,58].

Thus, it is an interesting candidate that may be used to prevent the Cu oxidation in this research. Because a-C:N can be synthesized at room temperature, it is more appropriate for the current chip fabrication process.

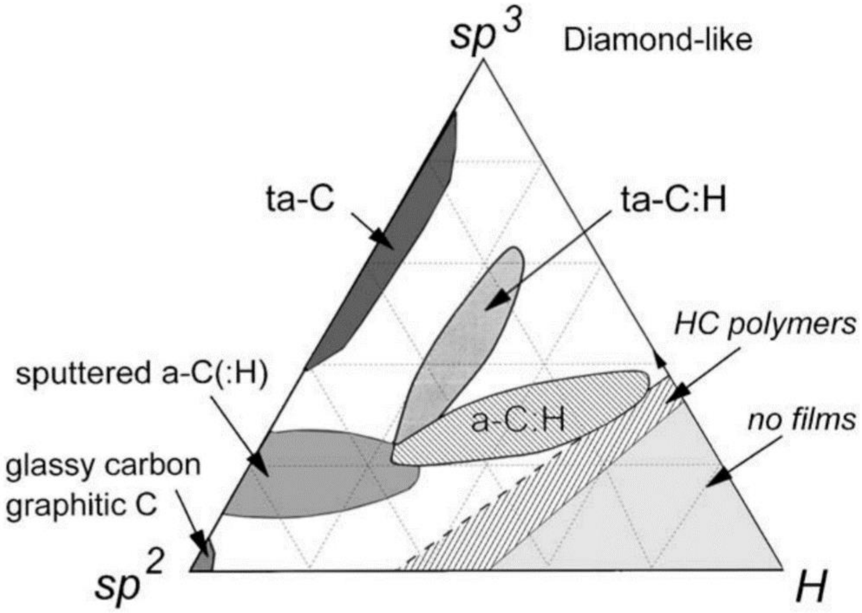

Figure 1.5. Ternary phase diagram showing different amorphous carbon types [44].

1.6. Literature review related to the objective of this research

Regarding the humidity resistance of LSIs, lifetime tests under acceleration conditions was carried out on devices containing Al-based metallization, as shown below. However, there is a lack of lifetime tests of Cu-based metallization and a model for the prediction of the lifetime of Cu metallization against humidity has not been reported yet. Therefore, the Cu oxidation due to moisture should be studied and the Cu reliability against humidity should be improved.

- D. S. Peck et al. [59] studied the effects of the temperature and humidity on the lifetime of Al metallization, which can be used to extrapolate autoclave testing results. They reviewed all data published on humidity testing over the entire stress range, both above and below 85℃/85% relative humidity (RH) condition. Then, they established a practical model for the lifetime extrapolation based on the objective that a model can be fitted all data from the stress conditions less than that of 85°C/85% RH.

Because Cu metallization has been studied for the use in interconnect materials in LSIs, including advanced SM devices [1–4], one of the most serious concerns regarding the long-term reliability is Cu oxidation, as described in the previous sections. The use of a conductive thin film, such as graphene, coated on the Cu surface as a moisture barrier, has been proposed. By using conventionally synthesized single-layer graphene (SLG) on a Cu foil (CVD method), the application of SLG has been studied, which then was adapted to various fields. Based on the impermeability and stability of graphene, SLG has been reported to be an ultra-thin coating material, which can be used to protect the substrate from corrosion, preserving the efficiency of the product, and even inducing an interface diffusion resistance, as described in the literature below.

- L. Nilsson et al. [60] reported the effectiveness of SLG coating on a platinum (Pt) surface protecting against O_2 exposure. Based on experiments and simulations, they also demonstrated that the SLG layer remains intact, even under harsh conditions of H exposure at 2,000 K (1,727°C) and prevents the direct interaction between the Pt surface and H atoms.

- Y. Zhao et al. [61] reported the efficiency of impermeable and transparent SLG, which was deposited on Cu foil using CVD and transferred to a silver (Ag) surface for optical applications. They reveal that SLG inhibits the corrosion of the Ag surface, including electrochemical reactions in salt and strong oxidizing solutions. The SLG/Ag samples maintained their optical properties under harsh conditions.

- S. Chen et al. [62] for the first time reported the use of graphene directly grown on Cu foil to prevent the oxidation in air after heating at 200°C for up to 4 h. In addition, they investigated the efficiency of a SLG coat on a Cu surface after exposure to aqueous solution of H_2O_2. The results indicated that only a few spots of SLG/Cu were attacked after 45 min H_2O_2 exposure and the majority of the Cu surface was still covered with SLG. They also suggested further improvement of large-grained and defects-free graphene for the use in nanoelectronic devices.

- M. Schriver et al. [63] reported anticorrosion and antioxidation surface treatments of SLG, which was deposited on Cu foil using CVD, used for Cu and silicon (Si) substrates. They found that SLG provides effective short-term oxidation protection (minutes to hours) for Cu and Si surfaces under heating in atmosphere at 250℃ and 185℃ and low humidity. Based on long-term tests, they found that O_2 and H_2O infiltrated the graphene through defects and oxidized or corroded the surface underneath the graphene.

- F. Zhou et al. [64] reported that SLG deposited on Cu foil using CVD can be used for short-term protection from oxidation under an ambient atmosphere at room temperature. They revealed that the SLG-coated Cu foil was inhomogeneous and the SLG grain size only reached a few micrometers. The corrosion of SLG/Cu could be enhanced because of the conductive nature of SLG.

- M. Galbiati et al. [65] reported a comparative real-time study showing the evolution of Cu oxide in SLG/Cu and hBN/Cu foils deposited using CVD. They showed that both graphene and hBN coatings provide good protection against Cu oxidation over the short time (30 min at <250℃), The SLG coating performed better than hBN because of its higher quality. However, the hBN coating eventually outperformed the SLG coating in long-term tests, even if the grain size of SLG was larger than that of hBN. They revealed that the grain size of SLG is too small to inhibit Cu oxidation and that the SLG grain boundary area induces high Cu oxidation during long-term tests.

- L. Li et al. [47] reported the multi-transfer of 1–3 layers of SLG with a grain size of ~15 µm, which was deposited using CVD on Cu foil as a Cu diffusion barrier for Cu interconnects. The test was conducted using TDDB and the results were compared with those obtained for a conventional TaN barrier and multilayer graphene deposited on Ni foil using CVD. Based on three stacked SLG layers, it indicated three times improvement of the mean time-to-fail (MTTF) could be three times improved compared with conventional TaN. The MTTFs of the structure were shorter after reducing the transferred SLG. Moreover, multilayer graphene (MLG) exhibited a worse MTTF than SLG due to the higher density of disorders in MLG. In addition, the use of larger-grained SLG was suggested to further improve the Cu diffusion barrier.

Based on the identification of other conductive materials that can be synthesized at low temperature, a-C and a-C:N materials are interesting candidates.

- B.-S. An et al. [54] reported the barrier performance of a sputtered a-C layer deposited by DC magnetron sputtering on SiO_2 in blocking Cu diffusion into the SiO_2 substrate during annealing at 400°C for 10 h. They reported that a thin a-C barrier layer (0.75 nm) prevents Cu diffusion into the SiO_2 layer. The results were confirmed using depth profiles and transmission electron microscopy (TEM). The results indicate a considerable improvement of the reliability of advanced Cu interconnects.

- M. Stelzer et al. [56] reported the electrical characteristics and reliability of low-temperature sputtered a-C and a-C:N at ~400°C as interface materials with respect to Si and compare them with those of conventional TiSi–Si contacts. Moreover, the N doping of a-C provided a lower resistivity and improved the stability of the a-C layer. The tests were conducted on a Schottky diode structure. Because the TiSi contacts had a low thermal stability, they could be degraded at high temperature, especially during electrostatic discharge, leading to the diffusion and migration of TiSi in Si. This study revealed that there were no diffusion of sputtered a-C and a-C:N after 10^9 of stress pulses. They also mentioned that the diffusion barrier properties of a-C make it a good alternative interconnect material to phase change material in 3D XPoint memories.

- H. Park et al. [58] studied the application of a-C as hard mask for the future fabrication of integrated semiconductor devices. They reported the effects of N doping of the a-C layer on the diffusion of F atoms based on first-principles density functional theory calculations.

They reported that the F atom formed bonds to the surrounding C atom rather than the N atom due to the electrostatic repulsion between N and F atoms. The results indicated that the diffusion barriers of the F atom passing the N atom are extremely large. These large barriers are mainly due to the electrostatic repulsion between N and F atoms originating from the strong electronegativity of both atoms. These findings revealed that N doping can enhance the diffusion barrier against F atoms leading to the suppression of F diffusion.

1.7. Aim and approach to reach the goal

Before improving the long-term reliability of Cu against oxidation due to moisture for over 100 years, the effects of Cu oxidation on the sheet resistance change were studied for the entire stress range of the temperature-humidity storage (THS) test, ~85℃/85% RH, which is the standard test for electronic packages. The depth profile of the Cu oxidation was obtained using Ar+ etching and X-ray photoelectron spectroscopy (XPS) measurements to study the Cu oxidation characteristics. The change in the sheet resistance due to Cu oxidation was measured and used to formulate a model for the prediction of the Cu lifetime depending on the humidity, which can be applied to study the factors accelerating the Cu oxidation.

Based on the literature review described in the previous section, many researchers indicated the impermeability of SLG deposited on Cu foil using CVD [47,60–65]. However, the efficiency of high-quality large-grained SLG has not been reported. In this work, the efficiency of large-grained SLG deposited on an epitaxial Cu surface using CVD is demonstrated in principle. Based on THS testing (at 85℃/85% RH for 25 h corresponding to ~100 years at 27℃/60% RH), it was expected that the higher quality and larger grain size of the SLG films will lead to the preservation of larger Cu surface areas compared with the commercial SLG deposition on Cu foils. In addition, a non-uniform SLG sample with a mixed composition of a-C and SLG was investigated to study its effect on the Cu-oxidation by using an ellipsometer after THS testing.

To improve the reliability of the SLG-coated Cu surface, the application of the stacked SLG was studied. In this work, the multiple stacking of SLG is proposed, as double-layer graphene (DLG) and triple-layer graphene (TLG) to cover the grain boundaries and defects underneath the SLG. The DLG and TLG can be fabricated by multi-transfer methods using CVD-SLG/Cu samples. The efficient moisture barrier of stacked graphene was investigated after THS testing using XPS measurement and the results were compared with those obtained for SLG/Cu and bare Cu samples.

Because the high-temperature deposition of SLG is not compatible with the current thermal budget of the fabrication process of IC chips, a-C and a-C:N materials deposited at room temperature on the Cu surface were investigated after the THS test to study the moisture barrier properties of these films. Sheet resistance change measurements and surface morphology observations using scanning electron microscope (SEM) were performed. Moreover, XPS depth profiling was carried out to confirm the moisture barrier properties of the layer.

These studies provide guidelines for the improvement of the long-term reliability of Cu metallization used in advanced SM devices.

1.8. Structure of the thesis

This dissertation is divided into seven chapters, as shown in Fig. 1.6, which can be briefly described as follows:

Chapter 1 consists of the general information and background including the history of digital data storage and critical issues leading to the objective of this research. Explanations of nanocarbon materials, including graphene, a-C, and a-C:N are given. In addition, several previous reports related to the objective are reviewed. The approach to reach the goal of this work is also described in this chapter.

Chapter 2 consists of the detailed explanations of the fabrication processes, tests, and analysis methods. The fabrication methods, including SLG, stacked SLG, and sputtered a-C, and a-C:N, used in this research are described. Details of the THS testing and analysis methods, such as Raman, XPS, SEM, TEM, optical microscope (OM), and four-point probe method for sheet resistance measurement, are also provided in this chapter.

Chapter 3 contains the results of the XPS and sheet resistance measurement, which were used to study the characteristics of surface oxidation of Cu in moisture. The Cu lifetime test was performed under various acceleration conditions of temperature and humidity to derive the acceleration parameters for the lifetime prediction model of Cu against oxidation due to moisture.

Chapter 4 consists of the experiments, results and discussion regarding the moisture barrier properties of high-quality large-grained SLG film coating on the Cu surface after THS test investigated by using OM and XPS. First-principle molecular dynamics simulations and calculations of the activation energy for the diffusion of oxygen (O) atoms through the SLG layer are also described in this chapter. The correlation between the SLG quality and Cu-oxide thickness was determined after the THS test using spectroscopic ellipsometry; a non-uniform SLG film was deposited on the Cu surface.

Chapter 5 comprises the two main experiments, that is, Raman measurement in areas with oxidized Cu on the SLG/Cu surface, showing that Cu oxidation occurred at SLG grain boundaries, XPS measurements indicating that multiple stacking of large-grained SLG films into DLG and TLG can protect the grain boundaries of the SLG film underneath and thus prevent the Cu oxidation during long-term THS test. The mechanism underlying the improvement of the resistance to oxidation based on first-principles simulations for overlapping graphene films are also described in this chapter.

Chapter 6 consists of the experimental results obtained for the sputtered a-C:N layer, which can be deposited at room temperature as a barrier against Cu oxidation after THS test. The efficiency of the moisture barrier was investigated using OM, SEM, TEM, and XPS measurements after Ar+ etching to obtain XPS depth profiles. The potential mechanisms of a-C:N layer against O diffusion are also discussed in this chapter.

Chapter 7 summarizes all results of this research. The conclusions are drawn. Future prospects of this work are also provided.

All references are listed at the end of each chapter.

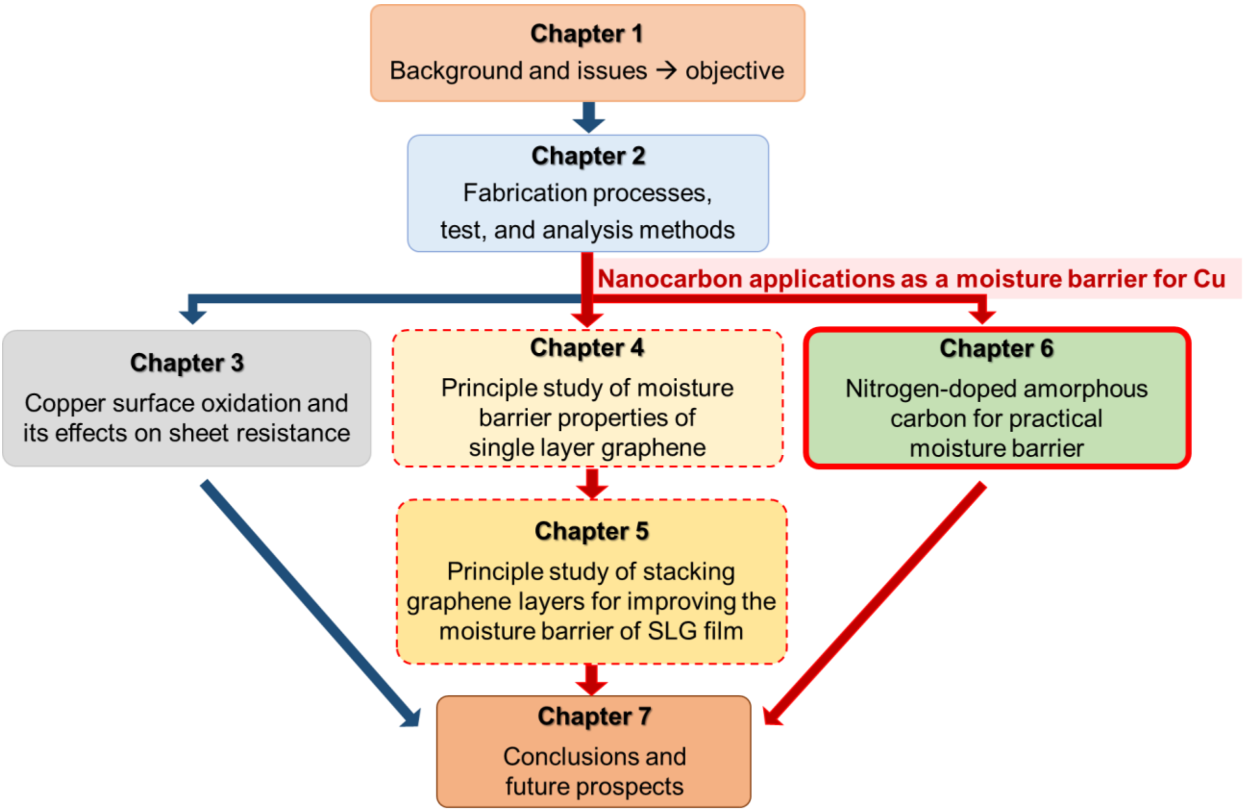

Figure 1.6. Flowchart of the dissertation

References

[1] H. B. Lee, J. W. Hong, G. J. Seong, J. M. Lee, H. Park, J. M. Baek, K. I. Choi, B. L. Park, J. Y. Bae, G. H. Choi, S. T. Kim, U. I. Chung, J. T. Moon, J. H. Oh, J. H. Son, J.H. Jung, S. Hah, and S.Y. Lee, Tech. Dig. IEEE Int. Interconnect Tech. Conf., 2007, p. 64.

[2] M. R. Baklanov, C. Adelmann, L. Zhao, and S. De Gend, ECS J. Solid State SC. **4**, Y1 (2015).

[3] L. L. Jinzhi, C. Yan, W. Bisheng, L. Xiaomin, F. Chao, H. Younan, Proc. IEEE Int. Conf. on Electronic Packaging Technology (ICEPT), 2018, p. 1546.

[4] Y. L. Cheng, C. Y. Lee, and Y. L. Huang, Copper Metal for Semiconductor Interconnects. Noble and Precious Metals–Properties, Nanoscale Effects and Applications (2018).

[5] T. G. Leary, 305 RAMAC; Random Access Method of Accounting and Control. Manual of operation (International Business Machines Corporation, Santa Clara, CA, 1957).

[6] IBM 3380 Direct Access Storage Description and User's Guide (International Business Machines Corporation, San Jose, CA, 1981) 2nd Ed.

[7] R. Jones, Data Process. **28**, 295 (1986).

[8] Flash Memory Guide (Kingston Technology Corporation, Fountain Valley, CA, 2012).

[9] H. Kaneko, T. Matsuzaka, and E. Fujiwara, Proc. IEEE Pacific Rim Int. Symp. on Dependable Computing (PRDC), 2008, p. 281.

[10] R. D. Weiss, Final report to the National Archives and Records Administration, Delivered by Arkival Tech. Corp. under contract requirement NAMA-01-F-0061, 2002, pp.1–94.

[11] B. M. Lunt, Proc. of Archiving, 2011, p.29.

[12] G. Z. Morgan, An Agile Cause Analysis Using JMP. 2017, https://community.jmp.com/t5/Discovery-Summit-2017/An-Agile-Cause-Analysis-Using-JMP/ta-p/44067. Accessed 17 Sep. 2020.

[13] S. Yokogawa and K. Kunii, Jpn. J. Appl. Phys. **57**, 07MG01 (2018).

[14] T. Uno, T. Oyamada, T. Yamada, and T. Oda, Nippon Steel & Sumitomo Metal Tech. Rep. **117**, 3 (2015).

[15] J. N. Aoh and C. L. Chuang, J. Electron. Mater. **33**, 300 (2004).

[16] S. Yokogawa and Y. Kakuhara, Jpn. J. Appl. Phys. **50**, 05EA02 (2011).

[17] S. Yokogawa, Jpn. J. Appl. Phys. **53**, 05GA03 (2014).

[18] S. Syama and P. V. Mohanan, Nano-Micro Lett. **11**, 6 (2019).

[19] T. H. Han, Y. Lee, M. R. Choi, S. H. Woo, S. H. Bae, B. H. Hong, J. H. Ahn, and T. W. Lee, Nature Photon. **6**, 105 (2012)

[20] A. K. Sundramoorthy and S. Gunasekaran, Trac-Trend. Anal. Chem., **60**, 36 (2014).

[21] D. Pierleoni, Z. Y. Xia, M. Christian, S. Ligi, M. Minelli, V. Morandi, F. Doghieri, V. Palermo, Carbon **96**, 503 (2016).

[22] B. S. Kwon, J. S. Kim, N. E. Lee, and J. W. Shon, J. Electrochem. Soc. **157**, D135 (2010).

[23] W. Liu, D. Mui, T. Lill, M. Wang, C. Bencher, M. Kwan, and W. Yeh, Proc. SPIE Int. Soc. Opt. Eng., 2003, p.841.

[24] M. Noked, A. Soffer, and D. Aurbach, J. Solid State Electrochem. **15**, 1563 (2011).

[25] M. Cai, D. Thorpe, D. H. Adamsonb, and H. C. Schniepp, J. Mater. Chem. **22**, 24992 (2012).

[26] A. A. Green and M. C. Hersam, Nano Lett. **9**, 4031 (2009).

[27] X. Li, W. Cai, J. An, S. Kim, J. Nah, D. Yang, R. Piner, A. Velamakanni, I. Jung, E. Tutuc, S. K. Banerjee, L. Colombo, R. S. Ruoff, Science **324**, 1312 (2009).

[28] H. Ago, K. Kawahara, Y. Ogawa, S. Tanoue, M. A. Bissett, M. Tsuji, H. Sakaguchi, R. J. Koch, F. Fromm, T. Seyller, K. Komatsu, and K. Tsukagoshi, Appl. Phys. Express **6**, 075101 (2013).

[29] J. K. Wassei, M. Mecklenburg, J. A. Torres, J. D. Fowler, B. C. Regan, R. B. Kaner, and B. H. Weiller, Small **8**, 1415 (2012).

[30] A. Cabrero-Vilatela, R.S. Weatherup, P. Braeuninger-Weimer, S. Caneva, and S. Hofmann, Nanoscale **8**, 2149 (2016).

[31] C. Lee, X. Wei, J. W. Kysar, and J. Hone, Science **321**, 385 (2008).

[32] R. Mas-Balleste, C. Gomez-Navarro, J. Gomez-Herrero, and F. Zamora, Nanoscale **3**, 20 (2011).

[33] T. Chen, Y. Xue, A. K. Roy, and L. Dai, ACS Nano **8**, 1039 (2014).

[34] R. R. Nair, P. Blake, A. N. Grigorenko, K. S. Novoselov, T. J. Booth, T. Stauber, N. M. R. Peres, A. K. Geim, Science **320**, 1308 (2008).

[35] A. A. Balandin, S. Ghosh, W. Bao, I. Calizo, D. Teweldebrhan, F. Miao, and C. N. Lau, Nano Lett. **8**, 902 (2008).

[36] B. Galindo, S. G. Alcolea, J. Gómez, A. Navas, A. O. Murguialday, M. P. Fernandez, and R. C. Puelles, IOP Conf. Ser.: Mater. Sci. Eng. **64**, 012008 (2014).

[37] J. S. Bunch, S. S. Verbridge, J. S. Alden, A. M. van der Zande, J. M. Parpia, H. G. Craighead, P. L. McEuen, Nano Lett. **8**, 2458 (2008).

[38] R. Mehta, S. Chugh, and Z. Chen, Nano Lett. **15**, 2024 (2015).

[39] N. T. Cuong and S. Okada, Appl. Phys. Lett. **110**, 131601 (2017).

[40] H. Shen, L. Zhang, M. Liu, and Z. Zhang, Theranostics **2**, 283 (2012).

[41] A. N. Banerjee, Glob. J. Nano. **1**, 555552 (2016).

[42] D. Prasai, J. C. Tuberquia, R. R. Harl, G. K. Jennings, B. R. Rogers, and K. I. Bolotin, ACS Nano. **6**, 1102 (2012).

[43] I. U. Unalan, G. Cerri, E. Marcuzzo, C. A. Cozzolino, and S. Farris, RSC Adv. **4**, 29393 (2014).

[44] D. Kongahge, J. Foroughi, S. Gambhir, G. M. Spinks, and G. G. Wallace, RSC Adv. **6**, 73203 (2016).

[45] L. Li, Z. Zhu, T. Wang, J. A. Currivan-Incorvia, A. Yoon, H.-S. Philip Wong, Proc. IEEE Int. Electron Devices Meeting, 2016, p.240.

[46] L. Li, Z. Zhu, A. Yoon, and H.-S. Philip Wong, IEEE Electron Device Lett. **40**, 815 (2019).

[47] L. Li, X. Chen, C. H. Wang, J. Cao, S. Lee, A. Tang, C. Ahn, S. S. Roy, M. S. Arnold, and H.-S. Philip Wong, ACS Nano **9**, 8361 (2015).

[48] J. Robertson, Mater. Sci. Eng. R **37** 129 (2002).

[49] Y. Lifshitz, Diamond Relat. Mater. **8**, 1659 (1999).

[50] A. C. Ferrari, Surf. Coat. Technol. **180 – 181**, 190 (2004).

[51] F. Ferrieu, C. Chaton, D. Neira, C. Beitia, L. P. Mota, A. M. Papon, A. Tarnowka, AIP Conf. Proc. **931**, 99 (2007).

[52] S. Aisenberg and R. Chabot J. Appl. Phys. **42**, 2953 (1971).

[53] R. Pandiyan, N. Delegan, A. Dirany, P. Drogui, M. A. El Khakani, Carbon **94**, 988 (2015).

[54] B.-S. An, Y. Kwon, J.-S. Oh, C. Lee, S. Choi, H. Kim, M. Lee, S. Pae, and C.-W. Yang, ACS Appl. Mater. Interfaces **12**, 3104 (2020).

[55] J. A. Behan, S. N. Stamatin, M. K. Hoque, G. Ciapetti, F. Zen, L. Esteban-Tejeda, and P.E. Colavita, J. Phys. Chem. C **121** 6596 (2017).

[56] M. Stelzer, M. Jung, U. Wurstbauer, A. W. Holleitner, and F. Kreupl, Proc. IEEE Int. Electron Devices Meeting, 2018, p.245.

[57] H. Park, S. Lee, H. J. Kim, D. Woo, S. J. Park, J. M. Lee, E. Yoon, and G. D. Lee, J. Appl. Phys. **125**, 155701 (2019).

[58] H. Park, D. Woo, J. M. Lee, S. J. Park, S. Lee, H. J. Kim, E. Yoon, and G.-D. Lee, Sci. Rep. **9**, 1 (2019).

[59] D. S. Peck, Proc. IEEE Int. Reliability Physics Symposium (IRPS), 1986, pp. 44.

[60] L. Nilsson, M. Andersen, R. Balog, E. Lægsgaard, P. Hofmann, F. Besenbacher, B. Hammer, I. Stensgaard, and L. Hornekær, ACS Nano **6**, 10258 (2012).

[61] Y. Zhao, Y. Xie, Y. Y. Hui, L. Tang, W. Jie, Y. Jiang, L. Xu, S. P. Laua, and Y. Chai, J. Mater. Chem. C **1**, 4956 (2013).

[62] S. Chen, L. Brown, M. Levendorf, W. Cai, S.-Y. Ju, J. Edgeworth, X. Li, C. W. magnuson, A. Velamakanni, R. D. Piner, J. Kang, J. Park, and R. S. Ruoff, ACS Nano **5**, 1321 (2011).

[63] M. Schriver, W. J. Gannett, A. M. Zaniewski, M. F. Crommie, and A. Zettl, ACS Nano **7**, 5763 (2013).

[64] F. Zhou, Z. Li, G. J. Shenoy, L. Li, and H. Liu, ACS Nano **7**, 6939 (2013).

[65] M. Galbiati, A. C. Stoot, D. M. A. Mackenzie, P. Bøggild, and L. Camilli, Sci. Rep. **7**, 1 (2017).

CHAPTER 2

FILM DEPOSITION, TEST, AND METHODOLOGY

2.1. Overview

The main aims of this study were to investigate the Cu-surface oxidation under accelerated Cu-oxidation conditions depending on both the temperature and humidity and demonstrate the moisture barrier properties of graphene and a-C:N respectively, as introduced in the previous chapter, in preventing Cu-oxidation. In this chapter, the research methods are described including the thin-film deposition, which was used for Cu and a-C:N sputtering; CVD of SLG, DLG, and TLG; THS test, and methodological theories.

2.2. Fabrication methods

2.2.1. Substrates cleaning

Two types of substrates were used for the deposition of thin films in this work: SiO_2/Si and Al_2O_3. To study the Cu oxidation and moisture barrier properties of the a-C coat on the Cu surface, SiO_2/Si was used as sample substrate for the deposition of the Cu film layer. The cleaning procedure used for the SiO_2/Si substrate is described below. To demonstrate the efficiency of SLG in preventing Cu oxidation, an Al_2O_3 substrate was used for the growth of an epitaxial Cu layer. Subsequently, large-grain SLG was synthesized on top of the Cu surface on the Al_2O_3 substrate after cleaning by Ago group (Kyushu University).

Cleaning of the SiO_2/Si substrate before the deposition of the Cu film:

1) Soaking of the substrate in a liquid containing sulfuric acid (H_2SO_4):hydrogen peroxide (H_2O_2), with a 4:1 volume ratio, and shaking for 10 min
2) Dipping in ultrapure water (twice) to remove chemicals
3) Soaking the substrate in a beaker with ultrapure water and ultrasonication for 5 min
4) Removal of surface water using a N_2 gas gun
5) Baking at ~100°C for 10 min

2.2.2. Magnetron sputter deposition

Magnetron sputter deposition has been widely used for the deposition of thin films of a variety of materials, such as metals, semiconductors, ceramics, and insulators, on different substrates. During the deposition, atoms are ejected from the target surface by bombarding it with Ar+ gas at low pressure. Two magnetron sputtering methods were used in this work: direct current (DC) magnetron sputtering and radio frequency (RF) magnetron sputtering. The schematic diagram of the DC/RF magnetron sputtering system is shown in Fig. 2.1.

The DC magnetron sputtering can be used for all conductive targets. As shown in Fig. 2.1, the negative probe of a DC power supply is connected to the conductive target, which serves as the cathode. The substrate side acts as the anode. In a low-pressure Ar atmosphere, Ar+ ions are generated and accelerated towards the target (cathode) to eject atoms from the target surface. The sputtered atoms move towards the substrate on the opposite side and are deposited, leading to the formation of a thin film on the substrate surface. A magnetic field generated by a permanent magnet can be used to enhance the ion bombardment and sputtering rate of the system.

The advantage of RF magnetron sputtering is that a thin film can be deposited on both conductive and insulating targets. Because the deposition on insulating materials requires a very high voltage to maintain the discharge between the electrodes, it is impossible to use DC sputtering. A high-frequency alternating current (13.56 MHz) is applied between the cathode and anode to provide induce electron oscillation and thus ionizing collisions and a self-sustained discharge (Fig. 2.1). A matching network is used to optimize the power transfer from the RF source to the plasma. Because of the higher mobility of electrons compared with Ar+ ions, the electrons will reach the target surface fast during the positive half-cycle of the AC signal. Subsequently, the target will be negatively self-biased and induce the Ag+ ions to form like a shell in front of the target. These Ar+ ions bombard the target to eject atoms from its surface during the negative half-cycle, which results in the deposition of atoms on the substrate.

In this work, both DC and RF magnetron sputtering were used for Cu and a-C:N deposition under different conditions, as described below.

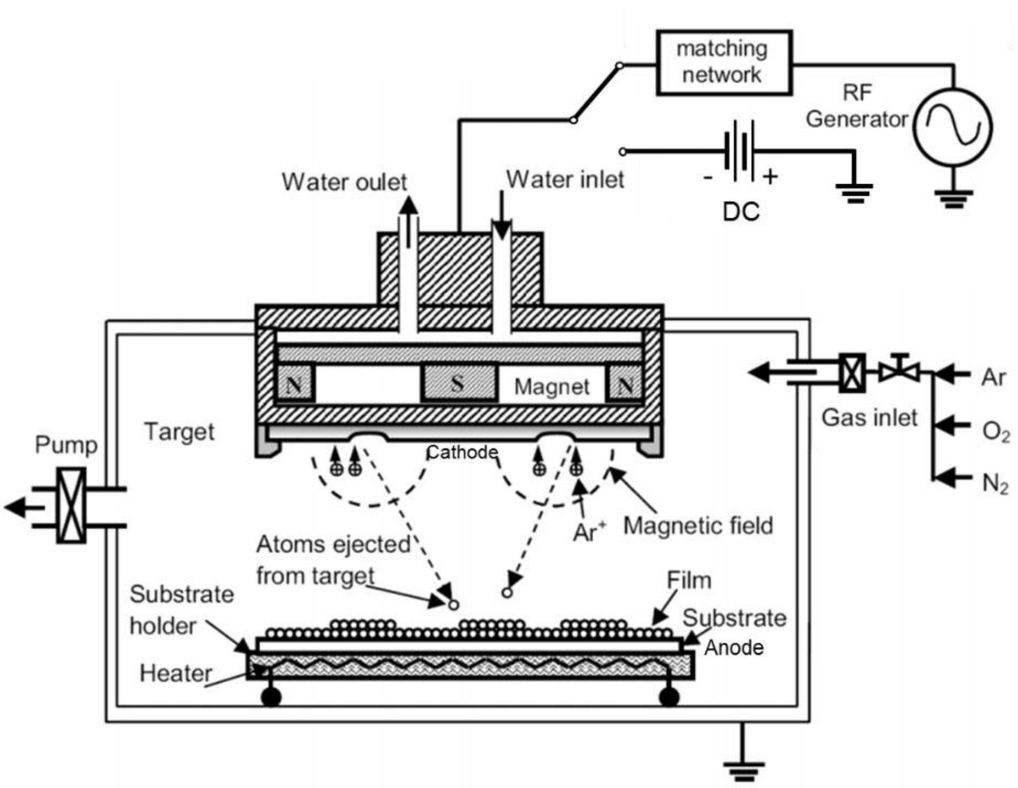

Figure 2.1. Schematic diagram of DC/RF magnetron sputtering system [1].

2.2.2.1. a-C, a-C:N, and Cu sputtering on SiO_2/Si substrate

Firstly, 100 nm thick Cu was deposited on a SiO_2/Si substrate at a power of 300 W in an Ar atmosphere (~0.6 Pa) using DC magnetron sputtering (Shibaura Mechatronics Co., Ltd., CFS-4EP-LL). Subsequently, a-C was deposited on a Cu surface at a power of 300 W in an Ar atmosphere (~0.6 Pa) using RF magnetron sputtering. In the case of N doping, a-C:N was deposited in an Ar–N_2 atmosphere. The a-C and N concentrations were controlled by changing the flow rate of the Ar and N_2 gases. The experiment conditions are described in detail in Chapter 6.

2.2.2.2. Cu sputtering on an Al_2O_3 substrate in preparation of graphene growth

The sample for the sputtering of Cu on an Al_2O_3 substrate was prepared by the Ago group (Kyushu University). A 1000 nm thick Cu film was deposited on an Al_2O_3 substrate by using RF magnetron sputtering (Shibaura Mechatronics Co., Ltd., CFS-4ES) with a power of 300 W in an Ar atmosphere (~0.6 Pa) [3].

2.2.3. Deposition and transfer of SLG

After the fabrication of a Cu film on the Al_2O_3 substrate, large-grain SLG was deposited by the Ago group (Kyushu University). The CVD of SLG is similar to the method described in a previous report [2–4]. After the fabrication of an epitaxial Cu film by sputtering, the sputtered Cu film was inserted into a horizontal quartz tube. The substrate was then heated up and annealed for 40 min at ambient pressure, 1000°C, and a gas flow of H_2/Ar. Subsequently, the temperature was raised from 1000°C to 1075°C in 20 min and CH_4 gas (10 ppm) was introduced to the quartz tube for 90 min as a C precursor for the SLG synthesis. The sample was then rapidly cooled down to room temperature by removing the sample holder from furnace with a magnet handle under H_2/Ar flow.

The preparation of stacked graphene layers and transfer of SLG are similar to those described in a previous report [3,5,6] and performed by Ago group (Kyushu University). The transfer of SLG onto SLG/Cu as BLG/Cu is schematically shown in Fig. 2.2. The SLG/Cu surface was covered with polymethyl methacrylate (PMMA) by spin-coating. Thermal tape (Revalpha, Nitto Denko) was attached to the PMMA surface. The Cu film was then dissolved in aqueous $FeCl_3$/HCl solution. Subsequently, the thermal tape/PMMA/SLG composite was washed with deionized water and transferred onto the surface of another SLG/Cu sample. Finally, the thermal tape and PMMA were removed using acetone, leading to the formation of a BLG film on the Cu surface. Note that the transfer process of TLG or SLG onto the SiO_2/Si substrate was the same as that described above for the BLG case.

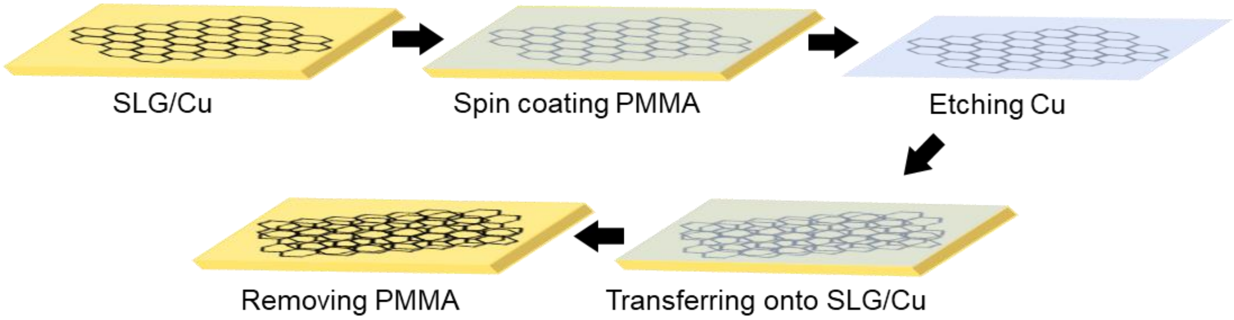

Figure 2.2. Schematic of the transfer of SLG onto SLG/Cu as BLG/Cu.

2.3. Temperature humidity storage test

The temperature and humidity chamber (Fig. 2.3) was used to test the resistance of Cu to oxidation due to humidity under accelerated temperature and humidity conditions. The chamber contains a refrigerator, heater, and humidifier, which were used to create accelerated test conditions.

The temperature and humidity chamber (ESPEC, SH-242) is an important apparatus, which was used to conduct the THS test in this work to evaluate the long-term reliability of Cu in terms of protection against oxidation due to humidity. Humidity in terms of % RH is the relative ratio between the actual moisture in the air and amount of saturated moisture at the given temperature. It is a common parameter used when the real effect of humidity is considered. For absolute humidity |RH|, mostly expressed in the unit of g/m^3, it refers to the actual moisture present in air, regardless the temperature. In this THS chamber, various temperature and % RH conditions were set. The temperature and humidity were increased to achieve the target conditions, as listed below. A typical temperature–humidity profile (85℃/85% RH) is shown in Fig. 2.4.

1) First, the samples are placed on the grate inside the chamber.
2) To set the THS conditions, the target temperature is divided into 7 steps (starting from ~30℃) and the humidity is divided into 3 steps (starting from step 5, ~65% RH).
3) From steps 1–6, the operating time is set to 15 min/step. During each step, the temperature and humidity are continuously increased.
4) The soak time starts at step 7 (required THS test time). The THS test time is set to count down after the target conditions are reached. The samples are soaked under these conditions until the time limit is reached.
5) The conditions to cool and dry the chamber (25℃/25% RH) before removing the samples are set.

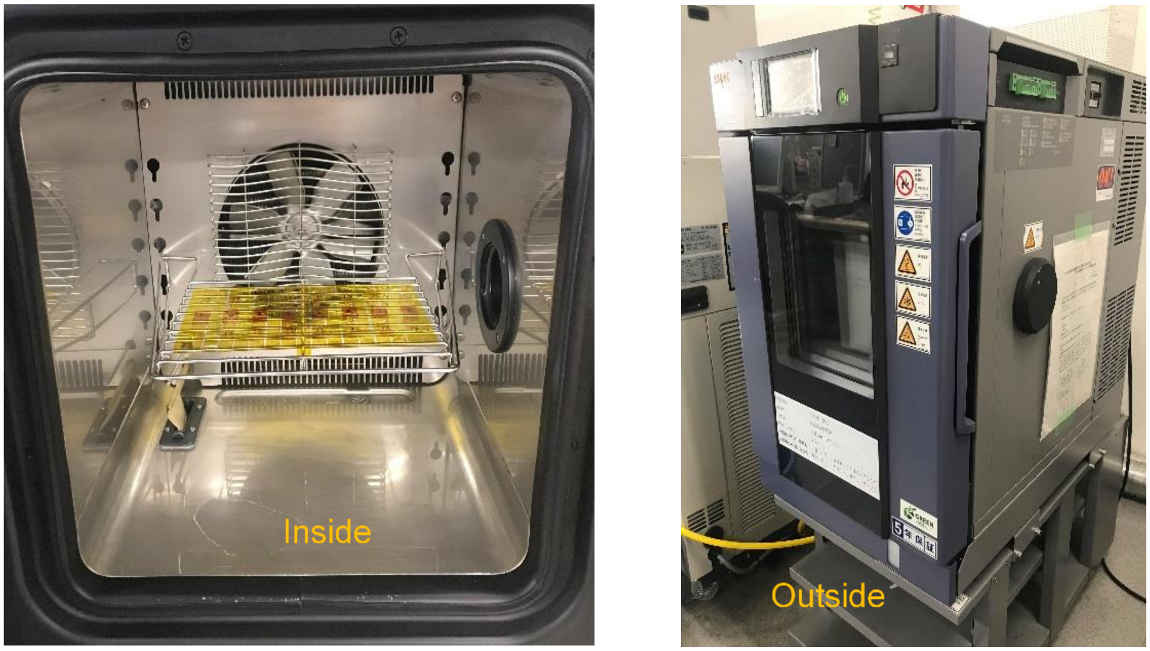

Figure 2.3. Temperature and humidity chamber.

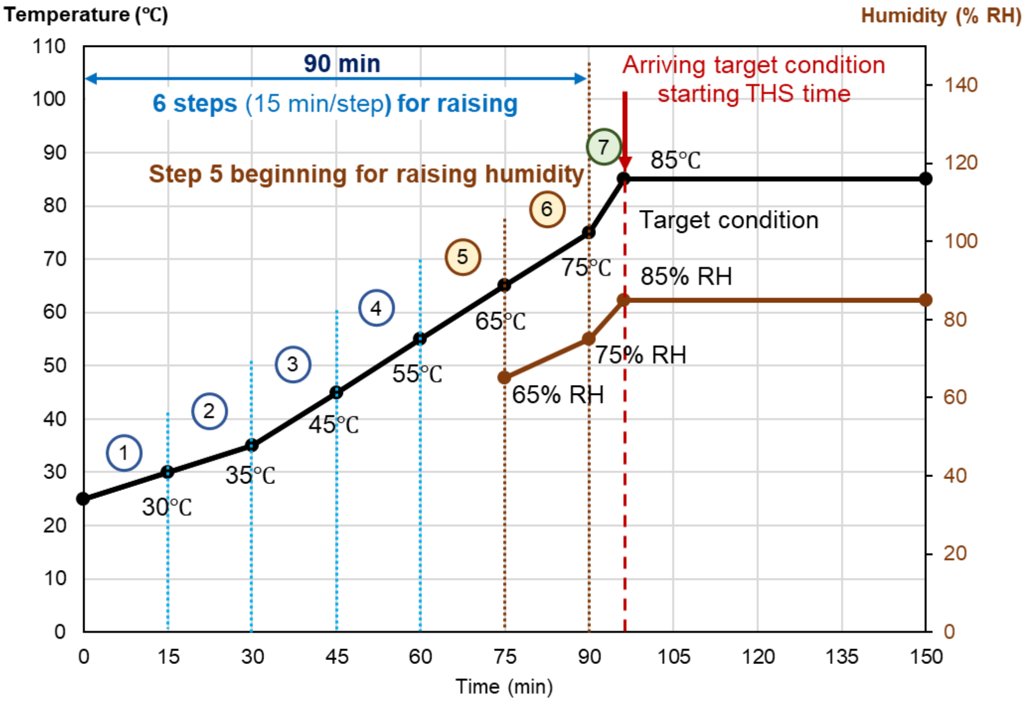

Figure 2.4. Steps used to increase the temperature and humidity to achieve the target conditions (85°C/85% RH).

2.4. Methodology

2.4.1. Raman spectroscopy

Raman spectroscopy is a practical tool that can be used to quickly measure the vibrational energy modes of molecules. It relies upon the inelastic scattering of photons. When the laser light interacts with molecular vibrations, photon scattering is induced and the energy levels of the scattered photons are shifted up or down. The changes in the energy levels of the scattered photons provide information about the vibrational modes, as shown in Fig. 2.5. In the vast majority of scattering events, laser photons are scattered at the same energy. The incident photons are called “elastic or Rayleigh scattering.” Raman scattering is an inelastic scattering process, which is based on the transfer of energy between the molecule and scattered photon. If the molecule gains energy from the scattered photon, the scattered photon will have a lower energy than the incident photon, resulting in a longer wavelength (“Stokes”). Contrarily, if the scattered photon gains energy from molecules, the final energy state will be lower than the initial state and the wavelength of the scattered photon will be lower (“Anti-Stokes”). The frequency range of the Stokes and anti-Stokes lines is the same. Raman measurements are mostly used to observe the Stokes shift.

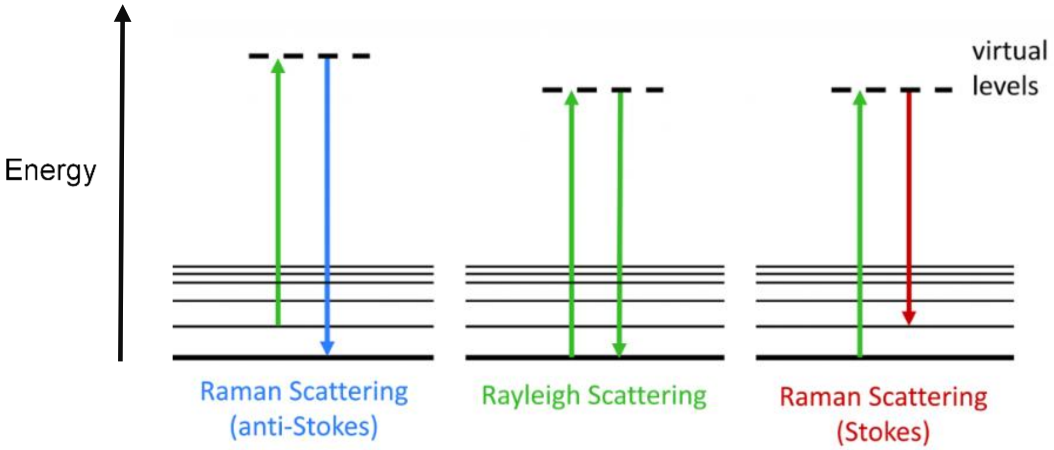

Figure 2.5. Energy level diagram showing Rayleigh and Raman scattering (Stokes and anti-Stokes lines) [7].

In this work, Raman spectroscopy was used to measure the characteristics of the graphene film. The Raman spectrum exhibits two main peaks, which are the G and 2D bands at 1587 and 2680 cm^{-1}, respectively. An additional peak, that is, the defect-related D band, appears at ~1350 cm^{-1} when the carbon lattice has defects.

- The G band is located at ~1587 cm^{-1}. The band corresponds to the in-plane vibrational mode of sp^2 hybridized carbon atoms. The increase in the G band intensity is due to the higher number of graphene layers. However, the number of graphene layers is determined by investigating the intensity ratio of the G and 2D bands.

- The D band, disorder mode, is located at ~1350 cm^{-1}. It corresponds to the breathing mode of sp2 hybridized carbon rings. The D band originates from a hybridized vibrational mode associated with defects in the graphene structure or at the graphene edges (disconnection in the carbon network). The intensity of the D band is typically high if the carbon lattice contains many defects, which explains why the D band is generally used to determine the quality of graphene sheets [8].

- The 2D band, the second-order D band, is located at ~2680 cm^{-1}. It is the result of a two-phonon lattice vibrational process. It is independent of defects or graphene edges. The intensity of the 2D band is always strong in graphene and can be used to determine the number of graphene layers in comparison with the G band. The relative intensity ratio of the 2D/G bands of SLG is >2 and decreases for multilayer graphene and graphite.

The Raman vibrational modes and their significance are provided in Table 2.1.

Table 2.1 Different Raman modes and their significance. [8]

Mode	Position (cm^{-1})	Significance
G	~1587	The G band originates from the stretching of the C–C bond in graphitic materials.
D	~1350	This band is associated with defects in the graphene structure or at the graphene edges.
2D	~2680	This is the second-order D band. It is always strong in graphene and can be used to determine the number of graphene layers.

2.4.2. X-ray photoelectron spectroscopy

The XPS is a surface characterization technique used to quantitatively determine the atomic composition at an analysis depth of ~1–10 nm. The XPS is conducted under ultra-high vacuum conditions (~10^{-9} mbar). A sample surface is irradiated with monochromatic x-rays, resulting in the emission of photoelectrons with energies that are characteristic of different elements, as shown in Fig. 2.6. During the measurement, the kinetic energy of the electrons that are emitted from the top of the material is recorded and used to create a XPS spectrum. The energies and intensities of the photoelectron peaks are used to identify and quantify the surface elements. The measured kinetic energies can be converted to binding energies by using the equation below:

$$E_b = E_p - E_k - \phi \tag{1}$$

where E_b is the binding energy of the electron, E_p is the energy of the X-ray photons, E_k is the kinetic energy of the emitted photoelectron, and ϕ is the work function depending on the material and spectrometer.

Different Cu-oxidation states and different C–C and C–N bond concentrations were identified with XPS (AXIS-Ultra DLD, Shimadzu) in this work. The binding energy of each chemical bond is described in Table 2.2. Based on XPS measurements after each cycle of Ar+ ion etching of the a-C:N/Cu surface, depth profiles of the element concentrations of the a-C:N/Cu layers were obtained.

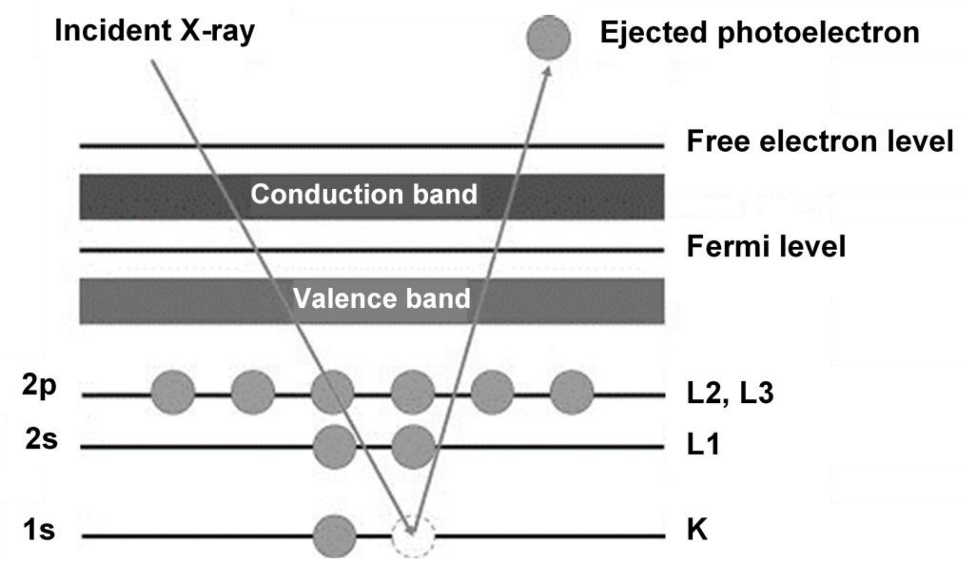

Figure 2.6. Photoemission process in XPS [12].

Table 2.2. Binding energies of the chemical bonds for Cu 2p and C 1s in XPS [13-20].

Binding energy (eV)	**Bond**
~932.4	Cu or Cu_2O
~933.6	CuO
~284.5	sp^2C
~285.5	sp^3C
286–286.8	sp^2C–N
287–287.8	sp^3C–N

2.4.3. Spectroscopic ellipsometer

The spectroscopic ellipsometer (SE) is used to measure the relative change in the polarization of light reflected by the sample surface. It is useful to determine the optical properties and film thickness of the sample based on measuring the top surface. Figure 2.7. shows the general SE principle. The oblique incidence of polarized light, which has a single wavelength, is directed onto the sample surface. The incidence plane is perpendicular to the sample surface. It contains a vector, k_{in}, which points to the propagation direction of the incident light. Vector k_{in} is perpendicular to the electric (E) and magnetic (B) fields of the light wave. The two components of E, that is, α and π, are perpendicular and parallel to the incidence plane, respectively. The polarization of the reflected light ("elliptically polarized light") differs from that of the incident light. This means that the amplitude and phase of the π and σ components of E also change.

The data obtained with the ellipsometer are two ellipsometric parameters: ψ and Δ. The relation between ψ and Δ is defined, as in equation below:

$$\tan(\psi)e^{i\Delta} = \frac{\rho_\pi}{\rho_\sigma} \tag{2}$$

where ρ_π and ρ_σ are the intensities of π and σ, respectively, after the reflection; tan(ψ) is related to the amplitude change upon reflection; and Δ is the phase shift.

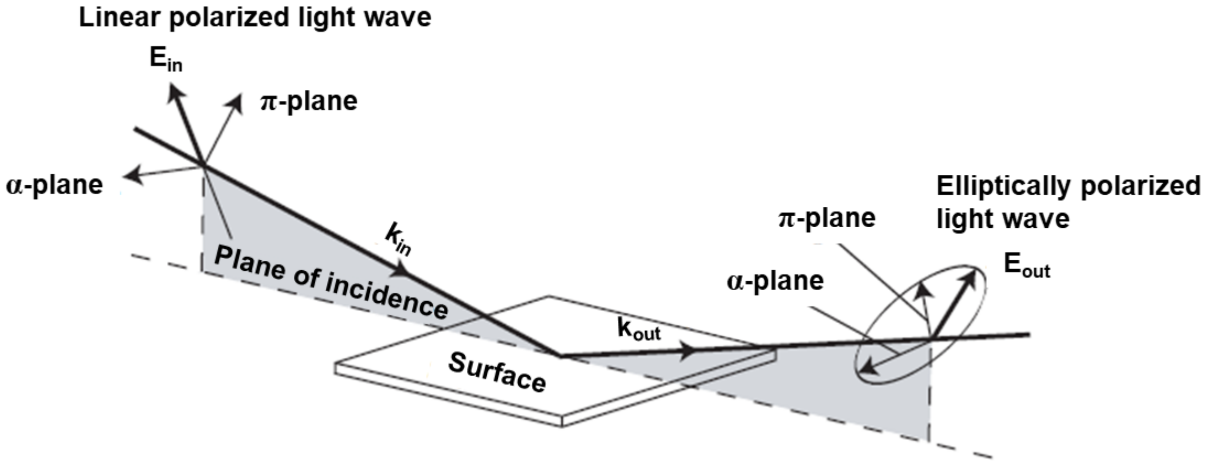

Figure 2.7. General principle of ellipsometry [21].

In this work, the SE (UVISEL™2) was used to determine the correlation between the SLG quality and Cu-oxide thickness in the collaboration with Horiba Techno Service. However, these data cannot be directly obtained from the ellipsometric parameters. The potential model structure of the measured sample and optical properties of each layer must be determined. The best fit between the model and measured parameters is estimated from the mean squared error (MSE). If the MSE is low, the obtained parameters can be used to determine the film thickness and optical parameters of the sample.

2.4.4. Optical microscopy

An OM is commonly used to magnify an object. It contains at least two lenses. Figure 2.8 shows the basic configuration of an OM. An excitation filter is used to allow only a small wavelength range of the light source to pass. A dichroic mirror then reflects the excitation light (blue) onto the sample and, at the same time, allows the emission of light (longer wavelength than blue) reflected by the sample surface to pass through the emission filter. The emission filter separates the excitation from the emitted light before the light reaches the detector.

An OM was used in this work to observe the change of the surface color between Cu with and without barrier after the THS test.

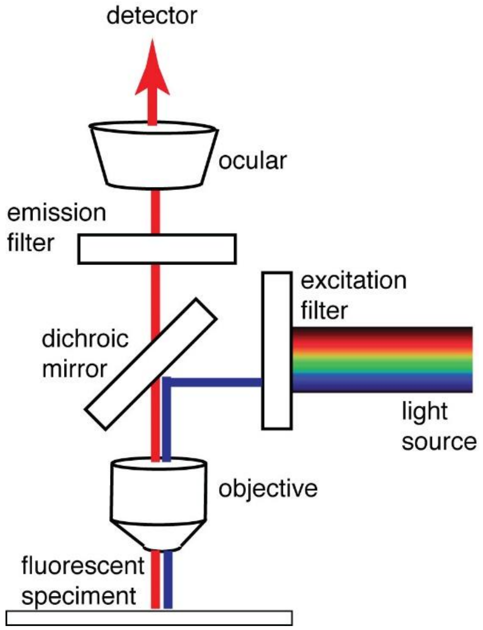

Figure 2.8. Basic construction of OM [22]

2.4.5. Scanning electron microscope

The SEM is used to observe the sample surface. When the surface of a sample is irradiated with an electron beam, secondary electrons will be emitted from the surface. The surface morphology can be determined by the two-dimensional scanning of an electron beam over the surface and detection of secondary electrons. The basic configuration of a SEM is shown in Fig. 2.9. The SEM requires an electron gun, condenser lens, and objective lens. The scanning coil is used to scan the electron beam over the sample surface along the x- or y-axis. Secondary electron detectors are used to detect secondary electrons emitted from the sample surface. An image is obtained by collecting the secondary electrons. The inside chamber must be kept under a high vacuum of 10^{-3}–10^{-4} Pa.

The SEM (JSM-7610F) was used in this work to observe the morphology of the a-C:N surface before and after the THS test.

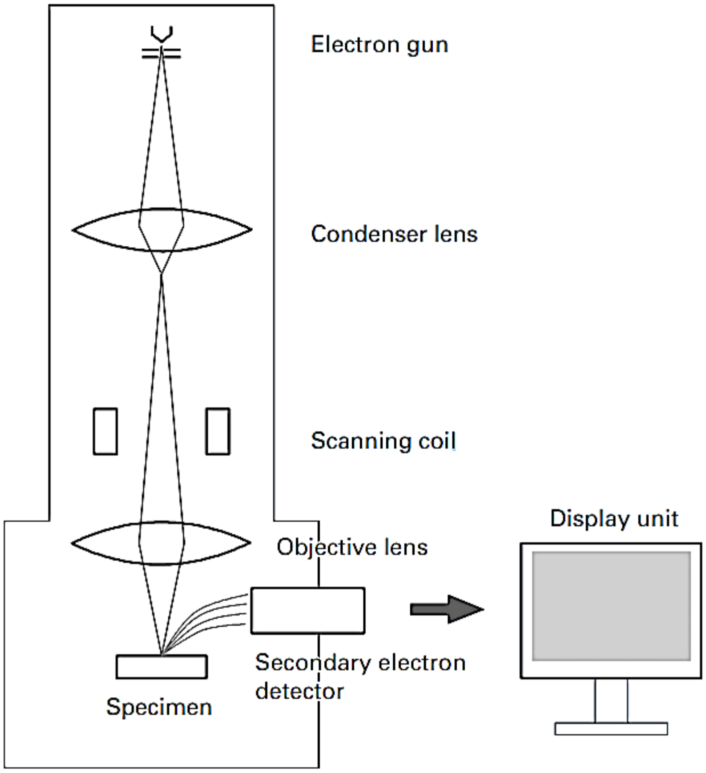

Figure 2.9. Basic configuration of a SEM [23].

2.4.6. Transmission electron microscopy

In TEM, transmitted electrons (electrons passing through the sample) are used to create an image. It can be used to determine the composition of small samples with near-atomic resolution. The basic configuration of a TEM is shown in Fig. 2.10. The electron gun, condenser lenses, and condenser aperture are used to produce a small electron beam. The electron beam is transmitted through the sample. The objective lens is then used to focus the transmitted electron beam and create the image. The image is enlarged by the column of intermediate and projector lenses. The magnification can be adjusted to obtain a good image on the screen.

The TEM was used in this work to observe the thickness the a-C:N layer under various sputtering conditions.

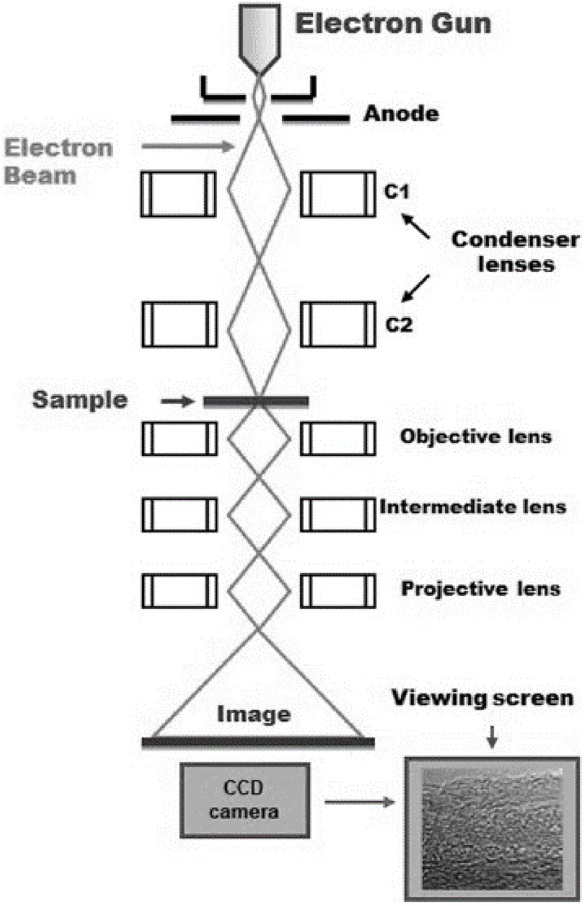

Figure 2.10. Basic configuration of a TEM [24].

2.4.7. Four-probe method

The four-probe method is a primary technique used to measure the sheet resistance. The basic configuration of this tool is shown in Fig. 2.11. It consists of four electrical probes set up with equal spacings between each probe. A current (I) is applied to the two outer probes and the voltage (V) between the two inner probes is measured. The sheet resistance (R_S) is calculated using the equation below [25]:

$$R_S = \frac{\pi}{\ln(2)} \frac{V}{I} \tag{3}$$

Note that this equation is valid for measuring a thin film with a thickness that is smaller than 40% of the probe spacing. In addition, the lateral dimensions of the sample should be sufficiently large to avoid unreliable measurement results.

The four-probe method was used in this work to detect the formation of Cu-oxide after the THS test by measuring the increase in the Cu sheet resistance.

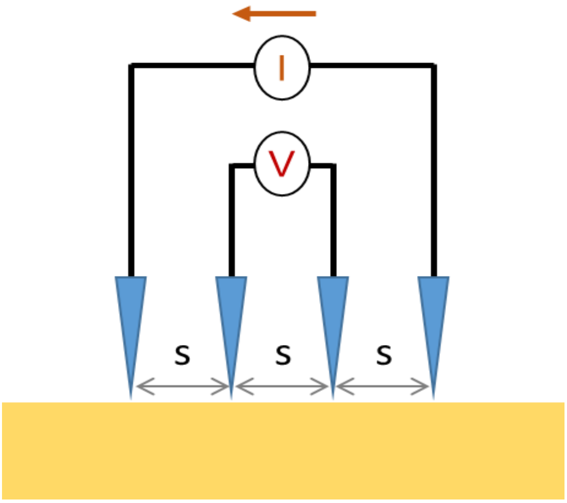

Figure 2.11. Schematic diagram of a four-point probe.

References

[1] C. Charpentier, “Investigation of deposition conditions and annealing treatments on sputtered ZnO:Al thin films: Material properties and application to microcristalline silicon solar cells.” Plasma Physics. Ecole Polytechnique X, (2012).

[2] H. Ago, K. Kawahara, Y. Ogawa, S. Tanoue, M. A. Bissett, M. Tsuji, H. Sakaguchi, R. J. Koch, F. Fromm, T. Seyller, K. Komatsu, and K. Tsukagoshi, Appl. Phys. Express **6**, 075101 (2013).

[3] B. Hu, H. Ago, Y. Ito, K. Kawahara, M. Tsuji, E. Magome, K. Sumitani, N. Mizuta, K. Ikeda, and S. Mizuno, Carbon **50**, 57 (2012).

[4] C. M. Orofeo, H. Hibino, K. Kawahara, Y. Ogawa, M. Tsuji, K. Ikeda, S. Mizono, and H. Ago, Carbon **50**, 2189 (2012).

[5] P. Li, C. Chen, J. Zhang, S. Li, B. Sun, and Q. Bao, Front. Mater. **1**, 26 (2014).

[6] Y. Takesaki, Kenji Kawahara, H. Hibino, S. Okada, M. Tsuji, and H. Ago, Chem. Mater. **28**, 4583−4592 (2016).

[7] Edinburgh Instruments “What Is Raman Spectroscopy? | Raman Spectroscopy Principle”, www.edinst.com/blog/what-is-raman-spectroscopy. Accessed 22 Mar. 2020.

[8] A. Y. Lu, S. Y. Wei, C. Y, Wu, Y. Hernandez, T. Y. Chen, T. H. Liu, C. W. Pao, F. R. Chen, L. J. Li, and Z. Y. Juang, RSC Adv. **2**, 3008 (2012).

[9] M. Wall, “Characterization of Graphene Using Raman Spectroscopy.” AZoM.Com, Thermo Fisher Scientific – Materials & Structural Analysis, 7 Aug. 2012, www.azom.com/article.aspx?ArticleID=6271.www.azom.com/article.aspx?ArticleID=6271.

[10] C. F. Comanescu, Int. Semiconductor Conf., 2016, p.49.

[11] H. Iguchi, C. Higashi, Y. Funasaki, K. Fujita, A. Mori, A. Nakasuga, and T. Maruyama, Sci. Rep. **7**, 39937 (2017).

[12] C. J. Corcoran, H. Tavassol, M. A. Rigsby, P. S. Bagus, and A. Wieckowski, J. Power Sources **195**, 785 (2010).

[13] J. P. Espinós, J. Morales, A. Barranco, A. Caballero, J. P. Holgado, and A. R. González-Elipe, J. Phys. Chem. B **106**, 6921 (2002).

[14] S. Poulston, P. M. Parlett, P. Stone, and M. Bowker, Surf. Interface Anal. **24**, 811 (1996).

[15] S. Suzuki, Y. Ishikawa, M. Isshiki, and Y. Waseda, Mater. Trans., JIM **38**, 1004 (1997).

[16] J. Iijima, J. W. Lim, S. H. Hong, S. Suzuki, K. Mimura, and M. Isshiki, Appl. Surf. Sci. **253**, 2825 (2006).

[17] A. P. Dementjev, A. de Graaf, M. C. M. van de Sanden, K. I. Maslakov, A. V. Naumkin, and A. A. Serov, Diam. Relat. Mater. **9**, 1904 (2000).

[18] J. W. Suk, S. Murali, J. An, and R. S. Ruoff, Carbon **50**, 2220 (2012).

[19] S. Xu, S. Kumar, Y. A. Li, N. Jiang, and S. Lee, J. Phys. Condens. Matter **12**, L121 (2000).

[20] K. Yamamoto, Y. Koga, S. Fujiwara, F. Kokai, J. I. Kleiman, and K. K. Kim, Thin Solid Films **339**, 38 (1999).

[21] J. A. Woollam "What Is Ellipsometry?", www.jawoollam.com/resources/ellipsometry-tutorial/what-is-ellipsometry. Accessed 22 Mar. 2020.

[22] P. Banks, "Development of the Optical Microscope" BioTex, 31 Oct. 2014, www.biotek.jp/ja/resources/white-papers/development-of-the-optical-microscope.

[23] "Scanning Electron Microscope A To Z | Applications | JEOL Ltd." Basic Knowledge For Using The SEM, www.jeol.co.jp/en/applications/detail/891.html. Accessed 25 Mar. 2020.

[24] K. Barbara, S. Pusz, and B. J. Valentine, Int. J. Coal Geol. **211**, 103203 (2019).

[25] Ossila "Sheet Resistance Equations and Theory | Complete Guide.", www.ossila.com/pages/sheet-resistance-theory. Accessed 24 Mar. 2020.

CHAPTER 3

COPPER SURFACE OXIDATION AND ITS EFFECTS ON SHEET RESISTANCE

3.1. Introduction

As describe in chapter 1, the long-term storage reliability of Cu against oxidation has become a serious concern [1–3]. Therefore, the process of reliability test under acceleration conditions is becoming an important method conducted to evaluate the Cu reliability against oxidation due to moisture.

To test the reliability of Cu metallization against oxidation, various acceleration conditions of THS test should be adopted to understand the failure mechanism of the Cu. Moreover, the effects of Cu oxidation as such the change of Cu sheet resistance depended on the remaining Cu thickness should be investigated to determine the Cu lifetime. Results of Cu sheet resistance change can be obtained in a short time after the THS test, then, it can be estimated to establish a model of lifetime prediction of Cu. Because the conventional models of a lifetime prediction are mostly based on the test results of conventional Al-based metallization [4,5], the prediction model for Cu metallization is required.

In this chapter, the characteristics of Cu oxidation and its effects under the accelerated conditions of the THS test were studied by sheet resistance measurement and XPS. The XPS measurement was performed to investigate the different amounts of Cu_2O and CuO on the Cu surface. The XPS depth profiling was carried out to confirm the results of sheet resistance change. At the end of this chapter, a sample model for prediction of Cu lifetime is proposed based on the measured sheet resistance.

3.2. Experimental methods

In this work, two main experiments were performed: the first one is to investigate the Cu oxidation behavior depending on the standard THS test and the other one is to investigate the characteristics of Cu oxidation at use conditions and also establish the lifetime prediction model, respectively. For preparation of Cu samples, 100-nm-thick Cu film was deposited on SiO_2/Si substrate using DC magnetron sputtering at 200°C to complete the Cu grain growth for stabilizing the initial sheet resistance. To measure the change of Cu sheet resistance, two Cu samples with 2×2 cm in size were prepared for each THS test.

In the first experiment, THS test was performed under the conditions of 85°C at the range of humidity of 75, 85, and 95% RH by covering the standard condition (85°C/85% RH). The sheet resistance of each sample was measured using four-point probe method before and after 25, 50, and 100 h of THS test. Each value of Cu sheet resistance was normalized by its initial value, which was measured before the THS test. Then, the Cu oxidation behavior among these tests were identified by XPS (AXIS-Ultra DLD, Shimadzu) with ~110-μm diameter of Al X-ray source (1486.6 eV) measured after 100 h of the THS test.

In the second experiment, steps of sample preparation are the same as those of the first experiment, but the conditions of THS test are changed appropriately to obtain the results corresponding to the spontaneous behavior in use conditions at lower temperature and humidity. Two groups of THS tests: the temperature dependence (85, 75, and 65°C, at fixed 75% RH) and the humidity dependence (75, 65, and 55% RH, at fixed 85°C) were studied. Temperature and humidity conditions can express in terms of dew-point temperature (T_d) and vapor pressure (e) using equation (1) and (2), respectively. Dew point is the temperature at which a sample of air must be cooled down to become complete saturation or reach 100% RH. The environmental vapor pressure is the saturation vapor pressure at the dew point. The summary of THS test condition expressed in terms of dew-point temperature and vapor pressure is shown in Tables 3.1 and 3.2.

$$T_d = \frac{237.3\left[\frac{\ln(RH/100)}{17.27} + \frac{T}{237.3+T}\right]}{1-\left[\frac{\ln(RH/100)}{17.27} + \frac{T}{237.3+T}\right]} \tag{1}$$

$$e = 0.6108\exp\left[\frac{17.27T_d}{T_d + 237.3}\right] \tag{2}$$

Table 3.1. Summary of THS test conditions for temperature dependence

Temperature, *T* (℃)	**Humidity, *RH* (% RH)**	**Dew point, T_d (℃)**	**Vapor pressure, *e* (kPa)**
85	75	77.85	43.58
75		68.29	29.03
65		58.71	18.82

Table 3.2 Summary of THS test conditions for humidity dependence

Temperature, *T* (℃)	**Humidity, *RH* (% RH)**	**Dew point, T_d (℃)**	**Vapor pressure, *e* (kPa)**
85	75	77.85	43.58
	65	74.41	37.77
	55	70.50	31.96

The change of Cu sheet resistance in various acceleration conditions was measured before and after 25, 50, 100, and 200 h of the THS test by a four-point probe method. Each value of Cu sheet resistance was normalized by its initial value, which was measured before the THS test.

The oxidation of the Cu surface was investigated by using XPS after 200 h of THS testing. The relative composition of Cu_2O and CuO was evaluated from the Cu 2p XPS spectrum after background subtraction. Depth profiling method was carried out [6−8] to investigate the different thickness of the oxidized Cu layer for supporting the different change of Cu sheet resistance. Every 10 s of etching, O 1s, Cu 2p, and Cu LMM spectra were investigated and recorded the relative atomic concentration ratios of O to Cu to obtain the depth profile of each sample. Cu LMM Auger spectrum was analyzed to distinguish between the metallic Cu and Cu_2O layers.

For the Cu lifetime prediction model, it has been proposed based on the Peck's model with using the correlated statistical analysis for lifetime acceleration. Then, the accuracy of the proposed model is estimated statistically and the significant parameters for predicting a lifetime are also suggested.

3.3. Results and discussion

3.3.1. Results of experiment 1:

3.3.1.1. Normalized sheet resistance change depending on accelerated humidity

Figure 3.1 shows the evolution of normalized sheet resistance (*R*) of each sample measured after 25, 50, and 100 h of THS test under the conditions of 85℃ at various relative humidity of 75, 85, and 95% RH. It displays that *R* rapidly increased after the first 25 h due to the reduction of Cu thickness resulting from the Cu oxidation. The increasing rate of *R* successively decreased after 50 and 100 h and it indicates that the further reduction of Cu thickness became slower than that of the initial 25 h. The highest *R* change was obtained as expected with the condition of the highest humidity as 95% RH at fix 85℃. However, there was no clear difference in the sheet resistance change between 75 and 85% RH at fix 85℃, as indicated in Fig. 3.2.

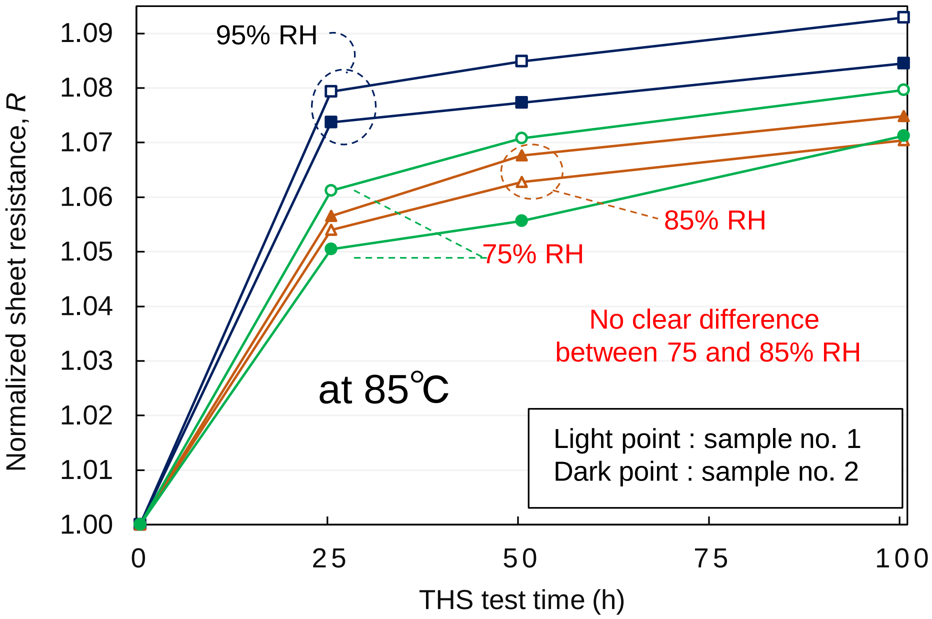

Figure 3.1. Normalized sheet resistance of the first experiment measured before and after 25, 50, and 100 h of THS test.

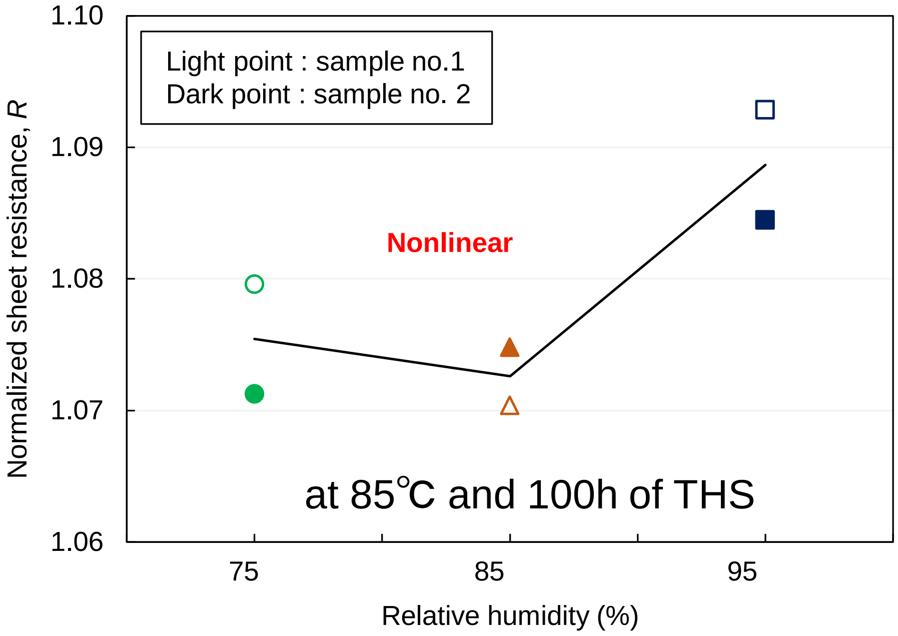

Figure 3.2. Comparison of normalized sheet resistance after 100 h of THS test, indicating nonlinear dependence on the humidity.

3.3.1.2. XPS analysis for the nonlinear dependence on the humidity

To investigate the reason for the nonlinear dependence on the humidity between 75 and 85% RH at 85℃, Cu 2p and O 1s XPS results were adopted to analyze the relative atomic concentration ratios of O to Cu measured on each sample surface after 100 h of the THS test, as shown in Fig. 3.3. It indicates that the relative O to Cu ratios linearly increase with the highly accelerated humidity. Since the relative increase of O content is according to the increase of moisture, the nonlinear behavior of the sheet resistance change could not be explained by analysing only the O to Cu atomic concentration ratios. It implied some structural changes in the oxidized Cu layer. Then, further analysis on Cu 2p XPS spectra was analyzed to identify what kind of oxidation state was formed on the Cu surface.

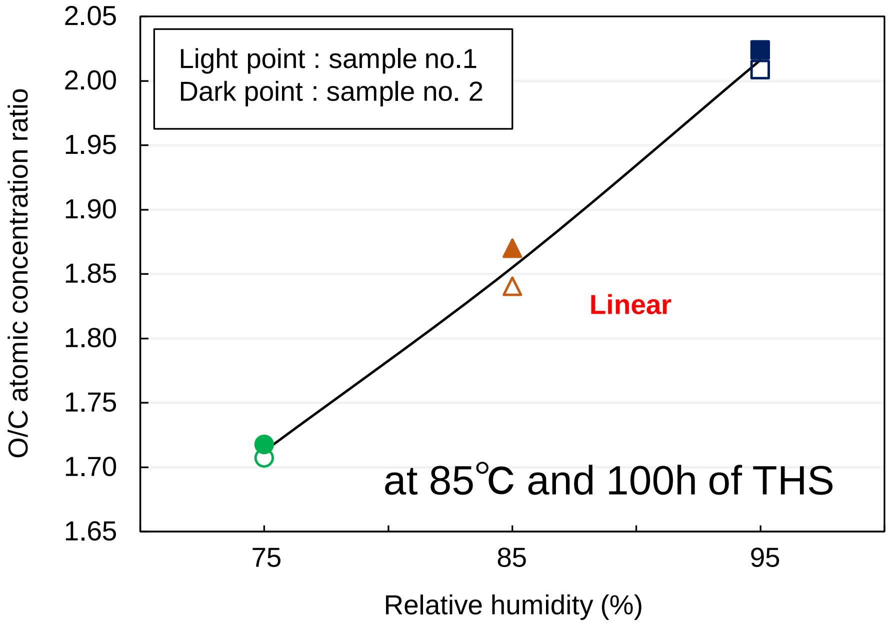

Figure 3.3. O/Cu atomic concentration ratios measured after 100 h of THS test, indicating the O/Cu ratios linearly increase with humidity.

Figure 3.4 shows the Cu 2p XPS spectra and the Cu (2p3/2) curve fitting to distinguish between Cu(I) in Cu_2O and Cu(II) in CuO peak located at the binding energy of ~932.5 and ~933.6 eV [9–12], respectively. The propotions of Cu(I) and Cu(II) are different for these three different conditions of humidity at the same temperature. Cu 2p spectra shows the highest content of Cu(I) at 95% RH and it successively reduces in lower humidity which is contrasted with the increase of Cu(II). Comparing between the 85 and 75% RH, Cu(II) content becomes the dominant structure in oxidized Cu layer at 85% RH while Cu(I) becomes the dominant structure at 75% RH. Based on the results of XPS and the nonlinear change of *R*, they indicate the regular change of Cu-oxide state in spite of almost the same range of *R* change between the 85 and 75% RH.

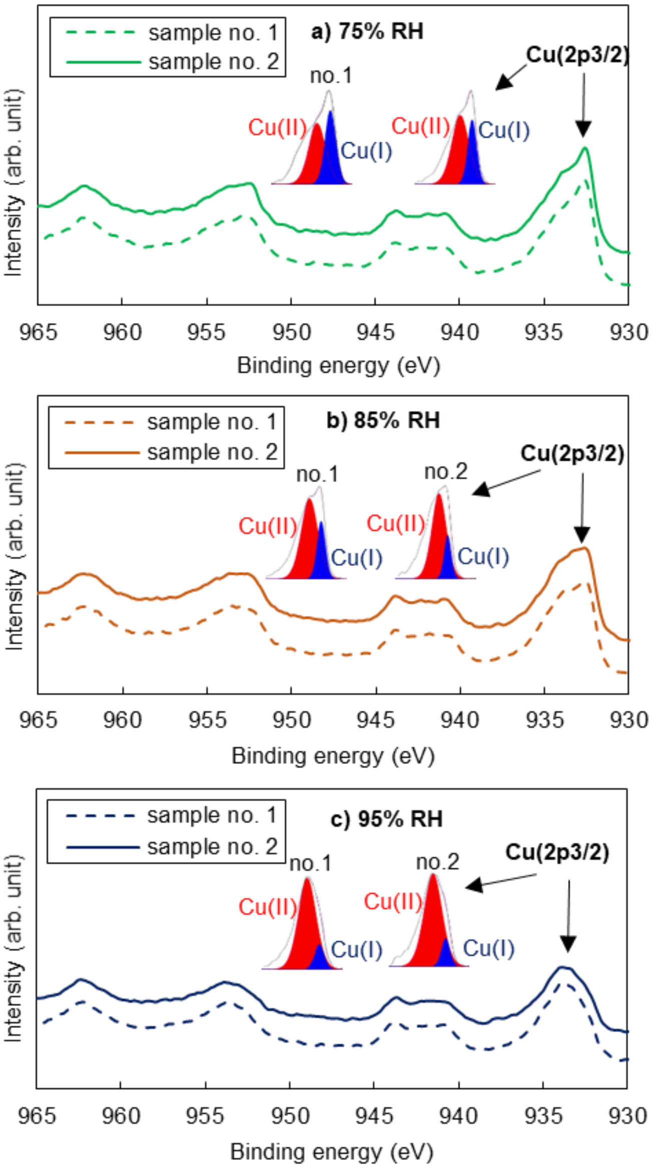

Figure 3.4. Cu 2p XPS spectra measured after 100 h of THS test under the conditions (a) 75% RH, (b) 85% RH, and (c) 95% RH at 85°C.

The results imply a potential cause of this issue that may relate to the relative volume of Cu_2O and CuO formation. It is possible that the different dominant structures of Cu oxidation among these two cases (85 and 75% RH) may consume almost the same amount of Cu, according to almost the same range of *R* for both cases (Fig. 3.2).

To prove this hypothesis, further analysis was carried out for considering the change in the relative volume during Cu-oxide formation and describe the nonlinear behavior between these two cases (85 and 75% RH) based on the hypothesis above.

3.3.1.3. Mechanism for the nonlinear dependence of normalized sheet resistance change.

To explain the phenomena based on the hypothesis above, the structural change from Cu into Cu_2O and CuO and their relative volume are considered in detail, as described below. There are two potential reactions of Cu oxidation. In the air atmosphere, Cu surface is oxidized by O atom from O_2 to form the Cu oxidation as the dry corrosion. This reaction immediately occurs when Cu surface was exposed to air, as shown in the following reactions (3) and (4).

$$4Cu + O_2 \rightarrow 2Cu_2O \tag{3}$$

$$2Cu_2O + O_2 \rightarrow 4CuO \tag{4}$$

Moreover, the wet corrosion can occur during the high humidity test where the relative humidity is higher than 60% RH [13]. In this reaction process, Cu is oxidized by O atom from H_2O to form the Cu oxidation, as shown in the following reactions (5) and (6).

$$2Cu + H_2O \rightarrow Cu_2O + H_2 \tag{5}$$

$$Cu_2O + H_2O \rightarrow 2CuO + H_2 \tag{6}$$

Cu surface was rapidly oxidized by O atom to form the first oxidation state as Cu_2O, and further oxidation by O atom provided the second oxidation state as CuO. The relative volume of Cu, Cu_2O, and CuO in a chemical reaction can be explained by the relationship, as in (7).

$$N_iV_i = N_pV_p \tag{7}$$

where *i* and *p* are the initial substance and product of reaction. *N* is the number of moles in a chemical reaction. *V* is the substance volume per a mole.

Based on the potential reactions above, the mole ratios, which mean the coefficients in a balanced equation between reactants and products involved in a chemical reaction, for the relationship of Cu:Cu_2O:CuO are 2:1:2. Relative volume of Cu, Cu_2O, and CuO are 7.09, 23.85, and 12.60 cm^3/mol [14,15], respectively. The change of relative volume related to the structural change from the Cu to Cu_2O and CuO, respectively, as summarized in Table 3.3.

It indicated that Cu film thickness was reduced to form the thicker Cu_2O layer as resulting the increase of *R*. During the Cu oxidation stage change, the relative volumes among the structural change from Cu_2O to CuO were not significant different based on almost the same volume ratios (Table 3.3) between Cu_2O and 2CuO products. These results correspond to the nonlinear change of *R* for the different cases of 75 and 85% RH in spite of the linear increase of O/Cu atomic concentration ratios.

According to the above discussion and Table 3.3, the nonlinear dependence of *R* change on the humidity between 75 and 85% RH at 85°C can be explained, as schematically shown in Fig. 3.5. While Cu was oxidized by O atoms to form the Cu_2O layer, the Cu film thickness continually decreased and affected the increase of *R*, corresponding to the results of low humidity at 75% RH. The CuO formation was considered to become more dominant in the Cu-oxide layer for higher humidity as 85% RH, leading to a higher O/Cu ratio. Because of the similar atomic volumes between Cu_2O and 2CuO (Table 3.3), they affected a similar change of *R*.

Table 3.3. Relative volume relates to the structural change of Cu and Cu-oxide.

Topic	**Relationship**		
Chemical relation	Cu	Cu_2O	CuO
Mole ratios	2	1	2
Relative volume (cm^{-3})	~14.18	~23.85	~25.2
Relative volume ratios	1	1.68	1.78

Regarding the nonlinear change of *R* as described above, the appropriate acceleration condition of the THS test to establish the Cu lifetime prediction model should be performed at the condition of 85°C/75% RH and lower to avoid the rapid change of Cu oxidation stage which was taken at the humidity higher than 85% RH and to obtain the results which correspond to the spontaneous behavior in the air at use condition, as expressed in the second experimental.

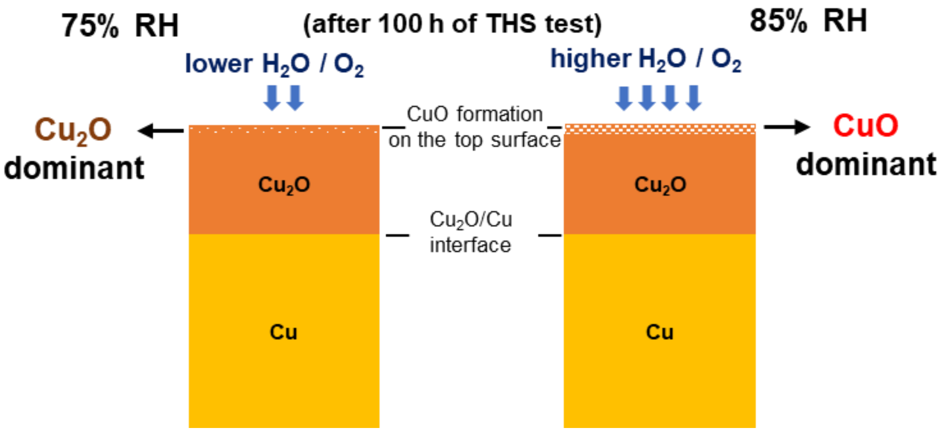

Figure 3.5. Proposed model to explain the difference of Cu-oxide structure between 75 and 85% RH.

3.3.2. Results of experiment 2:

3.3.2.1. Normalized sheet resistance depending on temperature and humidity

Figure 3.6 shows the time evolution of *R* under the various accelerations of THS test. The *R* rapidly increased after 25 h of the THS test. The increasing rate of *R* successively reduced after 100 h, and it indicates that the formation rate of oxidized Cu became slower than that of the initial 25 h. Comparing the dependencies between temperature and humidity, the results indicate that *R* increased with increasing both temperature and humidity, but it was more sensitive to the temperature than humidity.

Consideration in terms of vapor pressure dependence, *R* increases with increasing vapor pressure. These results are consistent with the previous report of J.-P. Wang group (Fig. 3.7) as showing the increasing rate of Cu oxidation with increasing water vapor pressure [16]. It is probably due to the increased Cu vacancies in Cu_2O leading to the increasing rate of Cu oxidation through these vacancies.

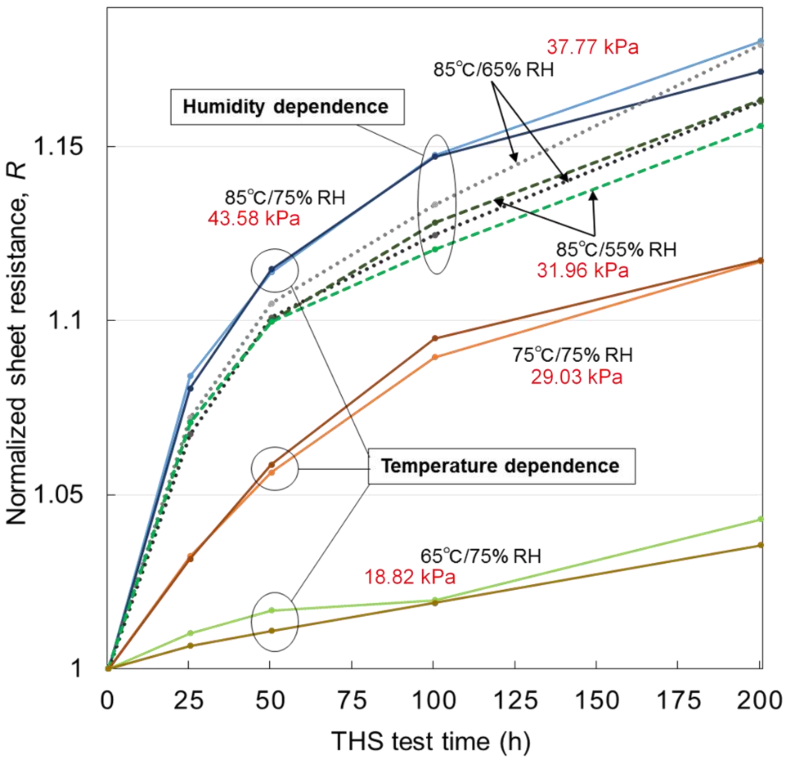

Figure 3.6. Time evolution of the normalized sheet resistance (*R*) during THS test under the acceleration conditions of temperature and humidity dependence tests or vapor pressure (in kPa).

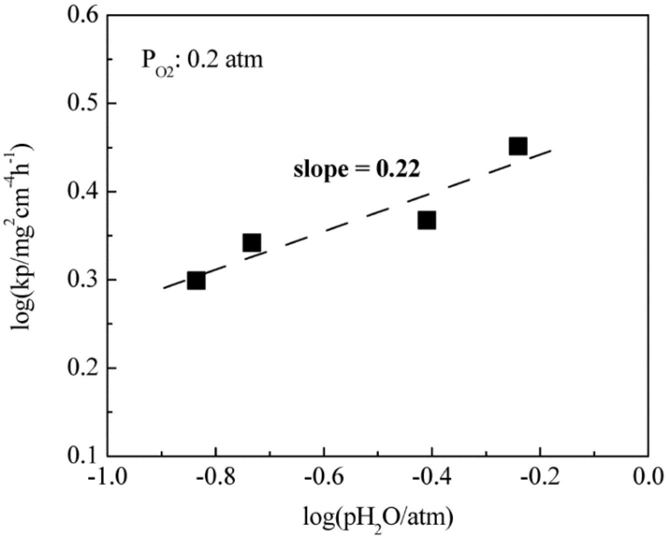

Figure 3.7. A previous report of parabolic rate constants (k_p) showing in terms of weight change per area per time ($mg^2cm^{-4}h^{-1}$) during Cu-oxide formation with water vapor pressure (pH_2O, atm) [16].

3.3.2.2. Difference of Cu-oxide thickness determined by XPS depth profiles

XPS depth profiling was carried out to measure the thickness difference of Cu-oxide layer under the various acceleration conditions of THS test for supporting the evolution of *R*. The variation of O/Cu atomic concentration ratios was estimated from the recorded Cu 2p and O 1s spectra measured on the top surface and after each cycle of Ar+ etching. Figure 3.8(a–b) shows the XPS depth profiles by plotting the O and Cu atomic concentrations as the function of etching time for all conditions of the temperature and humidity dependence tests. Typical spectra “A” to “D” [Fig. 3.8(a–b)] were determined from the measurement position during etching, i.e. “A” measured on the top surface before etching, “B” after the first etching, “C” among Cu_2O/Cu interface, and “D” after the final etching. The presence of Cu_2O + Cu and CuO was shown in Fig 3.9(a). In order to determine the relative position of Cu_2O/Cu interface, Cu LMM Auger spectrum was continually investigated after each Ar+ etching cycle until the metallic Cu peak appeared in the similar intensity with Cu_2O peak, as shown in Fig. 3.9(b) spectrum “C” [7]. In the case of temperature dependence test, results of depth profiles [Fig. 3.8(a)] confirm that the growth of the Cu_2O layer, which was indicated by the different positions of Cu_2O/Cu interface, corresponding to the increase of *R* (Fig. 3.6) under THS test. Moreover, depth profiles for the humidity dependence test [Fig. 3.8(b)] reveal that Cu_2O thickness just slightly increased as increasing humidity corresponding to the small difference of *R* (Fig. 3.6).

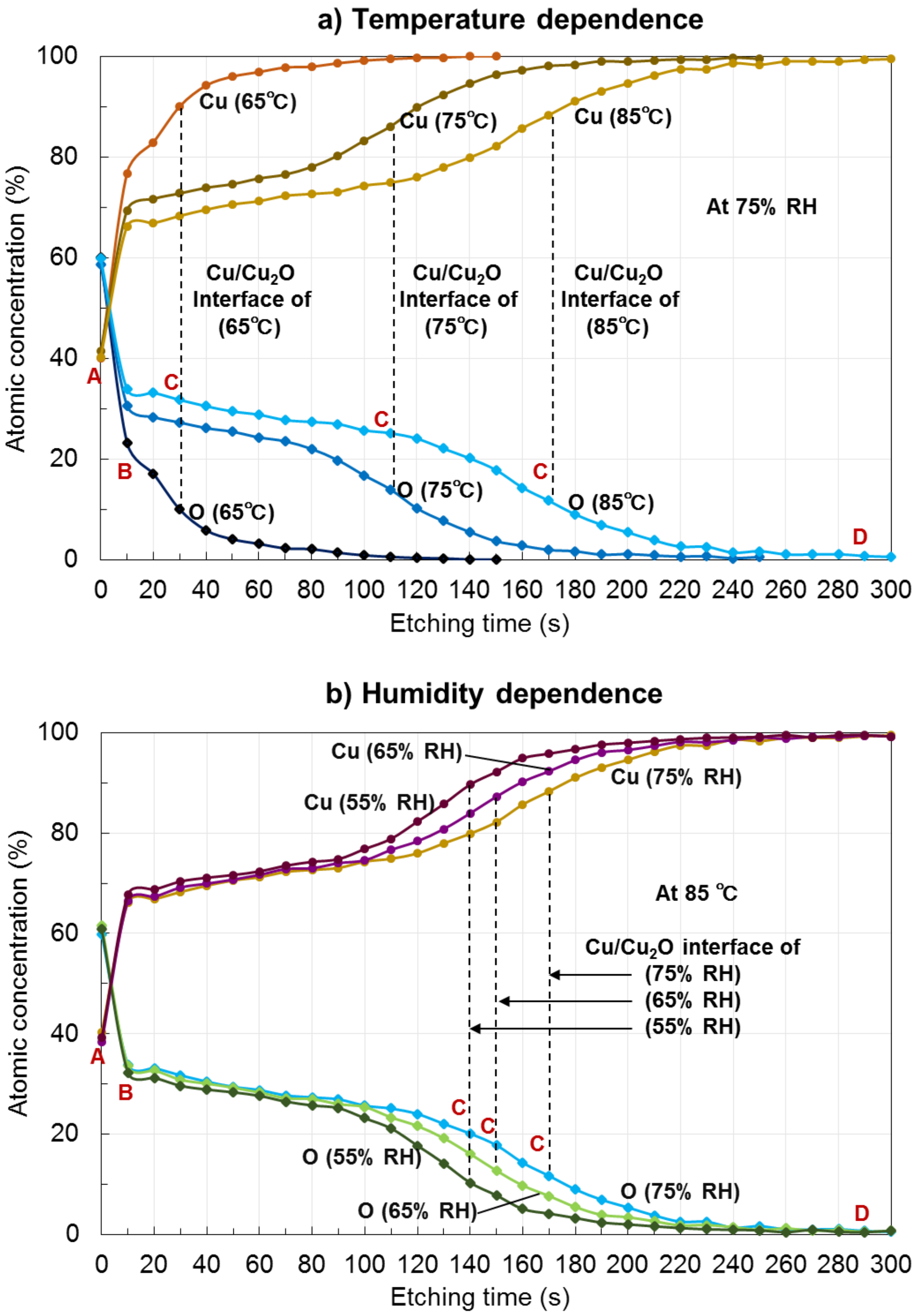

Figure 3.8. XPS depth profiles of (a) temperature and (b) humidity dependence tests.

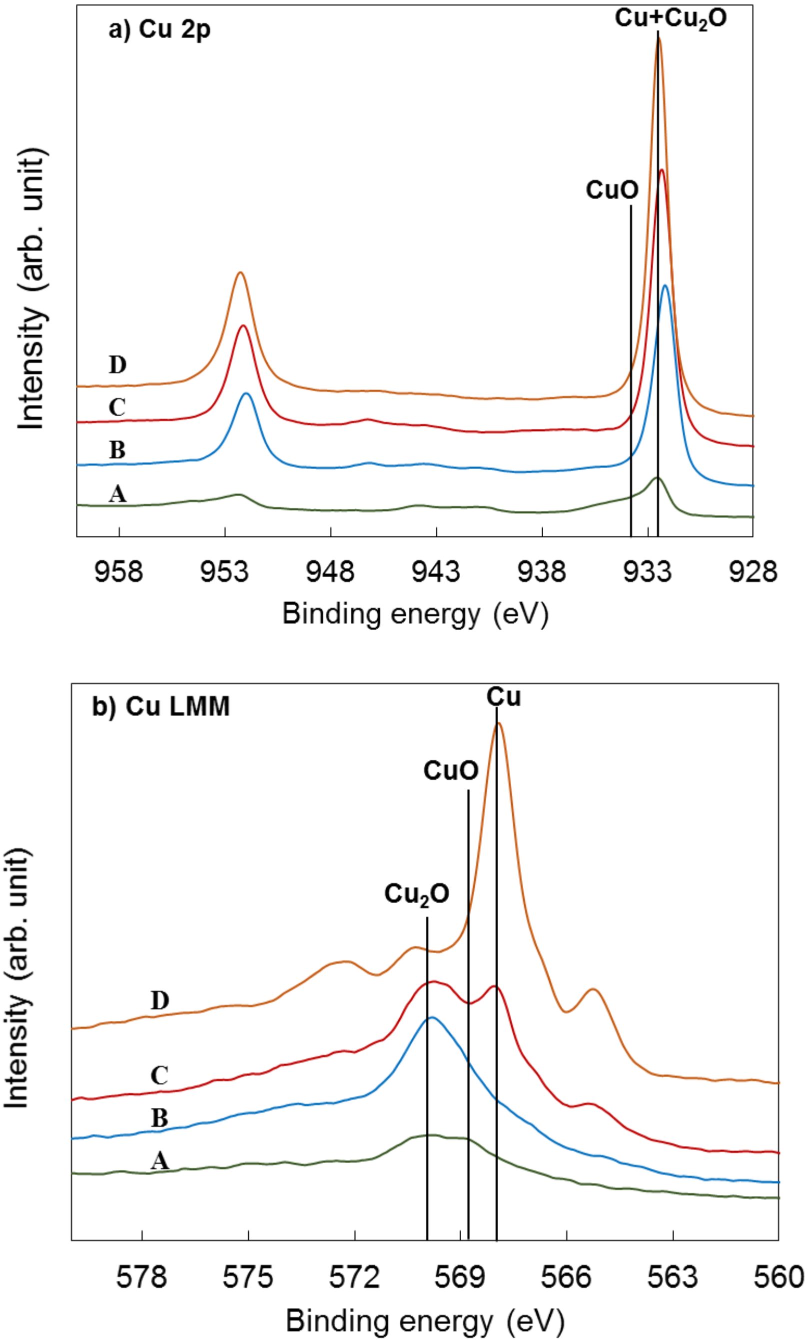

Figure 3.9. Comparison of (a) Cu 2p and (b) Cu LMM spectra indicating Cu_2O+CuO of the top surface ("A"), dominant Cu_2O after the first etching ("B"), Cu_2O+Cu at the interface ("C"), and Cu at the final etching ("D"), respectively. All measured locations are also indicated in Fig. 3.8.

3.3.2.3. Mechanism for normalized sheet resistance saturation with longer THS time

Beyond the investigation of Cu-oxide thickness, which directly affects the evolution of *R* under THS test as described above, further XPS analysis was carried out to investigate the reason for *R* saturation under these THS conditions. Figure 3.10 shows the relative composition of Cu(II) in CuO and Cu(I) in Cu_2O estimated from Cu 2p curve fitting of each sample surface after 100 and 200 h of THS testing. Comparing the CuO and Cu_2O compositions from 100 to 200 h, CuO was increased continually after long-term test in contrast with the decrease of Cu_2O. In addition, the results of CuO have an increasing trend in contrast with the decreasing trend of Cu_2O from the low to high acceleration conditions of the THS test. They implied the change of oxidation state from Cu_2O to CuO with increasing temperature, humidity, and period of THS test. After 200 h of THS testing, CuO became the dominant structure on the top surface for temperature dependence test of 75℃ and 85℃ [Fig. 3.10(a)], corresponding to the increasing rate of *R* was reduced after longer THS test time (Fig. 3.6). On the other hand, linear increase of *R* for 65℃ case (Fig. 3.6) corresponded to the dominant structure of Cu_2O, as shown in Fig. 3.10(a). In addition, CuO became the dominant structure in humidity dependence test [Fig. 3.10(b)], which was induced by temperature at 85℃, and the increasing rate of *R* was also reduced after long-term test (Fig. 3.6).

Figure 3.11 shows the schematic model to explain the variation of Cu-oxidation state in agreement with the evolution of *R* during the THS test under the low to high acceleration conditions of temperature and humidity based on the XPS analysis results, as described above.

a) Temperature dependence (at fixed 75% RH) measured after 100&200 h of THS test

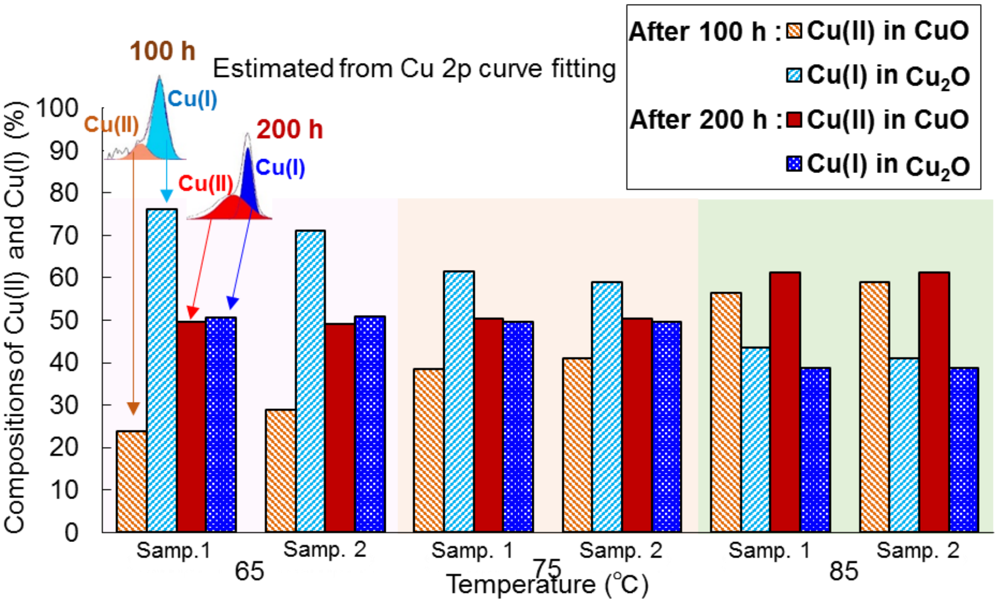

b) Humidity dependence (at fixed 85℃) measured after 100&200 h of THS test

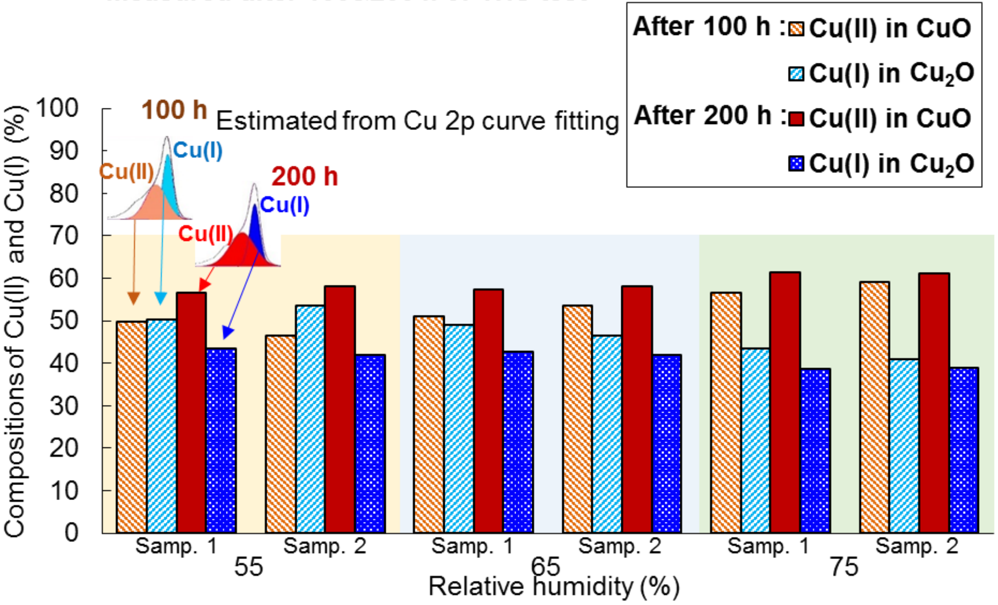

Figure 3.10. Relative compositions of Cu(II) in CuO and Cu(I) in Cu_2O estimated from the curve fitting in Cu 2p spectra, showing time dependence from 100 to 200 h of THS test for (a) temperature and (b) humidity dependence tests, respectively.

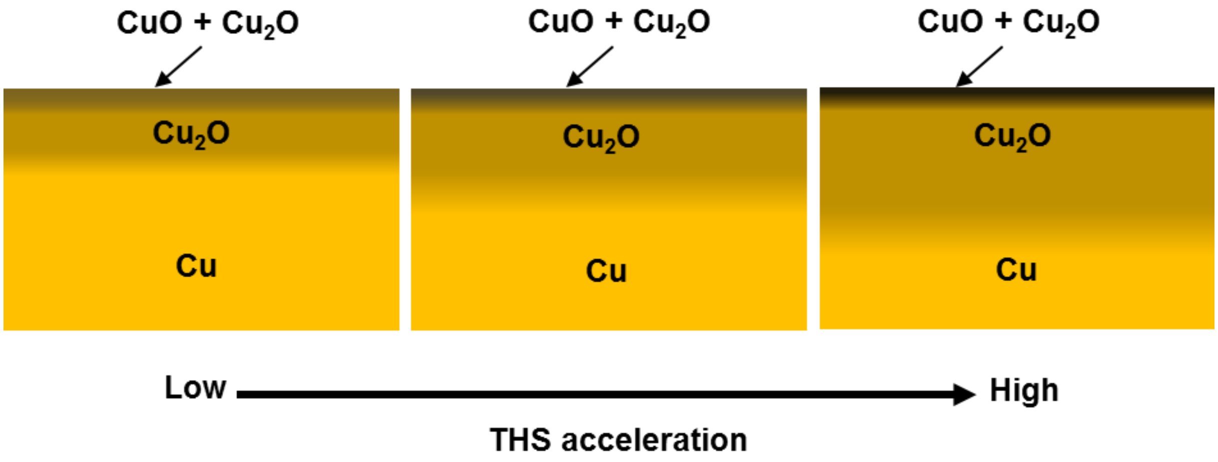

Figure 3.11. Schematic model based on XPS analysis results to explain the variation of Cu-oxide thickness under various acceleration conditions of THS test.

3.3.2.4. Cu lifetime prediction model

With using the results of experiment 2, Cu lifetime prediction model including the *R* saturation has been formulated by fitting the observed data of *R* based on the following models: the power-law time-dependent, the Arrhenius temperature-dependent, and the power-law humidity-dependent models [17,18], respectively, as in equations (8) to (10). Here, t and n in equation (8) are THS test time (h) and the power-law's exponent, respectively. E_a, k, and T in equation (9) are the activation energy (eV), the Boltzmann's constant, and temperature (K), respectively. RH and m in equation (10) are relative humidity and the power-law's exponent, respectively. The total model is shown in equation (11).

$$R \propto t^n \tag{8}$$

$$R \propto \exp\left(-\frac{E_a}{kT}\right) \tag{9}$$

$$R \propto RH^{m} \tag{10}$$

$$R \propto \exp\left[n\ln(t) - \frac{E_a}{kT} + m\ln(RH) \right] \tag{11}$$

From fitting the observed data of *R* with the total model by the regression analysis method, the prediction model of Cu lifetime has been obtained, as shown in equation (12). According to Fig. 3.12, lifetime prediction by the proposed model provides well agreement with observations. The coefficient of determination (R2), which is the square of the Pearson's product-moment correlation coefficient [19], is 0.984. The root-mean-square error (RMSE) value (~0.006) is very satisfactory. It means that the proposed model has been reasonably estimated. Although the increasing rate of *R* was reduced after 100 h of THS test (Fig. 3.6) due to the dominant structure of CuO formed in place of Cu_2O, the proposed model in equation (12) is also applicable for these behaviors.

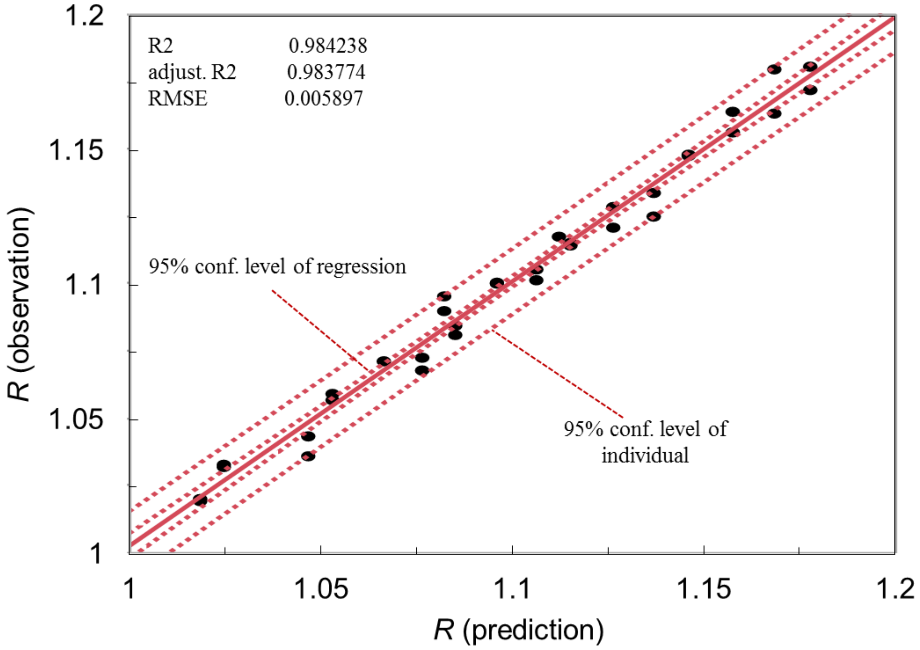

Figure 3.12. Correlation between observation and prediction of normalized sheet resistance (*R*), indicating very good accuracy of the proposed prediction model.

$$R = \exp\left[1.708 + 0.039\ln(t) + 0.056\ln(RH) - \frac{0.062}{kT}\right] \tag{12}$$

In order to compare the significant parameters (m and E_a) with those of other failure factors, it should be deformed to the form of normally used time-to-failure (*TTF*) based equation as the Peck's model, as shown in equation (13). Here, A_0 is arbitrary scale factor. The values of m and E_a from these failure factors induced by various acceleration conditions are 1.436 and 1.59, respectively.

$$TTF = A_0(RH)^{-1.436}\exp\left(\frac{1.59}{kT}\right) \tag{13}$$

The physical meaning of E_a based on the Arrhenius equation, this energy defines the minimum or threshold energy required to cause a chemical reaction. In the case that various chemical reactions continually occur, E_a is determined from which reaction required the maximum energy. H. Nagai group reported the E_a of Cu oxidation at the process temperature ~450℃, the E_a of the first Cu-oxide state as Cu_2O (~1.45 eV) is higher than that of the second state as CuO (~1.04 eV) [20]. It means that the E_a of Cu oxidation is determined from the Cu_2O formation. Our reporting E_a (1.59 eV) is relatively close to the previous report of E_a for Cu_2O formation, although it is a bit higher probably due to the lower process temperature. Therefore, the oxidation in our study is considered to be limited by the reaction of Cu_2O formation. Moreover, the relatively high value of the obtained E_a implies that the Cu oxidation can be delayed by reducing the temperature, leading to the longer lifetime of Cu.

3.4. Summary and conclusions

For long-term storage reliability of Cu metallization in the environment, temperature and humidity dependence of the sheet resistance increase has been studied. It was found that the *R* changed nonlinearly with the change of humidity. The increase of *R* at 85% RH/85℃ was almost the same as that of 75% RH/85℃ in spite of the higher oxidation. The nonlinear phenomena can be explained by the similar relative volume of the different Cu-oxidation states. The results suggest that lower humidity acceleration than 85% RH/85℃ would be more appropriate in the THS test to predict the Cu lifetime at the use condition. The appropriate range of THS tests in this work avoids the rapid change of the Cu oxidation state leading to the linear acceleration from the use condition. Normalized sheet resistance linearly depends on temperature and humidity or vapor pressure. XPS results confirm that the increase of Cu-oxide thickness corresponding to the increase of normalized sheet resistance and it is more sensitive to the temperature than humidity. Based on the temperature and humidity dependence of Cu sheet resistance under the appropriate THS conditions, a lifetime prediction model for Cu film against oxidation due to moisture was proposed. The proposed model of lifetime prediction for Cu is also applicable for the lifetime prediction in a longer time period although the increasing rate of normalized sheet resistance is reduced due to the formation of CuO. This model is expected to be used for the Cu lifetime prediction and further process development to improvement the reliability of Cu in terms of moisture protection.

References

[1] M. Schriver, W. J. Gannett, A. M. Zaniewski, M. F. Crommie, and A. Zettl, ACS Nano **7**, 5763 (2013).

[2] F. Zhou, Z. Li, G. J. Shenoy, L. Li, and H. Liu, ACS Nano **7**, 6939 (2013).

[3] M. Galbiati, A. C. Stoot, D. M. A. Mackenzie, P. Bøggild, and L. Camilli, Sci. Rep. **7**, 1 (2017).

[4] D. S. Peck, Proc. Int. Reliab. Phys. Symp., 1986, p. 44.

[5] O. Hallberg and D. S. Peck, Qual. Reliab. Eng. Int. **7**, 169 (1991).

[6] H. Bubert, E. Grallath, A. Quentmeier, M. Wielunski, and L. Borucki, Fresenius J. Anal. Chem. **353**, 456 (1995).

[7] S. K. Lee, H. C. Hsu, and W. H. Tuan, Mat. Res. **19**, 51 (2016).

[8] B.V. Appa Rao, K. C. Kumar, and N. Y. Hebalkar, Thin Solid Films. **556**, 337 (2014).

[9] S. Poulston, P. M. Parlett, P. Stone, and M. Bowker, Surf. Interface Anal. **24**, 811 (1996).

[10] J. Iijima, J. W. Lim, S. H. Hong, S. Suzuki, K. Mimura, M. Isshiki, Appl. Surf. Sci. **253**, 2825 (2006).

[11] B. Luo, P. R. Whelan, A. Shivayogimath, D. M. A. Mackenzie, P. Bøggild, T. J. Booth, Chem. Mater. **28**, 3789 (2016).

[12] D. Tahir and S. Tougaard, J. Phys.: Condens. Matter. **24**, 175002 (2012).

[13] I. Platzman, R. Brener, H. Haick, and R. Tannenbaum, J. Phys. Chem. C **112**, 1101 (2008).

[14] G. Fritz-Popovski, F. Sosada-Ludwikowska, A. Köck, J. Keckes, and G. A. Maier, Sci. Rep. **9**, 807 (2019).

[15] C. Taxén, SKB Technical Report, R-02-23, (2002).

[16] J.-P. Wang and W. D. Cho, ISIJ Int., **49** 1926 (2009).

[17] J. W. McPherson, Reliability Physics and Engineering (Springer, New York, 2010) 2nd ed., p. 5.

[18] M. Oizumi, K. Aoki, and Y. Fukuda, Jpn. J. Appl. Phys. **40**, L603 (2001).

[19] A. G. Asuero, A. Sayago, and A. G. González, Anal. Chem. **36**, 41 (2006).

[20] H. Nagai and M. Sato, Molecular Precursor Method for Fabricating p-Type Cu_2O and Metallic Cu Thin Films, Modern Technologies for Creating the Thin-film Systems and Coatings (2017).

CHAPTER 4

MOISTURE BARRIER PROPERTIES OF SINGLE LAYER GRAPHENE

4.1. Introduction

Based on the impermeability properties of graphene, it has been expected to protect Cu surface from oxidation due to moisture, leading to the Cu lifetime improvement for long-term storage in the environment. SLG grown by CVD on Cu foil was reported the evidence of the moisture barrier properties of graphene on the Cu surface, however, high-quality SLG with larger grain-sized has been required [1–5].

In this chapter, the moisture barrier properties of high-quality SLG films deposited on the Cu surface by high-temperature CVD were demonstrated. Although low-temperature deposition is more appropriated for interconnect fabrication, the evidence of this test can be determined the future target of graphene applications. The correlation between SLG quality and Cu oxide thickness after THS test was also investigated by SE using a non-uniform SLG film deposited on the Cu surface. Two comparative SE models were presented in this work. The advanced model was developed to describe the relative amount of Cu oxide formed among the non-uniform SLG film in more precise detail.

4.2. Experimental methods

In this work, two analytical experiments to investigate the moisture barrier properties of SLG on a Cu surface were performed. In the first experiment, a uniform SLG film was deposited on a Cu surface; then, the performance of SLG against oxidation from moisture was investigated and compared with that of a bare Cu sample. Fig. 4.1 shows the sample structures of SLG-coated Cu and bare Cu. A 1000-nm-thick Cu(111) film was deposited on a c-plane sapphire substrate by magnetron sputtering at 220°C. Then, the uniform SLG film was grown on a heteroepitaxial Cu (111)/sapphire substrate by CVD using CH_4 gas as the C precursor [6–8], as described in chapter 2.

The quality of the uniform SLG film was measured by Raman spectroscopy at three random measurement points on the SLG film after transferring to the SiO_2/Si substrate with 532 nm excitation, as shown in Fig. 4.1(c). Two high-intensity peaks located at 1587 and 2680 cm^{-1} are G and 2D bands, respectively [9,10]. The high-intensity ratios of 2D/G bands are evidence of single-layer graphene film [10,11]. The very low intensity of the defect-related D band at ~1350 cm^{-1} confirms the high quality of this SLG film [9,10,12]. The large grains of SLG approximately 50–100 µm sizes [6] were examined to determine the near-ideal graphene grain size for protecting a Cu surface, as the final target of this study.

A bare Cu sample without graphene coating was also prepared and annealed in the same temperature as the procedures for CVD-SLG for an unbiased comparison with the SLG/Cu/sapphire sample. All samples were kept in THS chamber at the standard condition of 85°C/85% RH for accelerating Cu oxidation. Based on the proposed model of lifetime prediction [Chapter 3 equations (12) or (13)], the period of THS test at the standard condition of 85°C/85% RH can be converted to the actual lifetime at use condition of 27°C/60% RH, as shown in Table 4.1. To confirm the long-term reliability of Cu metallization over 100 years, which is our target lifetime, the THS test at 85°C/85% RH should be carried out over 25 h (>100 years at 27°C/60% RH). The THS test for all experiments in the following chapter had been conducted for 100 h to confirm almost 4 times of the expected lifetime of Cu (>100 years). After 25, 50, and 100 h of THS testing, the changes in the surface color of all samples were observed by OM. The surface chemistry of Cu and SLG/Cu was analyzed by XPS [13−16]. Cu 2p and O 1s XPS spectra were investigated using an Al X-ray source at 1486.6 eV with the measured spot diameter of ~110 µm. The relative changes in the atomic concentration ratio of O to Cu elements, which was determined by XPS, were evaluated to estimate the oxidation of the Cu surface.

The properties of the SLG film against the permeation of O can be described by first-principles molecular dynamics (FPMD) and activation energy calculations within the framework of the density functional theory implemented in the STATE program package [17]. The FPMD simulation was conducted by the velocity scaling method to keep the temperature constant during the simulation [17].

Table 4.1 THS test duration at 85°C/85% RH converts to the actual lifetime at 27°C/60% RH.

THS test 85°C/85% RH	25 h	50 h	100 h
Actual condition 27°C/60% RH	~98 years	~197 years	~395 years

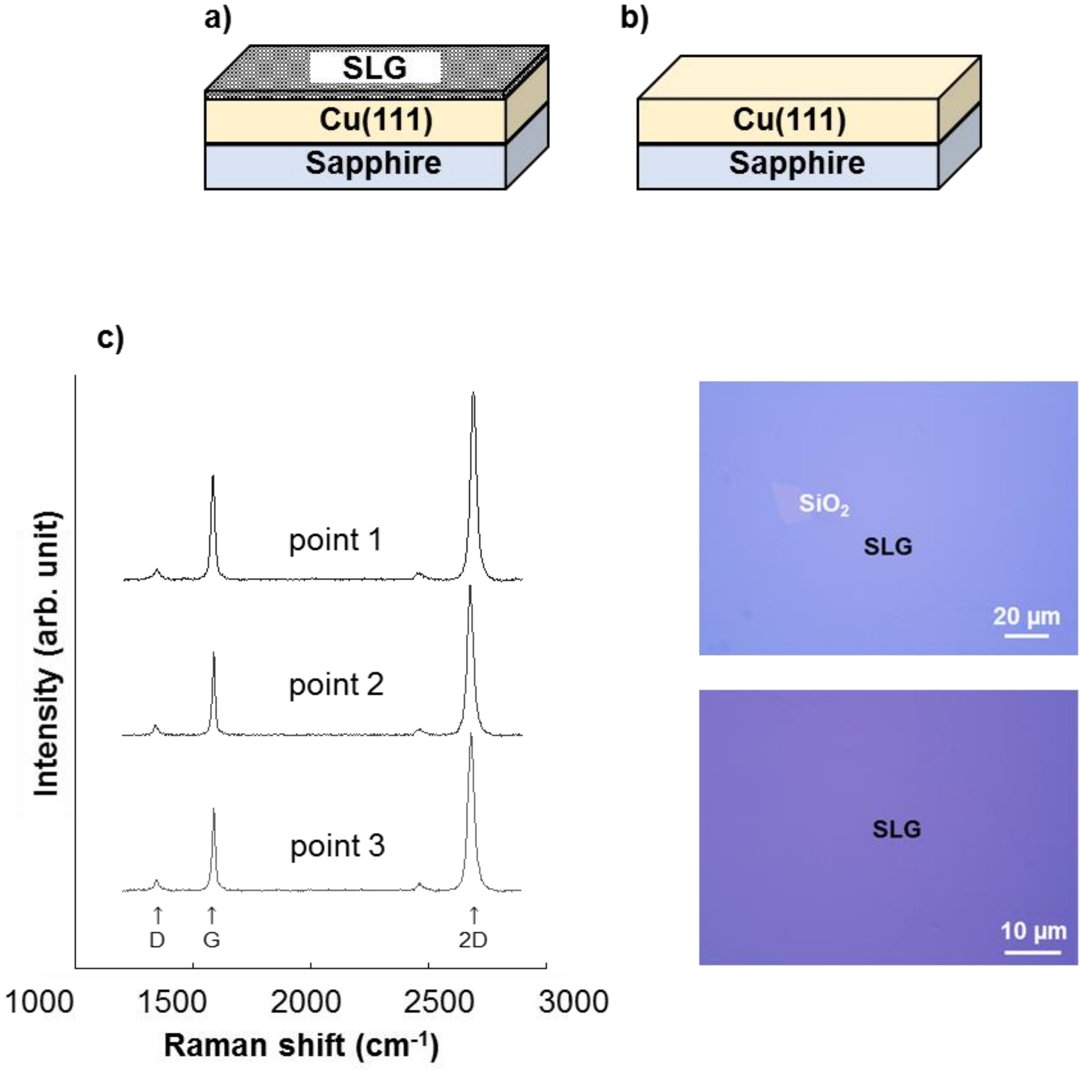

Figure 4.1. Panels (a) and (b) showing SLG/Cu and bare Cu samples, respectively, and (c) Raman spectra of three random points on SLG surface. (By courtesy of Prof. Ago group)

In the second experiment, the dependence of moisture barrier properties of SLG on the non-uniform SLG film (mixing ratio or volume fraction of SLG and a-C) were demonstrated. Here, a non-uniform SLG film was prepared in similar processes with those of the uniform SLG deposition as in the first experiment, accidentally, it became non-uniform film owing to some failures occurred during the CVD process. After THS testing, SE was carried out to measure the SLG quality and Cu oxide thickness on the Cu surface by the collaboration with Horiba Techno Service. SE technique is very useful for determining the optical constants, namely, refractive index (n), extinction coefficient (k), and the thicknesses of various thin films determined from the best fitting of ellipsometric results [18−22]. The non-uniform SLG, as shown in Fig. 4.2(a), was measured after 200 h of THS testing at twelve measurement points on the sample surface using spectroscopic phase-modulated ellipsometer (UVISEL^{TM}2) in the wavelength range of 206–824 nm (1.5–6.0 eV) with the measured spot diameter of ~500 μm at an incident angle of 70°. The optical constants (n and k) and the thicknesses of SLG and Cu-oxide layers cannot be obtained directly from ellipsometric results, but they can be derived from the assumed models, as shown in Fig. 4.2(b–c). On the basis of the models, the ellipsometric parameters ψ and Δ were also generated and then compared with those of the measured results. The algorithm of data fitting between the generated parameters based on the SE model and parameters from the measurement was performed [18]. During the data fitting, all the generated models can be changed to minimize MSE between the measured and generated parameters [18].

In this work, the basic model was proposed at the beginning, as shown in Fig. 4.2(b), to understand the correlation for the C-based thin films by focusing on the mixing composition ratios of SLG to a-C in the non-uniform SLG layer and the thickness of Cu oxidation. This model has the simplest structure for analyzing layer thickness. The generated ellipsometric parameters are fitted with the measured parameters to obtain a minimum acceptable MSE. The mixing ratios of SLG to a-C in each measured point was estimated from the proportions of their n and k, as shown in Fig. 4.3. In the advanced model, as shown in Fig. 4.2(c), graphite in the SLG and the interface area between the SLG and Cu oxide layers were introduced to obtain the best fitting of both ellipsometric parameters. Although it was difficult to identify the exact structure of the interface layer, it could be roughly determined from the optical constants which obtained results like metallic properties. It was probably due to the diffusion of Cu atoms into the C layer. The mixing ratios of SLG to a-C to graphite within each measurement point was also estimated from the proportions of their n and k, as shown in Fig. 4.4. The obtained results based on the advanced model were compared with those of the basic model.

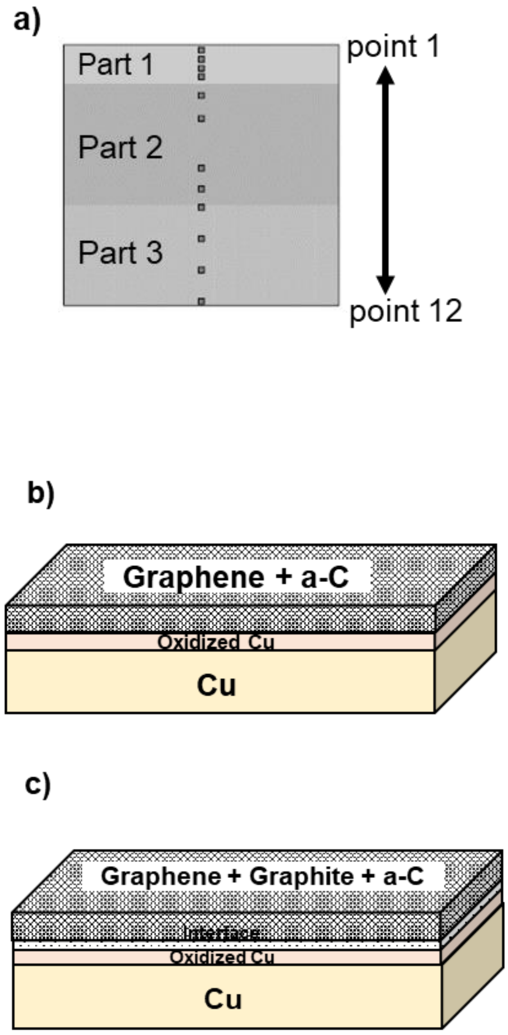

Figure 4.2. (a) Schematic of three parts SE measurement on non-uniform SLG/Cu surface, (b) and (c) sample structure in the basic and advanced models, respectively.

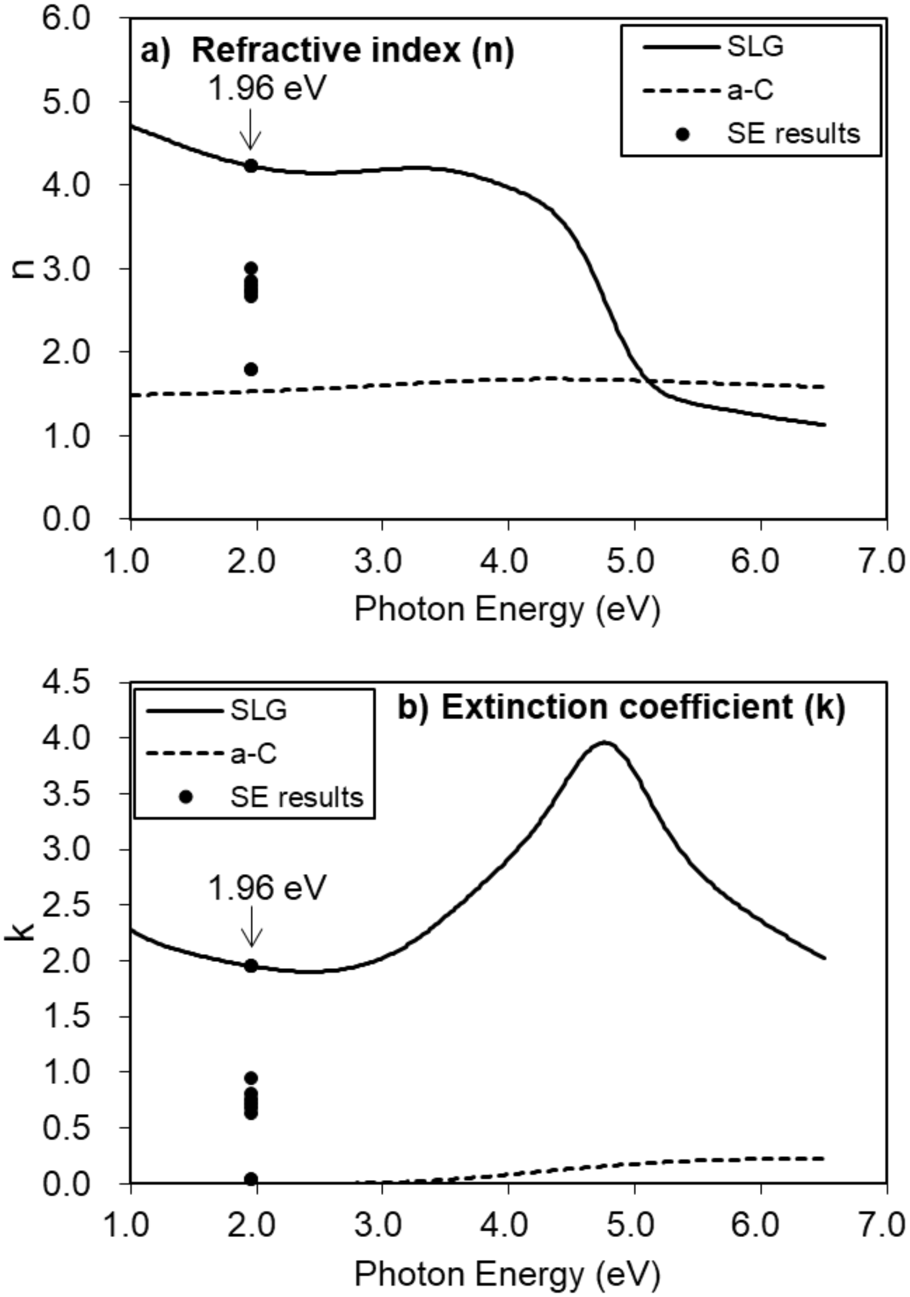

Figure 4.3. Optical constant of mixing composition of C-base film in the basic model. Panels (a) and (b) showing refractive index (n) and extinction coefficient (k), respectively.

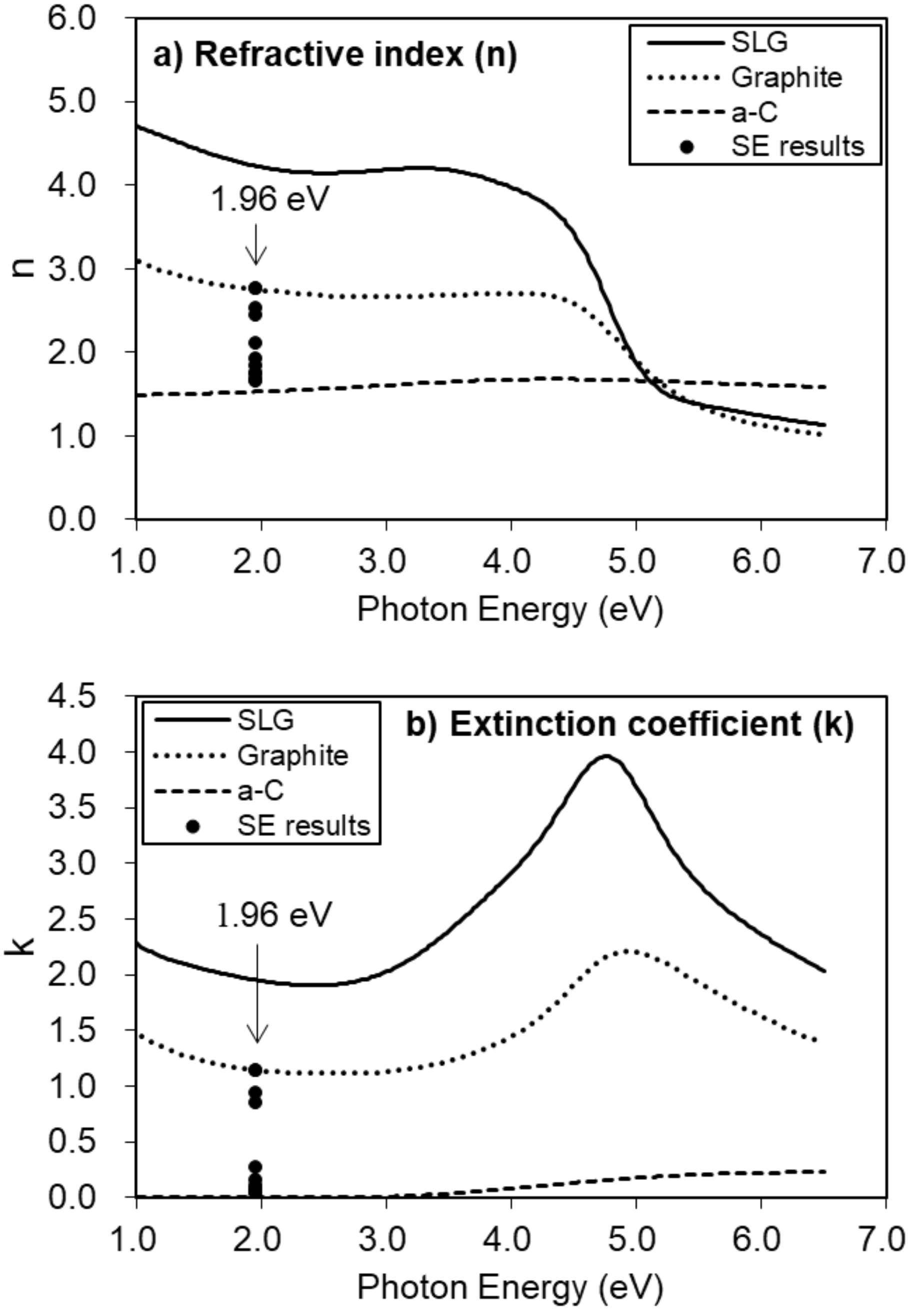

Figure 4.4. Optical constant of mixing composition of C-base film in the advanced model. Panels (a) and (b) showing refractive index (n) and extinction coefficient (k), respectively.

4.3. Results and discussion

4.3.1. Comparison between uniform SLG/Cu and bare Cu after THS test

The changes in surface color were observed before and after 25, 50, 100 h of the THS testing by OM. Figure 4.5(a–d) shows the change in the surface color of SLG/Cu and comparing to those of bare Cu surface as shown in Fig. 4.5(e–h). Most of the areas of the SLG/Cu surface still appeared shiny after 100 h of the THS test. It indicates that most of the Cu areas were covered by the SLG film which protects the Cu surface from oxidation. Small dark lines appeared in the SLG/Cu surface after 100 h of the THS test probably caused by O diffusion through the areas of SLG grain boundaries [23,24]. In the case of the bare Cu surface without the SLG coating, the surface gradually changed in color and became uniformly darker after 100 h of the THS test, which obviously indicates the oxidation of the Cu surface.

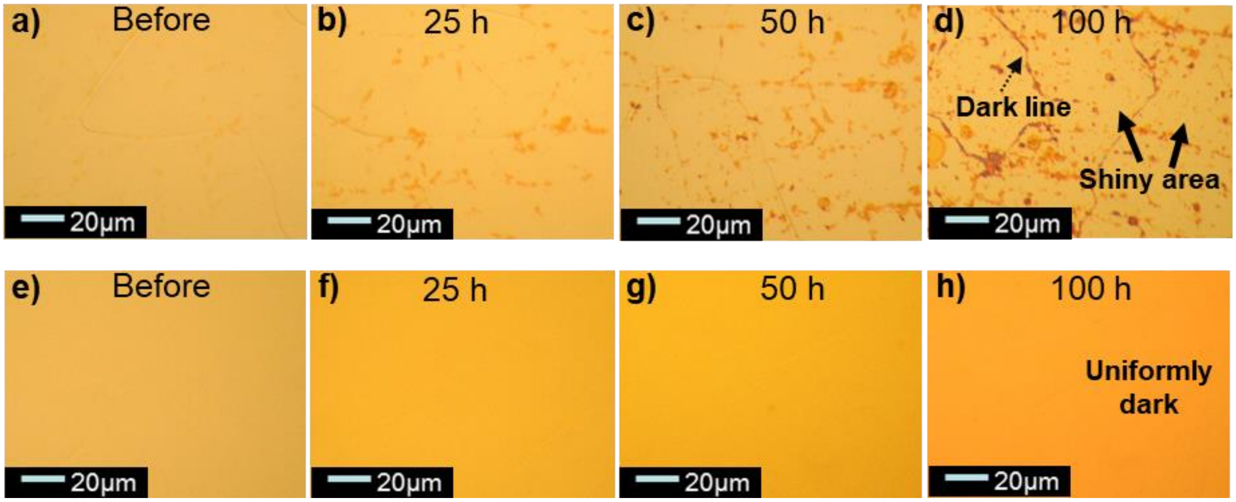

Figure 4.5. Optical images of (a-d) SLG/Cu and (e-h) bare Cu surface observed before and after 25, 50, and 100 h of THS test.

The oxidation states of the Cu, namely, Cu_2O and CuO, were analyzed on the basis of the Cu 2p XPS spectra of five measurement points on the sample surface. The center of the Cu 2p peak located in the range of 932.6 to 932.2 eV corresponds to the metallic Cu and Cu_2O [13−16]. Cu_2O is the low-oxidation state of metallic Cu, and it rapidly forms on the Cu surface after exposure to air

[16]. After Cu surface was continuously oxidized, the high-oxidation state as CuO was evidently observed at ~933.6 eV [14,16]. For the SLG/Cu surface, there were no peaks separated from the Cu or Cu_2O in the Cu 2p spectra. It reveals just a slight reduction in the peak intensity after 100 h of the THS test. It seems that metallic Cu was slightly oxidized to form Cu_2O only, as shown in Fig. 4.6(b) as compared with Fig. 4.6(a) on the same vertical scale. Corresponding to the small dark lines in Fig. 4.5(d), a slight change in Cu 2p spectra probably occurred owing to the XPS measurement area also covering the Cu oxidation area along SLG grain boundaries. Besides, these results can confirm the state of oxidation along SLG grain boundaries during the THS testing with only the Cu_2O formed. On the other hand, the Cu 2p spectra of the bare Cu surface before the THS test already exhibited a small-intensity CuO peak, as shown in Fig. 4.7(a). After 100 h of THS test, the Cu 2p spectra appeared the clear CuO peak due to the complete oxidation of Cu surface, as shown in Fig. 4.7(b). The shake-up peaks between 940 and 944 eV in Fig. 4.7(b) also indicate the existence of CuO. The reduction in Cu or Cu_2O peak was according to the increasing of O content from Cu oxidation.

Figure 4.8 shows the atomic concentration ratios of O to Cu within the measurement area before and after 25, 50, and 100 h of the THS test determined by XPS. Before THS testing, the O/Cu ratio of the bare Cu surface was higher than that of SLG/Cu surface. The results were in accordance with the difference in the shape of the Cu 2p between the bare Cu surface [Fig. 4.7(a)] and the SLG/Cu surface [Fig. 4.6(a)]. In the case of the bare Cu surface, the O/Cu ratio increased with THS test time and appeared more linearly than those of the SLG/Cu surface. Corresponding to optical images, XPS results clearly indicate that the Cu surface without SLG coating was easily oxidized by O atom from moisture. In the case of the SLG/Cu surface, the O/Cu ratio increased after 25 h, then the increasing rate of this content gradually decreased after a long time of the THS testing. Five measurement points of XPS on the SLG/Cu surface indicate a slight difference in the O/Cu ratios owing to non-uniform oxidation within each measurement point. From the results, it is considered that SLG performs as a barrier film to protect the Cu surface under SLG coating.

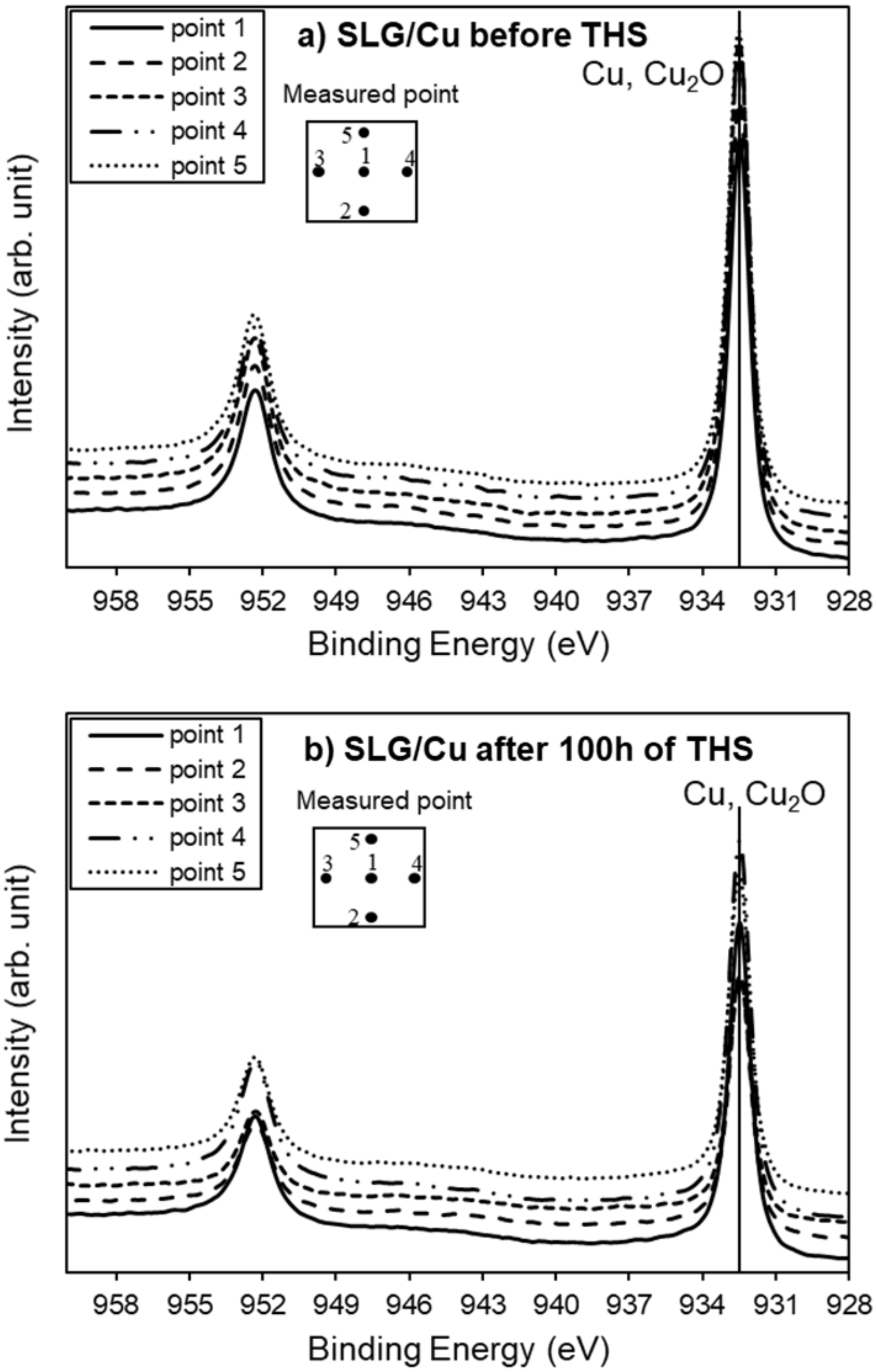

Figure 4.6. Cu 2p XPS spectra of SLG/Cu surface measured (a) before and (b) after 100 h of THS test.

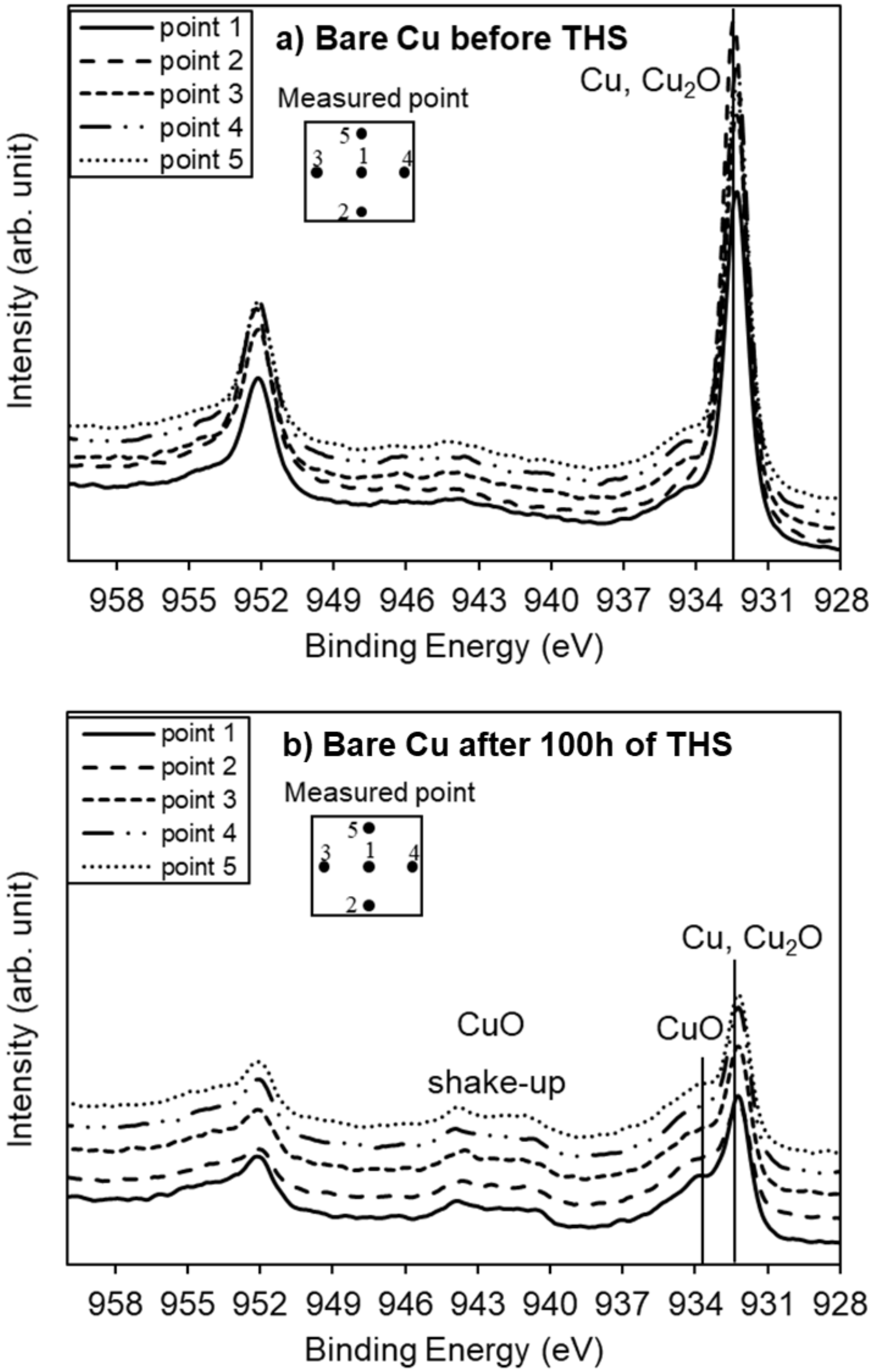

Figure 4.7. Cu 2p XPS spectra of bare Cu surface measured (a) before and (b) after 100 h of THS test.

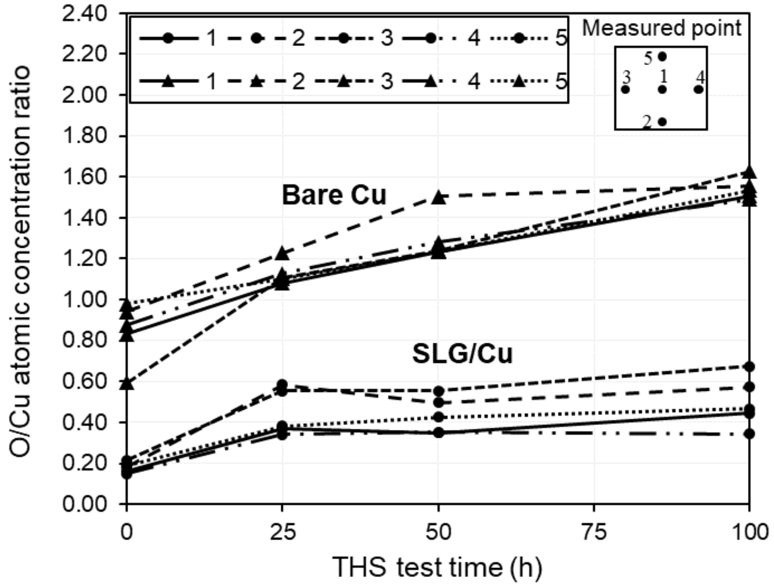

Figure 4.8. Atomic concentration ratios of O to Cu measured by XPS on SLG/Cu and bare Cu surfaces measured before and after 25, 50, and 100 h of THS test.

In order to confirm the barrier properties of SLG theoretically, FPMD simulation was performed, as shown in Fig. 4.9 by Okada group (University of Tsukuba). The O atom diffusion through the SLG layer under the periodic boundary condition for lateral and normal directions of SLG, two layers of SLG was simulated as shown in Fig. 4.9 in which molecular diffusion is distinguished by its position with respect to the inner or outer of the bilayer structure. After 20 ps of molecular dynamics (MD) simulation, O atoms could not penetrate through the SLG structure to the opposite side. Each O atom only forms a chemical bond with a C atom of the SLG. In order to understand the mechanisms by which the SLG surface obstructs the penetration of O atoms, the monolayer model and the diffusion energy that an O atom required to pass through the SLG layer were considered, as shown in Fig. 4.10. Figure 4.10 shows the correlation of the barrier energy and distance between an O atom and the SLG surface. The energy continually increased as the O atom moved to the graphene layer. The activation energy of the O atom to penetrate through the SLG surface (at a distance of 0 Å) was 22.71 eV and then continually decreased after moving out of the SLG surface. The obtained energy was very high and it was reasonable that O atoms did not have enough energy to pass through the SLG surface. From both results of simulation and experiment, they indicate that the large-grain SLG can protect the Cu surface from oxidization by moisture.

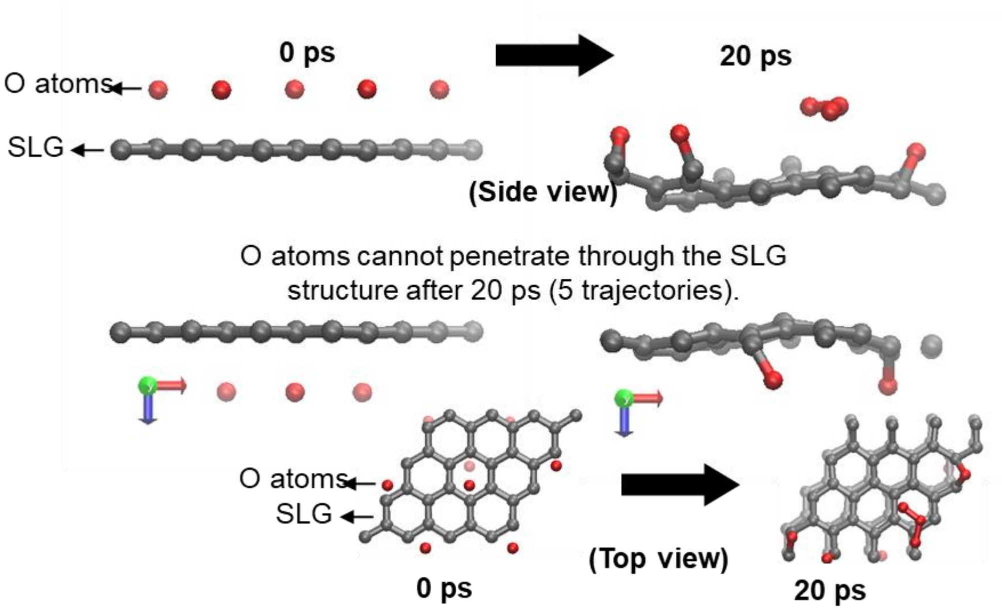

Figure 4.9. Initial atomic geometry and final atomic geometry of 20 ps. FPMD simulation of O atoms on the top and bottom surfaces of a two-layer graphene structure at 1000 K. (By courtesy of Prof. Okada group)

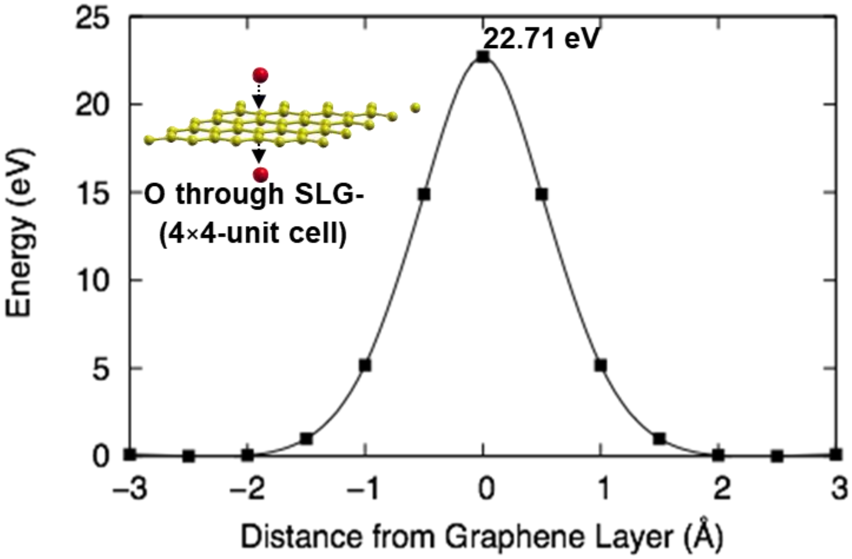

Figure 4.10. Energy barrier for O atom diffusion through SLG film. (By courtesy of Prof. Okada group)

4.3.2. Cu-oxide thickness dependence on SLG quality in non-uniform SLG/Cu

In the above section, it was found that high-quality SLG with large grains was able to protect the Cu surface from oxidation by moisture. However, it was still practically difficult to deposit such an SLG film with large grains at a low temperature. Therefore, the barrier performance dependence on the SLG film quality were also demonstrated.

At the beginning, the basic model [Fig. 4.2(b)] was used to fit the ellipsometric data to obtain the results as shown in Table 4.2. The mixing ratios of SLG to a-C was found to depend on the proportions of n and k of so-called SLG and a-C. The results of Cu-oxide thickness within the measurement points were also shown in Table 4.2. The non-uniform SLG surface was classified by color into three main parts, as shown in Fig. 4.2(a). The first part (points 1–4) exhibited the highest values of optical constants (n and k) related to the highest ratio of SLG. Most importantly, the Cu-oxide thickness among these parts was the smallest according to the highest ratio of SLG. The Cu-oxide thickness was thicker along with decreasing SLG ratio, as in the second (points 5–8) and third (points 9–12) parts, as shown in Table 4.2. However, the Cu-oxide thickness in the third part was a bit thinner than those of the second part probably due to the thinner C layer in the third part. The correlation between Cu-oxide thickness and a-C to SLG mixing ratios can be briefly explained from the basic model, as shown in Fig. 4.11. The measured areas with a low a-C (high SLG) ratio indicate the thicker Cu-oxide layer, whereas the areas with a higher a-C (low SLG) ratio became a poor barrier which could not protect the Cu surface from oxidation.

Figure 4.12(a–c) shows the OM plan view of each part. In the first part [Fig. 4.12(a)], the color of the Cu surface was relatively light, indicating a low level of Cu oxidation which was in agreement with the SE results. In the second part [Fig. 4.12(b)], light and dark-colored areas were mixed, and the color contrast was higher in this part than that of the other parts. These results indicate that both non-oxidized and Cu-oxide areas were combined according to the mixed SLG and a-C structure shown by the SE results. In the third part [Fig. 4.12(c)], the surface was darker than that of the first part, however, the color contrast is more uniform than that of the second part. The SE results of the third part indicate the dominant a-C ratio with the thinner layer than those of the second part, leading to more uniform oxidation of the third part.

Table 4.2. Thicknesses of Cu-oxide layer and C-based thin films with mixing ratios from the basic SE model.

Point	Thickness (Å)		Mixing ratio of a-C to SLG		Optical constant at 633 nm (~1.96 eV)		MSE
	CuO_x	C	a-C	SLG	n	k	
1	8.2	2.1	0	100	4.226	1.952	3.252
2	19.3	4.8	0.4	99.6	4.215	1.944	6.137
3	26.4	6.3	0	100	4.226	1.952	7.140
4	49.9	8.5	0	100	4.226	1.952	11.339
5	160.5	31.7	48	52	2.987	0.947	10.223
6	133.6	24.2	53.8	46.2	2.844	0.808	6.517
7	123.5	22.6	57.6	42.4	2.75	0.717	5.820
8	124.2	22.9	55.9	44.1	2.792	0.757	5.922
9	112	15.7	59.6	40.4	2.703	0.672	4.732
10	104.2	11.8	61.5	38.5	2.656	0.626	4.223
11	108.9	7.9	100	0	1.791	0.036	4.361
12	108.8	9.8	100	0	1.791	0.036	4.620

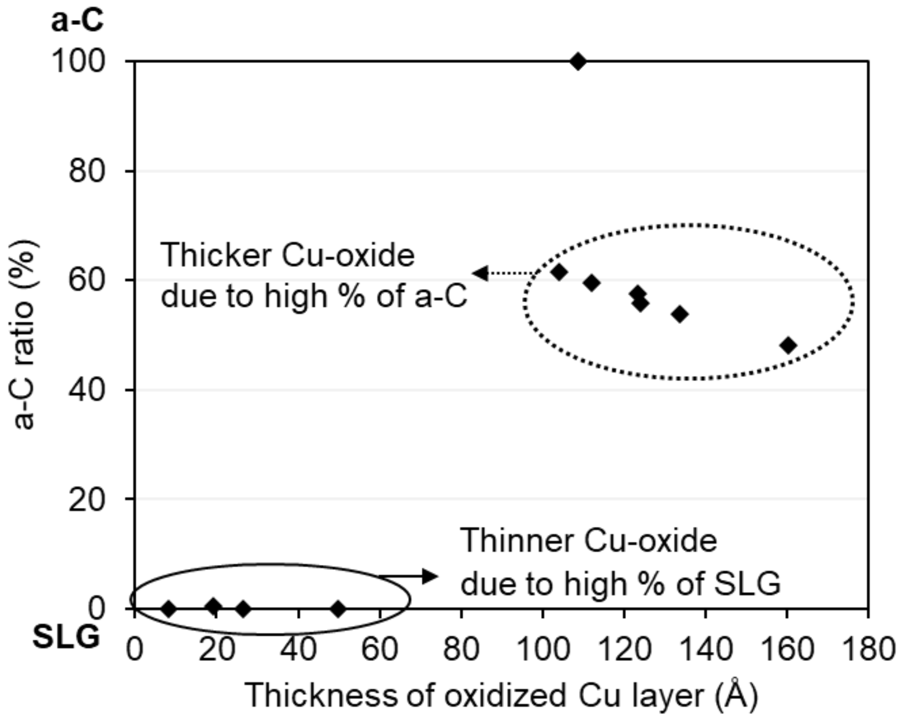

Figure 4.11. Relationship between the relative amount of a-C and Cu-oxide thickness from the basic model of SE.

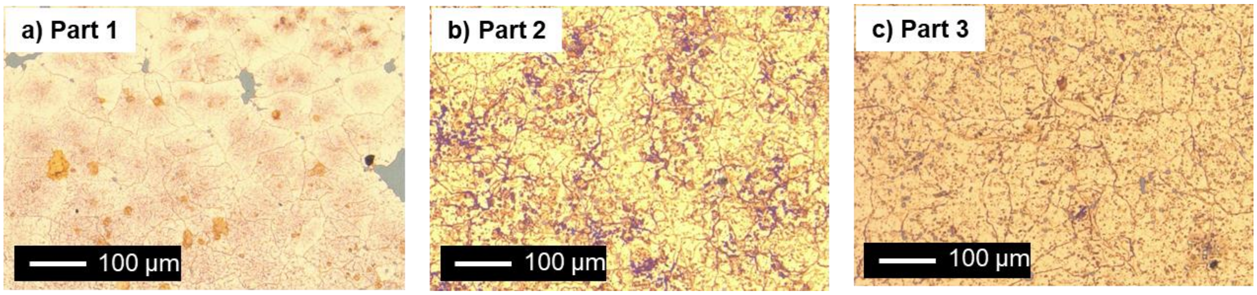

Figure 4.12. Three main parts of the non-uniform SLG/Cu surface observed by OM: (a) part 1, (b) part 2, and (c) part 3.

The thickness of the Cu-oxide layer varied in spite of the same SLG ratio of 100%, as noted in Fig. 4.11. A more precise SE model was required for further analysis. Therefore, an advanced model was developed by introducing optical parameters of graphite (Fig. 4.4) in the SLG film and the interface layer between SLG and Cu-oxide layers, as shown in Fig. 4.2(c). Better fitting with lower MSE values of the measured parameters was obtained using the advanced model. MSE values of the advanced model were lower than those of the basic model at all measured positions. Figure 4.13(a–b) shows examples of data fitting, which were obtained from measurement point 7, as in Fig. 4.2(a), for comparison between the measured parameters and parameters generated from the basic and advanced models, respectively. Table 4.3 shows the SE results based on the advanced model. The correlation between the a-C ratio and the thickness of the Cu-oxide layer was compared, as shown in Fig. 4.14.

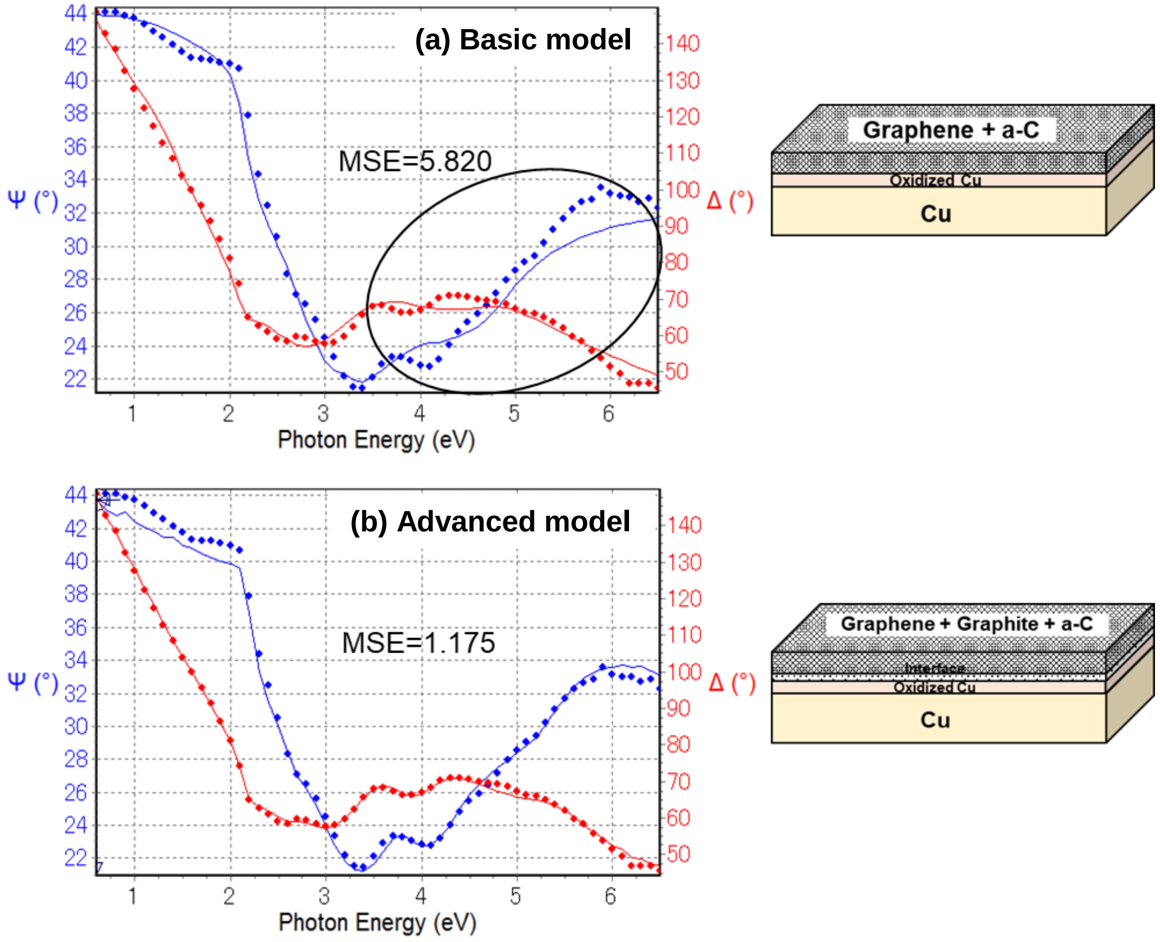

Figure 4.13. Ellipsometric parameters fitting based on the generated parameters from the (a) basic and (b) advanced models.

Based on the results of n and k from Table 4.3, they imply the mixing ratios of carbon allotropes that compose of the so-called a-C, graphite, and graphene. The overall correlation between the mixing ratios of a-C to SLG to graphite and the Cu-oxide thickness was similar to those of the obtained results from the basic model, supporting the findings based on the basic model. However, there was a negative correlation between the a-C ratio and the Cu-oxide thickness in the first part, as shown in Fig. 4.14 and Table 4.3. By introducing the graphite parameters, it was found that the C layer in the first part (points 1–4 from Table 4.3.) consisted of a mixture of graphite and a-C, and the a-C ratio varied with the measured positions. The results are in accordance with the color variation in the OM image [Fig. 4.12(a)]. According to the correlation, high a-C ratios up to 24.7% (graphite ratio down to 75.2%) might lead to a smaller thickness of the Cu-oxide layer. It reveals that the Cu-oxide thickness at the areas of 100% graphite (points 3 and 4 in Table 4.3.) was thicker than the areas with a mixture of 24.7% a-C, 75.2% graphite and 17.7% a-C, 82.3% graphite at points 1 and 2, respectively, indicating a possibility of practical optimization of graphene film structure by not only enlarging the grains. Because the defect density or film density of the barrier layer can determine the amount of Cu-oxide, the crystalline structure of graphite or graphene, which composes of lower defects or higher film density than the non-crystalline structure of a-C, should have shown the higher efficiency in preventing the formation of Cu-oxide compared to a-C.

It is noted that the G, D, and 2D Raman bands measured on each area reveal just the existence of graphitic and defective C structures in each area. However, there were no significant differences in the spectra in spite of the different colors of different parts. As yet, it could not discuss the structural difference by Raman spectra, then the further study has been required to support the structures of C determined using the advanced model of SE.

Table 4.3. Thicknesses of Cu-oxide layer and C-based thin films with mixing ratios from the advanced SE model.

Point	**Thickness (Å)**			**Mixing ratio of a-C to SLG to graphite**			**Optical constant at 633 nm (~1.96 eV)**		**MSE**
	CuO$_x$	**Interface**	**C**	**a-C**	**SLG**	**Graphite**	**n**	**k**	
1	5.0	12.0	23.7	24.7	0.1	75.2	2.432	0.851	0.840
2	23.2	11.3	24.5	17.7	0.0	82.3	2.522	0.938	1.678
3	39.1	11.4	16.1	0.0	0.0	100.0	2.751	1.144	1.366
4	71.1	13.2	16.4	0.0	0.0	100.0	2.751	1.144	2.077
5	205.6	10.1	24.3	81.9	17.2	0.9	1.912	0.157	3.888
6	168.8	7.0	14.7	92.6	5.5	1.8	1.657	0.045	1.747
7	154.2	6.1	13.8	92.3	7.2	0.5	1.675	0.046	1.175
8	156.5	6.3	13.0	92.7	6.0	1.4	1.660	0.044	1.224
9	134.8	5.0	9.6	85.7	14.3	0.0	1.828	0.108	0.957
10	120.2	4.4	6.9	75.0	25.0	0.0	2.100	0.274	1.501
11	120.5	3.9	14.6	88.9	11.1	0.0	1.754	0.074	0.957
12	122.0	3.9	20.0	89.5	10.5	0.0	1.740	0.068	1.463

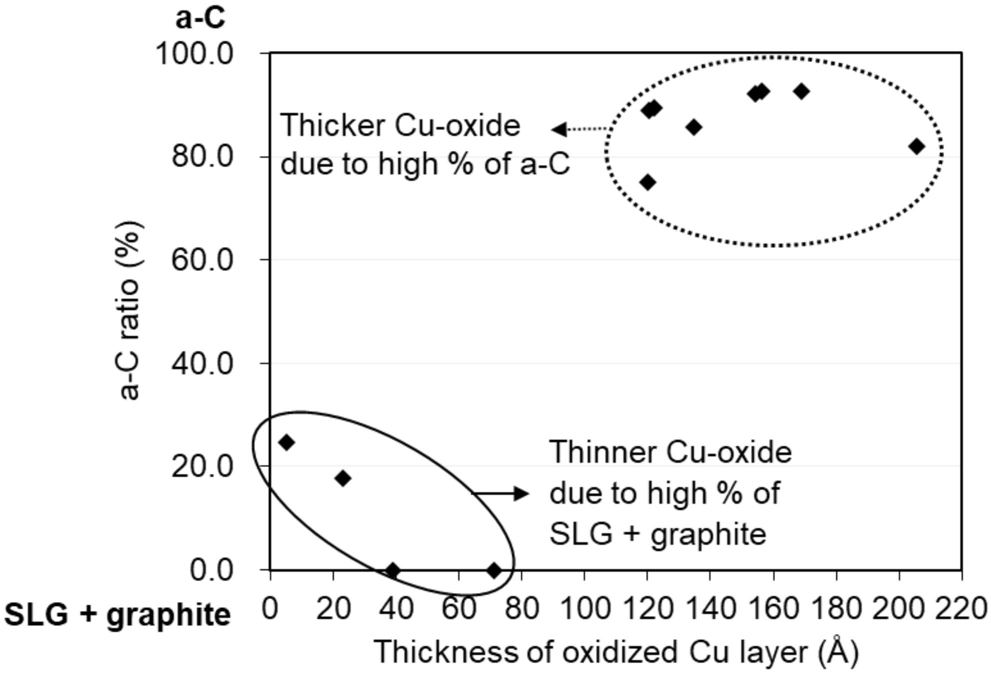

Figure 4.14. Relationship between relative amount of a-C and Cu-oxide thickness from the advanced model of SE.

4.4. Summary and conclusions

The moisture barrier properties of a high-quality large-grain SLG deposited on a Cu(111)/sapphire substrate by CVD were investigated. After the THS test at 85°C/85% RH (>25 h), OM and XPS clearly indicate that SLG coating can protect the Cu surface from oxidation by moisture and only small areas of Cu under SLG grain boundaries were oxidized. The barrier efficiency of SLG to prevent the penetration of O atoms was also confirmed by ab initio MD simulation. The first-principles simulation of the activation energy indicates that the O atoms do not have enough energy to pass through the SLG structure. The SE was then used to evaluate the correlation between Cu-oxide thickness and SLG quality on the Cu surface. The results indicate that high-proportion of graphite or graphene areas can prevent the oxidation of the Cu surface along with the potential optimization of the film structure. Simulation and measurement results reveal that the increase in SLG grain size and the elimination of grain boundaries should be provided to improve the performance of the SLG barrier layer in preventing the oxidation by moisture.

References

[1] F. Zhou, Z. Li, G. J. Shenoy, L. Li, and H. Liu, ACS Nano. **7**, 6939–6947 (2013).

[2] C. Jia, J. Jiang, L. Gan, and X. Guo, Sci. Rep. **2**, 707 (2012).

[3] M. Galbiati, A. C. Stoot, D. M. A. Mackenzie, P. Bøggild, and L. Camilli, Sci. Rep. **7**, 39770 (2017).

[4] M. Schriver, W. Regan, W. J. Gannett, A. M. Zaniewski, M. F. Crommie, A. Zettl, ACS Nano. **7**, 5763–5768 (2013).

[5] P. Y. Huang, C. S. Ruiz-Vargas, A. M. van der Zande, W. S. Whitney, M. P. Levendorf, J. W. Kevek, S. Garg, J. S. Alden, C. J. Hustedt, Y. Zhu, J. Park, P. L. McEuen, and D. A. Muller, Nature **469**, 389–393 (2011).

[6] H. Ago, K. Kawahara, Y. Ogawa, S. Tanoue, M. A. Bissett, M. Tsuji, H. Sakaguchi, R. J. Koch, F. Fromm, T. Seyller, K. Komatsu, and K. Tsukagoshi, Appl. Phys. Express **6**, 075101 (2013).

[7] B. Hu, H. Ago, Y. Ito, K. Kawahara, M. Tsuji, E. Magome, K. Sumitani, N. Mizuta, K. Ikeda, and S. Mizuno, Carbon **50**, 57 (2012).

[8] C. M. Orofeo, H. Hibino, K. Kawahara, Y. Ogawa, M. Tsuji, K. Ikeda, S. Mizono, and H. Ago, Carbon **50,** 2189 (2012).

[9] A. Y. Lu, S. Y. Wei, C. Y, Wu, Y. Hernandez, T. Y. Chen, T. H. Liu, C. W. Pao, F. R. Chen, L. J. Li, and Z. Y. Juang, RSC Adv. **2**, 3008 (2012).

[10] A. C. Ferrari, J. C. Meyer, V. Scardaci, C. Casiraghi, M. Lazzeri, F. Mauri, S. Piscanec, D. Jiang, K. S. Novoselov, S. Roth, and A. K. Geim, Phys. Rev. Lett. **97**, 187401 (2006).

[11] C. F. Comanescu, Int. Semiconductor Conf., 2016, p.49.

[12] H. Iguchi, C. Higashi, Y. Funasaki, K. Fujita, A. Mori, A. Nakasuga, and T. Maruyama, Sci. Rep. **7**, 39937 (2017).

[13] J. P. Espinos, J. Morales, A. Barranco, A. Caballero, J. P. Holgado, and A. R. Gonzalez-Elipe, J. Phys. Chem. B **106**, 6921 (2002).

[14] S. Poulston, P. M. Parlett, P. Stone, and M. Bowker, Surf. Interface Anal. **24**, 811 (1996).

[15] S. Suzuki, Y. Ishikawa, M. Isshiki, and Y. Waseda, Mater. Trans. JIM **38**, 1004 (1997).

[16] J. Iijima, J. W. Lim, S. H. Hong, S. Suzuki, K. Mimura, and M. Isshiki, Appl. Surf. Sci. **253**, 2825 (2006).

[17] Y. Morikawa, K. Iwata, and K. Terakura, Appl. Surf. Sci. **11**, 169 (2000).

[18] N. Nabatova-Gabin, Y. Wasai, and T. Tsuboi, Curr. Appl. Phys. **6**, 833 (2006).

[19] S. Tanemura, L. Miao, S. Koide, Y. Mori, P. Jin, A. Terai, and N. Nabatova-Gabain, Appl. Surf. Sci. **238**, 360 (2004).

[20] L. Miao, P. Jin, K. Kaneko, A. Terai, N. Nabatova-Gabain, and S. Tanemura, Appl. Surf. Sci. **212-213**, 255 (2003).

[21] T. Tsuboi, Y. Wasai, and N. Nabatova-Gabain, IEICE Trans. Elec. **E87-C**, 2039 (2004).

[22] J.B. Gong, W. L. Dong, R. C. Dai, Z. P. Wang, Z. M. Zhang, and Z. J. Ding, Chin. Phys. B **23**, 087802 (2014).

[23] P. Y. Huang, C. S. Ruiz-Vargas, A. M. van der Zande, W. S. Whitney, M. P. Levendorf, J. W. Kevek, S. Garg, J. S. Alden, C. J. Hustedt, Y. Zhu, J. Park, P. L. McEuen, and D. A. Muller, Nature **469**, 389 (2011).

[24] S. Chen, L. Brown, M. Levendorf, W. Cai, S. Ju, J. Edgeworth, X. Li, C. W. Magnuson, A. Velamakanni, R. D. Piner, J. Kang, J. Park, and R. S. Ruoff, ACS Nano **5**, 1321 (2011).

CHAPTER 5

STACKED GRAPHENE LAYERS TO IMPROVE MOISTURE BARRIER

5.1. Introduction

Based on the results in chapter 4, large-grained SLG can serve as an efficient impermeable film to prevent the penetration of moisture. However, some areas of the SLG-coated Cu surface were oxidized. The Cu-oxide areas were speculated as that the areas among the SLG grain-boundaries or defects [1].

In this chapter, two analytical experiments were performed. The first experiment was performed to demonstrate the Cu-oxide areas in the SLG-coated Cu among the grain boundaries or defective structures of graphene by Raman spectroscopy measurements. For improvement the reliability of graphene-coated Cu against Cu oxidation, an artificial multi-stacking SLG layers on CVD-SLG/Cu into DLG was demonstrated to eliminate the Cu oxidation through the defects and grain boundaries of the underneath SLG, as in the second experiment. In addition, TLG was also prepared by further stacking SLG on the DLG-coated Cu surface. The comparative oxidation resistances of DLG-coated Cu, TLG-coated Cu, SLG-coated Cu, and bare Cu surfaces was investigated after THS test. The sample surfaces were characterized using OM and XPS. The results indicate that the multiple stacking as DLG can improve the moisture barrier properties of the SLG-coated Cu surface by covering the underneath SLG grain boundaries. Moreover, TLG achieves as a highly efficient barrier that uniformly prevents oxidation of Cu surface by protecting the cross-points of grain boundaries in DLG. The mechanism of improvement by the first-principles simulation of overlapping graphene films result in an increased energetic barrier against the water diffusion through the different length of graphene overlap are also discussed in this chapter.

5.2. Experimental methods

High-quality large-grained SLG was grown on Cu/sapphire substrates using a previously reported CVD method [2,3] as described in chapter 4. A 1000-nm-thick Cu (111) film was deposited on a c-plane sapphire substrate via high-temperature sputtering. Then, SLG growth occurred on heteroepitaxial Cu (111)/sapphire substrates via ambient-pressure CVD at 1075℃ in CH_4 precursor gas. DLG- and TLG-coated Cu samples were prepared by stacking SLG on CVD SLG-coated Cu samples by a standard PMMA-assisted transfer method [2,4]. A bare Cu sample was also deposited on a sapphire substrate by sputtering and annealing in a quartz tube without the CH_4 precursor gas to facilitate comparison with that of graphene/Cu samples.

The THS test was conducted for 100 h under 85℃ and 85% RH conditions designed to accelerate oxidation. The first experiment was carried out to examine the Cu-oxide areas in the SLG-coated Cu surface after 100 h of THS test measured by Raman spectroscopy measurement at an excitation wavelength of 633 nm and spot diameter of ~1 μm. The second experiment was performed for testing the efficiency of stacking graphene samples comparing to SLG-coated Cu and bare Cu samples. Before and after 25, 50, and 100 h of THS test, all sample surfaces were observed by OM. Cu 2p, Cu LMM, and O 1s XPS spectra were investigated using an Al X-ray source (1486.6 eV) with a spot diameter of ~110 µm. The relative atomic concentration of O to Cu ratio was evaluated from the O 1s and Cu 2p spectra after background subtraction.

Unstitched grain boundaries of SLG were simulated for armchair graphene nanoribbons with hydrogenated edges by Okada group (University of Tsukuba) [5]. The diffusion of water through the overlapping graphene areas was simulated with various overlapped lengths. The O atom was fixed along the migration coordinate. In simulation, water migration began from the center of the graphene nanoribbon and ended among the overlapped graphene layers via the edge site. The energy barrier to water migration was estimated form the simulation results.

5.3. Results and discussion

5.3.1. Analysis of Cu oxidation on SLG-coated Cu surface

Regarding the previous report of moisture barrier properties of SLG-coated Cu surface, as in chapter 4, it was found that some areas of Cu surface were oxidized after 100 h of THS test. To confirm the hypothesis that the Cu oxidation occurred among the SLG grain boundaries or defects, dark and shiny areas of SLG-coated Cu surface were examined by Raman spectroscopy and also investigated the formation of Cu oxides comparing to those of the bare Cu surface, as shown in Fig. 5.1. For the Raman spectrum of SLG (Fig. 5.1), the D, G, and 2D peaks are located in the range of 1320–1327, 1585–1597, and 2640–2680 cm^{-1}[6,7], respectively. The existence of D peak corresponds to the defective structures of graphene. Comparative D and G peaks intensity ratio (I_D/I_G) among the dark and shiny areas of SLG-coated Cu surface after 100 h of THS test, the I_D/I_G intensity ratios of the dark color area was relatively higher than that of the shiny area. It indicates that there were many more defects among the dark area in a lengthwise direction which was like the grain boundary of SLG. In addition, the Raman spectra of the dark area exhibited various peaks of Cu_2O at 148, 219, and 525 cm^{-1}, and a peak located at ~630 cm^{-1} corresponded to CuO [8–11]. The intensity of Cu_2O and CuO peaks were larger in the spectrum of the SLG-coated Cu surface comparing to those of the bare Cu surface [Fig. 5.1]. In the case of shiny area on the SLG-coated Cu surface after 100 h of THS test, Raman spectrum did not exhibit the Cu-oxide peak. The results indicate that the efficiency of oxidation resistance of SLG got worse for long-term test due to the diffusion of moisture through the areas of grain boundaries. The defective areas of SLG can enhance the oxidation of the Cu surface.

To solve this problem, further development by multiple stacking of SLG has been performed to completely protect the Cu surface from moisture.

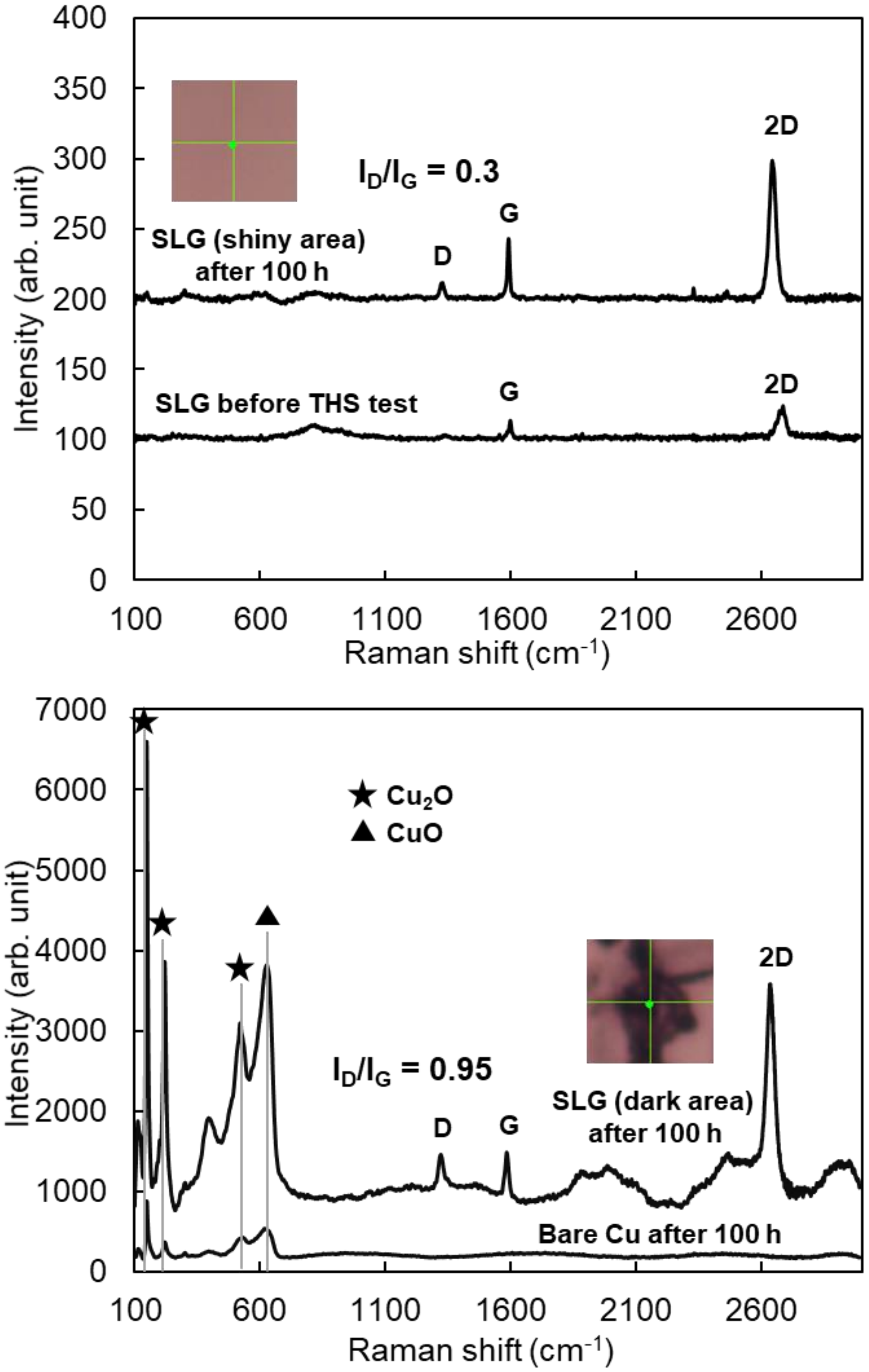

Figure 5.1. Raman spectra of SLG-coated Cu and bare Cu surfaces after 100 h of THS test. Spectrum of SLG (shiny area) shows small D peak without Cu-oxide peaks. Dark area of SLG and bare Cu spectra show various peaks of Cu_2O and CuO.

5.3.2. Artificial stacking of CVD-SLG to cover the underneath grain boundaries

In the second experiment, the oxidation resistance of SLG-coated Cu was improved by artificial stacking of CVD-SLG layers. Figure 5.2 shows the concept of SLG stacking as DLG-coated Cu surface expected to eliminate the Cu oxidation through the defects and grain boundaries in SLG-coated Cu surface, since the grain boundaries was covered by overlaying SLG grain. Further CVD-SLG stacking on the DLG-coated Cu surface as TLG was also carried out to improve the integrity of covering grain boundaries and defects.

5.3.2.1 Change of surface color during THS test observed by OM

All cases were prepared, including SLG-, DLG-, TLG-coated Cu and bare Cu samples, and then kept in THS test. Primary observation in the changes of the surface color was carried out by OM with comparing before and after variously THS testing times, as shown in Fig. 5.3. Comparing to its initial state [Fig. 5.3(a)], the bare Cu surface rapidly changed to a uniformly dark color after 25 h of THS test [Fig. 5.3(b)] and became continually darker after the long-term THS test [Fig. 5.3(c–d)]. The changes in color indicate that the Cu surface was oxidized upon exposure to high temperature and humidity. Most areas of the SLG-coated Cu surface after the THS test still be shiny [Fig. 5.3(f)], which was similar to the initial surface before the test [Fig. 5.3(e)]. However, in some areas appeared dark lines and spots [Fig. 5.3(f–h)] and became darker and larger size after long-term THS test [Fig. 5.3(b−d)]. The color change of SLG-coated Cu surface was qualitatively similar to the previous report, but the dark color areas were relatively larger in this study probably due to the higher density of defects. The DLG- and TLG-coated surfaces exhibit large shiny areas after the THS test. These results can confirm the expected effects of stacking SLG layers for covering the defects underneath. Although some small dark spots were observed on the DLG-coated Cu surface after long-term THS test, the shiny areas on the DLG-coated Cu surface were clearly larger [Fig. 5.3(j–l)] than those on the SLG-coated Cu surface [Fig. 5.3(f–h)]. The dark spots were more perfectly eliminated in the case of the TLG-coated Cu surface by showing a uniformly shiny surface without dark spots or dark lines after 100 h of THS test [Fig. 5.3(n–p)].

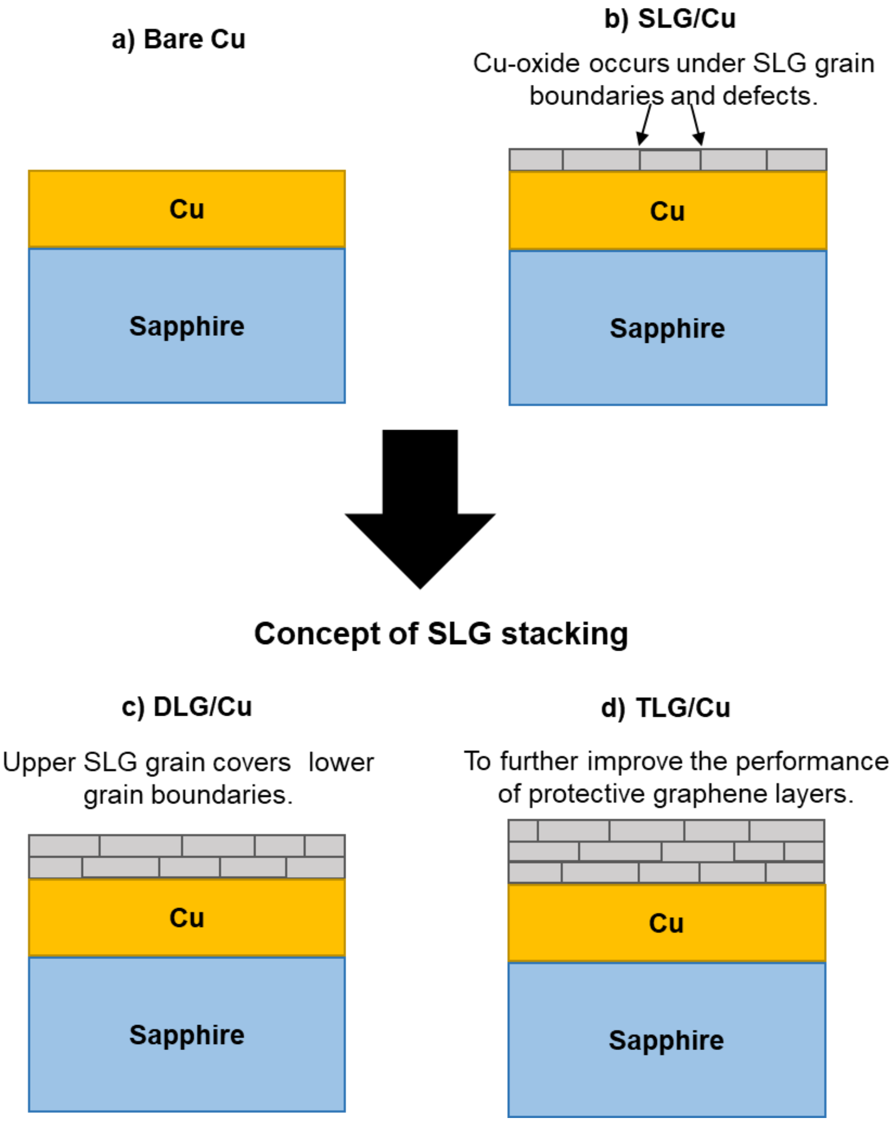

Figure 5.2. Structural models of the (a) bare Cu, (b) SLG-coated Cu, and stacking SLG layers as (c) DLG-coated Cu and TLG-coated Cu samples.

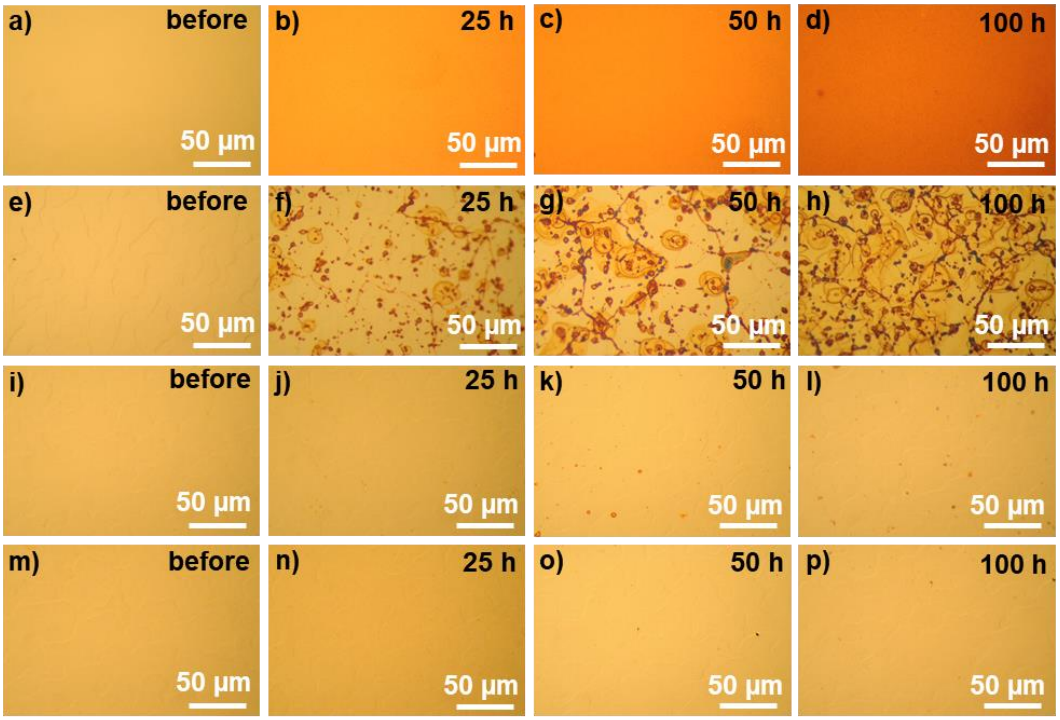

Figure 5.3. OM images of (a–d) bare Cu, (e–h) SLG-coated Cu, (i–l) DLG-coated Cu, and (m–p) TLG-coated Cu surfaces measured before and after different durations of THS test.

5.3.2.2 Evolution of Cu oxidation measured by XPS during THS test

The relative changes in the contents of O and Cu during the THS test were evaluated by XPS. A typical spectrum for each duration was shown in Fig. 5.4. The XPS peak intensity is associated with the average amount of the corresponding elements within the analyzed XPS depth. The primary analysis to confirm the components of metallic Cu, Cu_2O, and CuO in the Cu 2p spectrum was carried out, as shown in Fig. 5.4(A1–A4). The main peaks observed from 932.6–932.4 eV correspond to the metallic Cu and the low oxidation state as Cu_2O [12–15]. The high oxidation state as CuO is reflected by the peaks at ~933.6 eV, and its satellite peak was observed from 944.6–942.4 eV [12–14]. The metallic Cu and Cu_2O peaks can be distinguished clearly in the Cu LMM Auger spectrum, as shown in Figs. 5.4(B1–B4). The Cu 2p spectrum of the bare Cu surface before the THS test [Fig. 5.4(A1)] exhibited high-intensity peaks of metallic Cu and Cu_2O along with small CuO and CuO satellite peaks.

In the Cu LMM Auger spectrum of the bare Cu surface, the peaks at the binding energies of ~567.9 and ~570 eV correspond to the metallic Cu and Cu_2O [16,17], respectively. The Cu LMM spectrum of bare Cu before the THS test [Fig. 5.4(B1)] exhibited both metallic Cu and Cu_2O peaks, indicating that a layer of Cu_2O formed on the Cu surface upon exposure to air before the THS test. After THS test, the peaks corresponded to metallic Cu and Cu_2O in the Cu 2p spectrum [Fig. 5.4(A1)] decreased continually in contrast with the growth of CuO peak, indicating that Cu continued to be oxidized during the THS test. There was almost no metallic Cu observed after 100 h of test, indicating that the Cu surface within the measurement depth of XPS was fully oxidized, as shown in the Cu LMM Auger spectrum [Fig. 5.4(B1)].

The Cu 2p spectra of the SLG-, DLG-, and TLG-coated Cu surfaces before the THS test [Fig. 5.4(A2–A4)] exhibited the high-intensity peaks of metallic Cu and Cu_2O. In the Cu LMM Auger spectra [Fig. 5.4(B2–B4)], the presence of metallic Cu was much higher than that of Cu_2O. These results demonstrated the ability of the graphene layers to protect the Cu surface. Significant changes were observed in the Cu 2p spectrum of the SLG-coated Cu surface after long-term THS test [Fig. 5.4(A2)]. The peak of CuO appeared suddenly after 100 h of the THS test, and its intensity was greater than that of the Cu_2O peak. This change was consistent with the appearance of dark lines and spots, as observed by OM [Fig. 5.4(h)]. The Cu 2p spectra of the DLG- and TLG-coated Cu surfaces [Figs. 5.4(A3–A4)] indicate strong peaks of metallic Cu+Cu_2O components, whereas the CuO peaks were almost nonexistent. The Cu LMM Auger spectra of the DLG- and TLG-coated Cu surfaces [Fig. 5.4(B3–B4)] clearly indicate the presence of a large amount of metallic Cu after 100 h of THS test, in agreement with the large shiny areas observed on the Cu surfaces by OM [Fig. 5.4(i–p)].

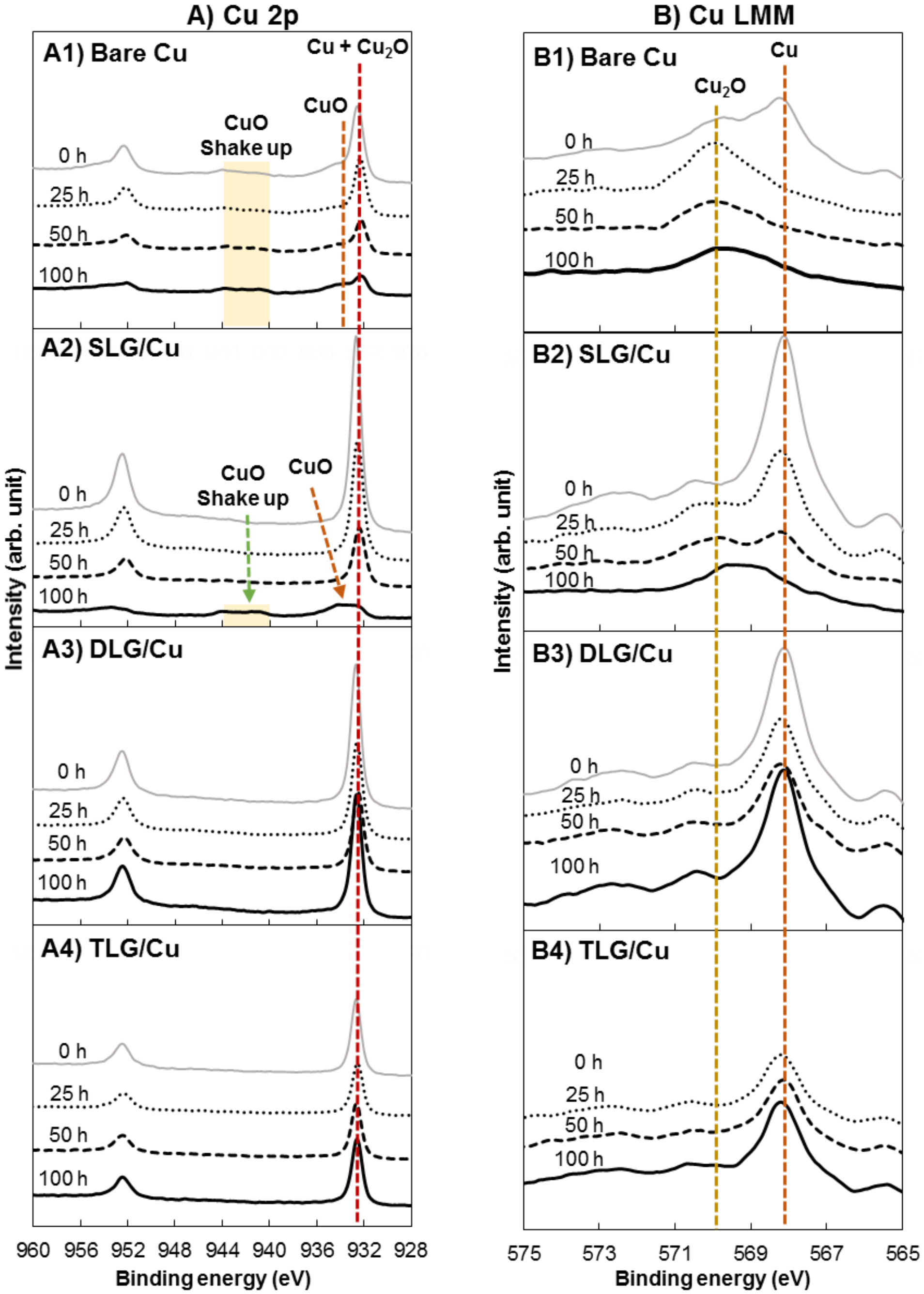

Figure 5.4 XPS spectra of (A) Cu 2p and (B) Cu LMM measured on bare Cu and graphene-coated Cu surfaces comparing before and after different durations of THS test.

The relative O/Cu atomic concentration ratios for each condition estimated from the Cu 2p and O 1s spectra; adsorbed O and C–O contents were not included when determining the concentration ratios [18,19], are shown in Fig. 5.5. Before the THS test, the O/Cu ratio of the bare Cu surface was higher than those of all the graphene-coated Cu surfaces owing to the rapid oxidation of Cu after exposure to air moisture. The increasing rate of the O/Cu ratio on the bare Cu surface was maximized after 25 h of the THS test and then decreased as the test continued, indicating the reduction of Cu_2O formation. It implies that the Cu-oxide layer performs as the passivation layer to slow down the further Cu_2O formation (just changing the existent Cu_2O to CuO) after the long-term THS test in the same vapor pressure.

For the SLG-coated surface, the O/Cu ratio increased linearly with the THS test time and then increased extremely quickly after 100 h of test due to the formation of CuO higher than that of bare Cu surface, as shown in inset Cu 2p curve fitting. These results were in accord with the presence of dark lines and spots investigated on the sample surface by Raman spectroscopy (Fig. 5.2) and the change in shape of the Cu 2p spectra (Fig. 5.5). For the DLG- and TLG-coated Cu surfaces, their O/Cu ratios increased slightly after 25 h of THS test and then remained stable.

A comparative results of Cu-oxide formation between the bare Cu and graphene-coated Cu surfaces by Raman spectroscopy (Fig. 5.1), OM images [Fig. 5.3(b–d) and (f–h)] and XPS results (Figs. 5.4 and 5.5) reveal that SLG could preserve the metallic Cu surface underneath for almost 50 h of the THS test; however, the efficiency of the SLG coating was reduced after long-term THS test as 100 h. Raman spectrum and OM images indicate the high Cu oxidation at the sites of defects and grain boundaries of SLG [Figs. 5.1 and 5.3(f–h)] comparing to that on the bare Cu surface [Fig. 5.1]. The increased O/Cu ratio after the long-term THS test can be explained by the formation of a galvanic cell [20], as shown schematically in Fig. 5.6. When Cu_2O begins to form among the defective areas of SLG, a galvanic cell is formed. The electron donated by Cu atom during oxidation can be transferred via graphene sheet to air, thereby promoting further Cu oxidation at SLG defects and grain boundaries. The results indicate that the oxidation rate of the bare Cu surface decreased after long-term THS test because no galvanic cell was formed to accelerate the Cu corrosion.

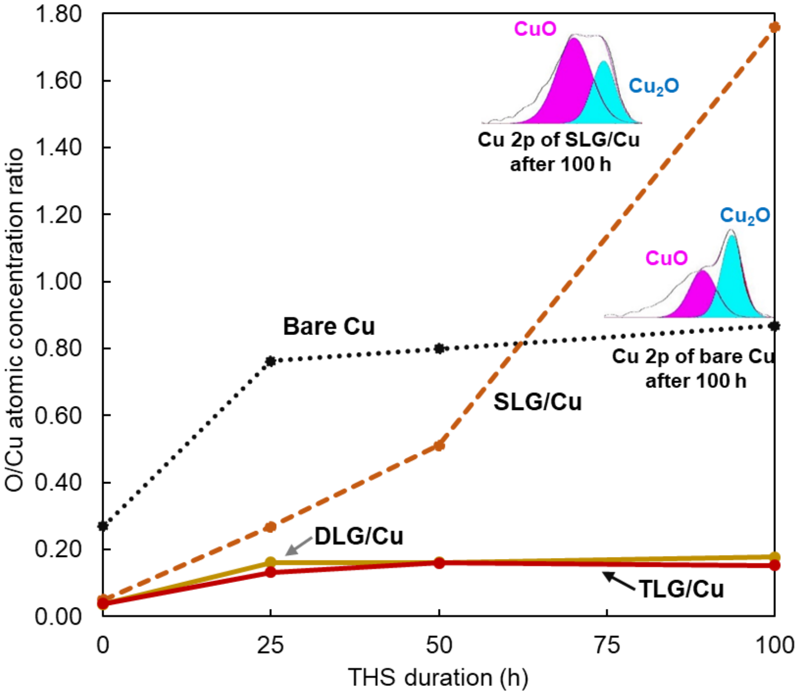

Figure 5.5 Relative O/Cu atomic concentration ratios of the bare Cu and graphene-coated Cu surfaces measured before and after different durations of THS test.

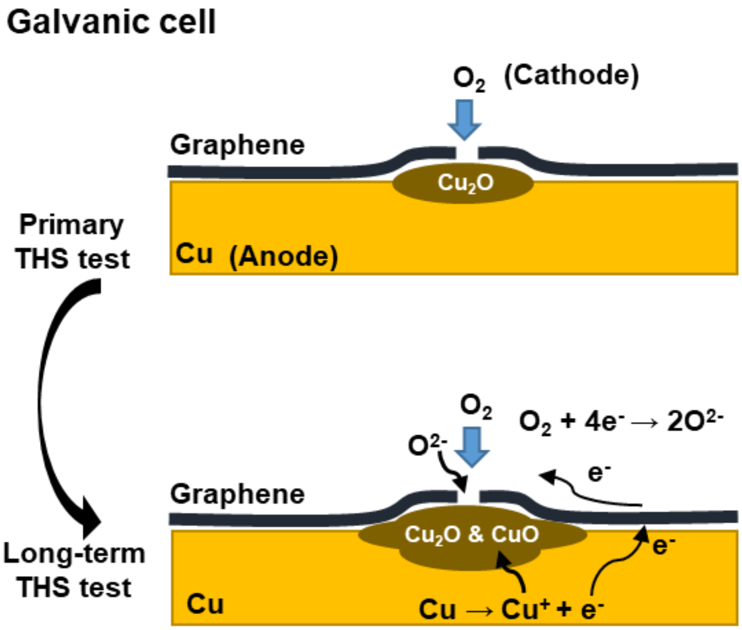

Figure 5.6 Schematic model showing the formation of a galvanic cell among the defective areas of graphene over the Cu surface.

As expected, DLG-coated Cu surface exhibited larger shiny areas after long-term THS test [Fig. 5.3(j–l) and (n-p)] because the penetration of O atom through the SLG defects and grain boundaries was obstructed by the multiple stacking of SLG layer. Little change was observed in the XPS spectrum of DLG-coated Cu during 100 h of THS test [Fig. 5.4(A3)], indicating good protective ability. In order to explain how the upper SLG layer protects the areas of SLG grain boundaries or defects underneath, Fig. 5.7 shows the simulated energy barrier to water migration through the overlapped SLG sheets. In the first-principle simulation, migrating water moved from the middle-right side to the left side of both graphene layers, and water migrates along the migration coordinate via the edge site and ends up among the overlapped SLG sheets [Fig. 5.7(a)]. The simulation results indicate that the energy barrier (*E*) to water migration was higher when the length of the graphene overlapping (d) was 1.22 to 3.66 Å [Fig. 5.7(c–e)] comparing to the scenario with no overlapping [d = 0 Å; Fig. 5.7(b)]. The results indicate that SLG overlapping was essential to improve the barrier efficiency.

However, small dark spots of Cu_2O and CuO were still observed on some areas of the DLG-coated Cu surface, as indicated by OM [Fig. 5.3(j–l)]. These tiny dark spots, which were almost similar in size, likely corresponded to the intersection between the upper and lower SLG grain boundaries, as shown in the schematic model in Fig. 5.8. The O atom can penetrate through these holes to oxidize the Cu surfaces. The number of small dark spots on the TLG-coated surface after 100 h of THS test [Fig. 5.3(n–p)] was drastically reduced compared to the DLG-coated Cu surface [Fig. 5.3(j–l)] owing to the efficient barrier of the stacked SLG layers covering on the defects of the lower SLG layers. The Cu 2p spectrum and O/Cu ratio of the TLG-coated Cu surface did not change significantly during THS test [Figs. 5.4(A4) and 5.5], confirming the ability of TLG to prevent the oxidation of the Cu surface by moisture. Overall, the findings demonstrate that stacking graphene layers can effectively prevent the moisture diffusion through the SLG defects and grain boundaries of the lower graphene layers.

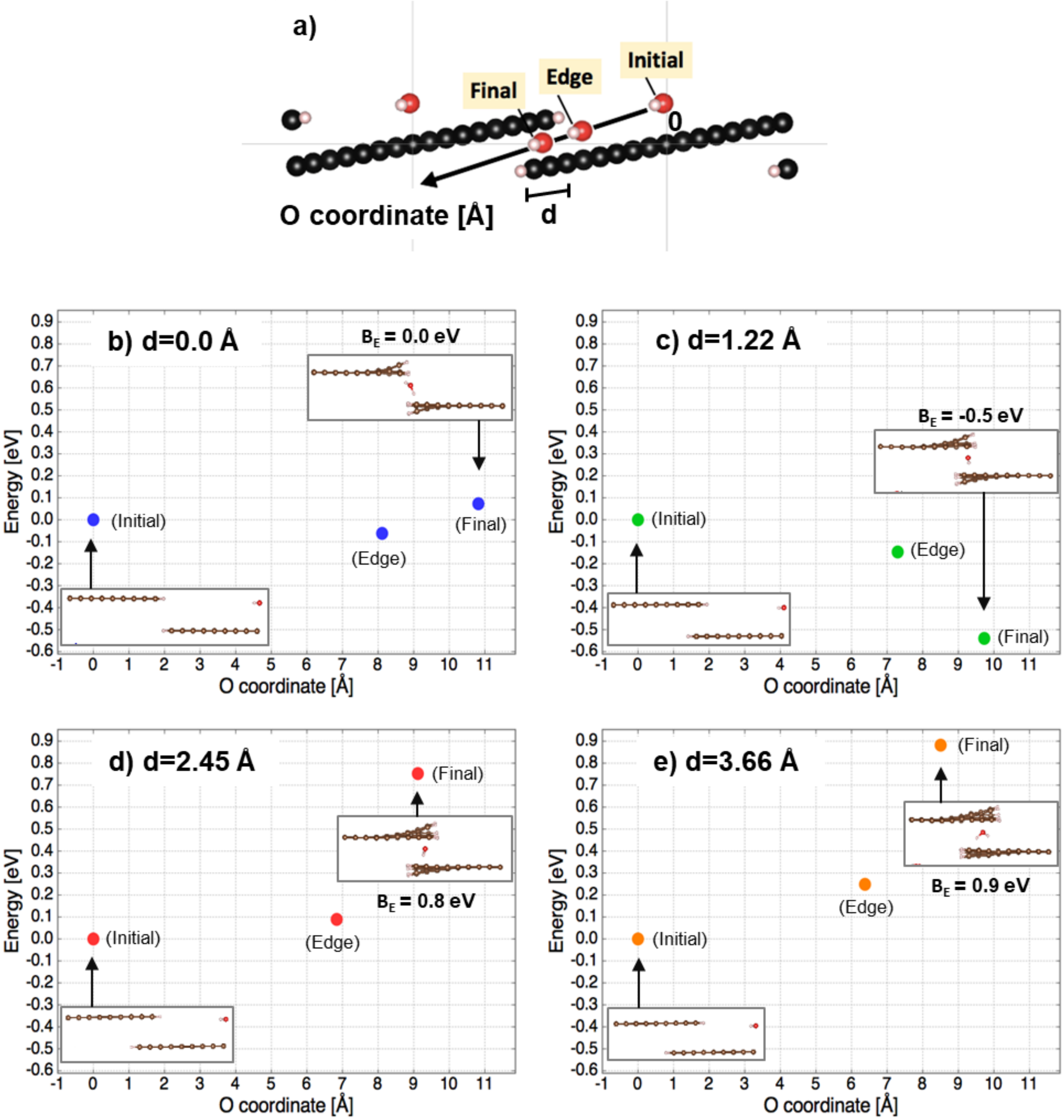

Figure 5.7. Optimized geometry and energy of water migration through overlapping areas of two SLG sheets [5].

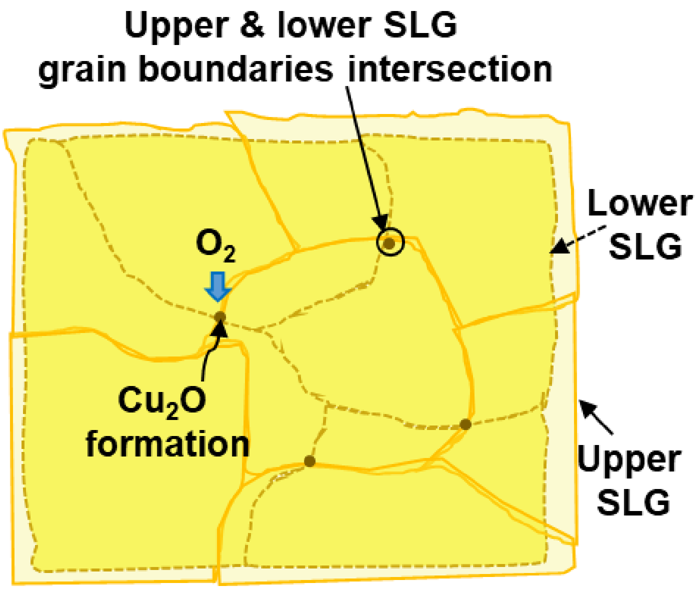

Figure 5.8. Schematic model showing the potential cause of Cu oxidation on the DLG-coated Cu surface.

5.4. Summary and conclusions

The improvement of graphene-coated Cu should be adopted to prevent the oxidation on the Cu surface and also to eliminate the galvanic cell formation, which enhances the Cu oxidation in long-term storage. Stacking SLG on the SLG-coated Cu surface was performed to cover defects and grain boundaries of the underlying SLG layer. Long-term THS test (100 h) was carried out under the accelerated conditions of 85°C and 85% RH to evaluate the effectiveness of the graphene coatings in preventing oxidation. The results reveal that stacking SLG as DLG was an efficient barrier against O atom diffusion, although some tiny areas of Cu were still oxidized at the cross-point of grain boundaries between the upper and lower SLG layers. Further stacking as TLG can preserve the Cu film surface in long-term THS test. A typical simulation of O atoms diffusion through the overlapping SLG sheets indicates that the energy barrier against O atoms diffusion was higher with increasing the range of graphene overlapping. Based on the measurement and simulation results, multiple-stacking SLG layers can cover the underneath grain boundaries and defects. The findings demonstrated that stacking large-grained SLG is a promising strategy for improving the moisture barrier properties of graphene on Cu film surface.

References

[1] P. Y. Huang, C. S. Ruiz-Vargas, A. M. van der Zande, W. S. Whitney, M. P. Levendorf, J. W. Kevek, S. Garg, J. S. Alden, C. J. Hustedt, Y. Zhu, J. Park, P. L. McEuen, and D. A. Muller, Nature **469**, 389 (2011).

[2] H. Ago, K. Kawahara, Y. Ogawa, S. Tanoue, M. A. Bissett, M. Tsuji, H. Sakaguchi, R. J. Koch, F. Fromm, T. Seyller, K. Komatsu, and K. Tsukagoshi, Appl. Phys. Express **6**, 075101 (2013).

[3] B. Hu, H. Ago, Y. Ito, K. Kawahara, M. Tsuji, E. Magome, K. Sumitani, N. Mizuta, K.-I. Ikeda, S. Mizuno, Carbon **50**, 57 (2012).

[4] Y. Takesaki, Kenji Kawahara, H. Hibino, S. Okada, M. Tsuji, and H. Ago, Chem. Mater. **28**, 4583 (2016).

[5] K. Yasuraoka, M. Maruyama, and S. Okada, Int. Microprocesses and Nanotechnology Conf., 2018.

[6] A.-Y. Lu, S.-Y. Wei, C.-Y. Wu, Y. Hernandez, T.-Y. Chen, T.-H. Liu, C.-W. Pao, F.-R. Chen, L.-J. Li, and Z.-Y. Juang, RSC Adv. **2**, 3008 (2012).

[7] A. C. Ferrari, J. C. Meyer, V. Scardaci, C. Casiraghi, M. Lazzeri, F. Mauri, S. Piscanec, D. Jiang, K. S. Novoselov, S. Roth, and A. K. Geim, Phys. Rev. Lett. **97**, 187401 (2006).

[8] S. He, S. Amoruso, D. Pang, C. Wang, and M. Hu, J. Chem. Phys. **144**, 164703 (2016).

[9] X. Yin, Y. Li, F. Ke, C. Lin, H. Zhao, L. Gan, Z. Luo, R. Zhao, T. F. Heinz, and Z. Hu, Nano Res. **7**, 1613 (2014).

[10] Y. Deng, A. D. Handoko, Y. Du, S. Xi, and B. S. Yeo, ACS Catal. **6**, 2473 (2016).

[11] N. Tounsi, A. Barhoumi, F. C. Akkari, M. Kanzari, H. Guermazi, S. Guermazi, Vacuum **121**, 9 (2015).

[12] S. Poulston, P. M. Parlett, P. Stone, and M. Bowker, Surf. Interface Anal. **24**, 811 (1996).

[13] J. Iijima, J.-W. Lim, S.-H. Hong, S. Suzuki, K. Mimura, and M. Isshiki, Appl. Surf. Sci. **253**, 2825 (2006).

[14] B. Luo, P. R. Whelan, A. Shivayogimath, D. M. A. Mackenzie, P. Bøggild, and T. J. Booth, Chem. Mater. **28**, 3789 (2016).

[15] D. Tahir and S. Tougaard, J. Phys.: Condens. Matter **24**, 175002 (2012).

[16] M. Galbiati, A. C. Stoot, D. M. A. Mackenzie, P. Bøggild, and L. Camilli, Sci. Rep. **7**, 39770 (2017).

[17] K. Ueno, V. M. Donnelly, Y. Tsuchiya, J. Vac. Sci. Technol., B **16**, 2986 (1998).

[18] A. I. Aria, P. R. Kidambi, R. S. Weatherup, L. Xiao, J. A. Williams, and S. Hofmann, J. Phys. Chem. C **120**, 2215 (2016).

[19] Y. Cong, X. Li, Y Qina, Z. Dong, G. Yuan, Z. Cui, and X. Lai, Appl. Catalysis B: Environmental **107**, 128 (2011).

[20] L. Shen, Y. Zhao, Y. Wang, R. Song, Q. Yao, S. Chen, and Y. Chai, J. Mater. Chem. A **4**, 5044 (2016).

CHAPTER 6

NITROGEN-DOPED AMORPHOUS CARBON FOR PRACTICAL MOISTURE BARRIER

6.1. Introduction

As described in chapter 5, graphene is expected as a candidate for an ultra-thin barrier for Cu metallization, however, high-temperature processes were still not appropriate for the current LSIs fabrication [1,2]. To approach this goal, a-C:N material, which can be fabricated at room temperature by sputtering, seems to be a potential moisture barrier to against Cu oxidation.

In this chapter, the moisture barrier properties of the sputtered a-C:N with various nitrogen contents were investigated by comparison to a-C-coated Cu and bare Cu surfaces under the THS test. Surface color observation and sheet resistance measurement were carried out to evaluate the physical change of sample surfaces. Further study by surface morphology observation and chemical state analysis were performed to confirm the efficiency of a-C:N against Cu oxidation in more detail and the potential mechanisms of this method were also discussed in this chapter.

6.2. Experimental methods

For the preparation of Cu film sample, 100-nm-thick Cu film was deposited on SiO_2/Si substrate by DC-magnetron sputtering at 200°C to complete the Cu grain growth. Then, N-doped a-C layer was deposited on the Cu surface by RF-magnetron sputtering from a graphite target in the gas mixture of Ar and N_2 at room temperature for 537 s. Different Ar:N_2 gas flow ratios; 90:10, 80:20, and 70:30, were performed to investigate the relative changes of a-C:N mixed composition and their efficiency of moisture barrier. After sample preparations, the cross-sectional area of a-C:N layer was observed to measure the precise film thickness by TEM. Then, existence of a-C and N atoms were analyzed using XPS with ~110-μm diameter of Al X-ray source (1486.6 eV), voltage 15 kV, and current 5 mA.

Then, THS test was carried out under the conditions of 85°C/85% RH to accelerate the oxidation of Cu surface for 100 h. Primary investigation was conducted by observing the change of surface color and measuring the sheet resistance using an OM and a four-probe method, respectively. Further investigation was performed to observe the change of surface morphology using SEM comparing before and after the THS test. Moreover, XPS depth profiling was performed after 100 h of the THS test to investigate the oxidation of Cu surface below a-C:N layer by using Ar+ ion beam etching with a beam energy of 4 keV scanned over an area of 2 mm×2mm for 50 s per cycle then measured by XPS after each cycle and obtain the relative atomic concentration ratios of N, C, O, and Cu elements.

6.3. Results and discussion

6.3.1. Film characteristics measured by TEM and XPS

Figure 6.1(a) shows the structural illustration of a-C:N-coated Cu surface. The thickness of sputtered a-C:N layer was measured as ~15 nm for the a-C:N 90:10 and ~25 nm for 70:30 samples by the cross-sectional TEM image, as shown in Fig. 6.1(b–c). It was found that the increase of the N_2/Ar gas flow ratio had an effect on the growth rate of a-C:N layer. The obtained results are in accord with the previous report of Kamiyama et al. [3]. Large surface roughness in case of a-C:N 70:30 [Fig. 6.1(c)] was considered to be caused by the large Cu roughness probably due to stress from the substrate heating during Cu sputtering at 200°C. Although the interfacial diffusion between Cu and a-C:N [Fig. 6.1(c)] seemed to be a potential effect on this surface roughness, the TEM images evidently indicate that the a-C:N layer uniformly covered all the Cu surface.

All three conditions of a-C:N samples were characterized the compositions of C–N bonds from the curve fitting of C 1s XPS spectra, as shown in Fig. 6.2(a–c). The peaks located at the binding energies of 284.5 and 285.5 eV were corresponded to sp^2- and sp^3-hybridized bonds [4,5], respectively. The binding energies of 286-286.8 and 287-287.8 were corresponded to the bonding of sp^2C–N and sp^3C–N [6,7], respectively. Owing to the lower formation energy of the sp^2C-N bond, most N atoms were bound to sp^2C rather than sp^3C atoms [8]. For the lowest N-doping (a-C:N 90:10), C–C bonds from sp^2 and sp^3 were still be the dominant composition in C 1s spectra. Main composition became C–N bonds in the cases of higher N-doping. The relative atomic concentration ratios of N to C are shown in Fig. 6.2(d). It indicates that the increase of N concentration was obtained from the higher flow rate of N_2 gas during sputtering. N concentration was increased double with the increase of N_2 gas flow rate from a-C:N 90:10 to 80:20. However, the existent N concentration seemed to be lower than expected in the case of a-C: N 70:30.

6.3.2. Efficiency verification of a-C:N against oxidation after THS test

6.3.2.1. Evolution of normalized sheet resistance measured by four-probe method

Based on the decrease of Cu film thickness by oxidation leading to the sheet resistance increase, it was considered to detect the oxidation of the Cu surface. The sheet resistance of each sample (two samples/condition) was measured before and after 50 and 100 h of the THS test and then normalized by its initial value before test, as shown in Fig. 6.3.

The evolution of R indicates the large increase for the bare Cu samples. In contrast, the change of sheet resistance was much smaller for the samples of a-C:N-coated Cu. R was almost the same as the beginning for the lowest N-doping (a-C:N 90:10). For both cases of the higher N-doping, their R was slightly increased. These results reveal that the lowest N-doping (a-C:N 90:10) can protect the Cu surface from oxidation through 100 h of the THS test. Although the efficiency of the oxidation barrier was lower for other cases, the increasing rate of R was much lower than that of the bare Cu surface.

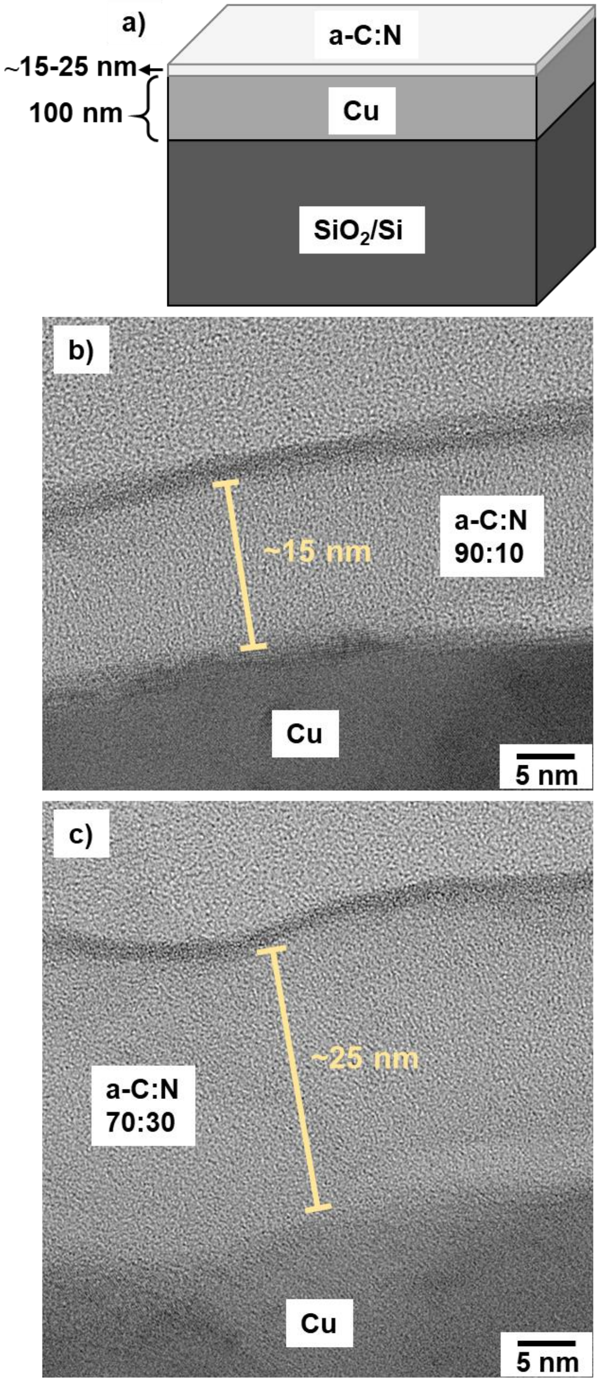

Figure 6.1. (a) Schematic illustration of a-C:N-coated Cu sample and cross-sectional TEM image of a-C:N layer grown on Cu surface for a-C:N ratios of (b) 90:10 and (c) 70:30.

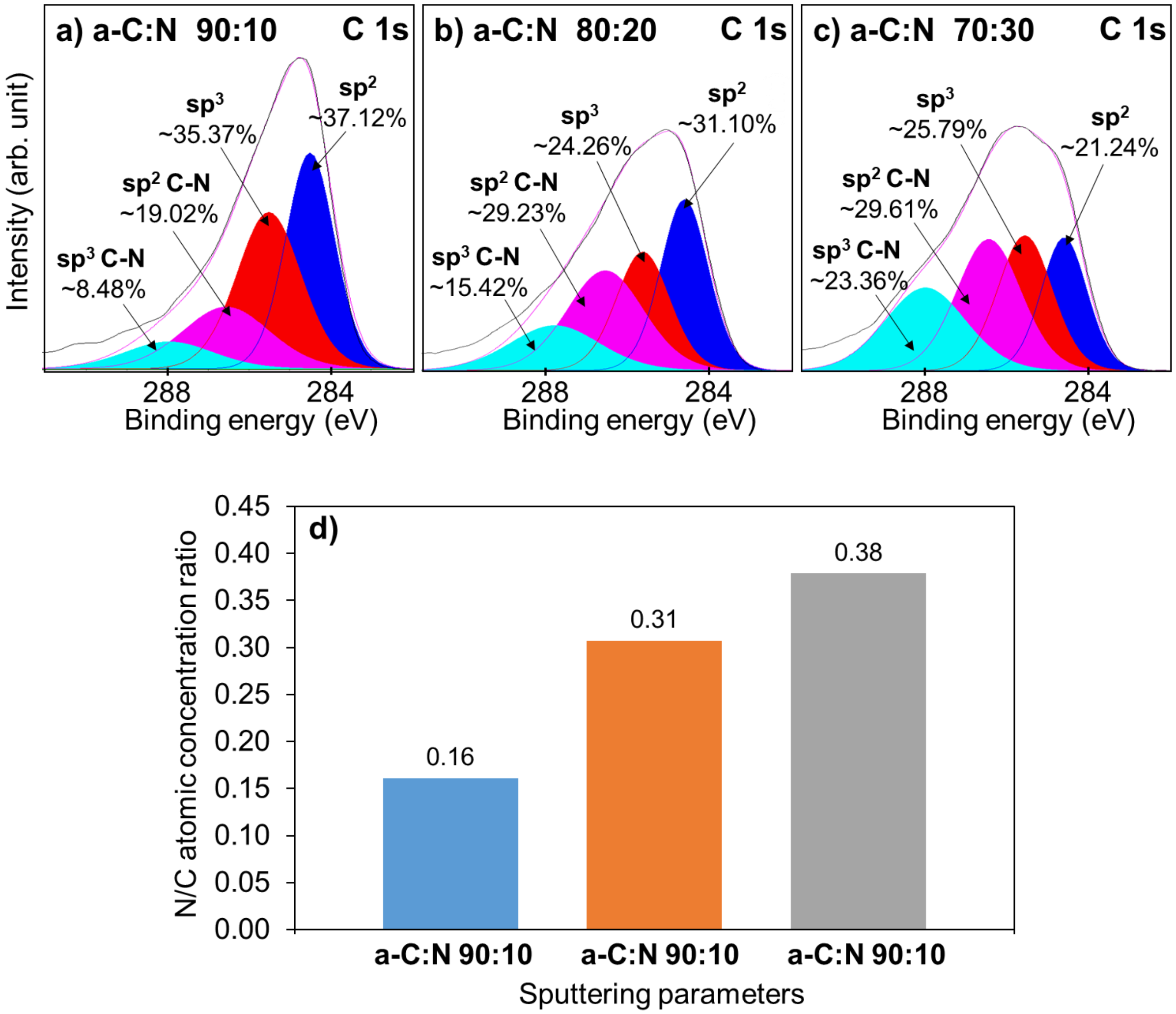

Figure 6.2. C 1s XPS spectra of different a-C:N ratios; (a) 90:10, (b) 80:20, and (c)70:30 and (d) relative atomic concentration ratios of N/C measured on the sample surface.

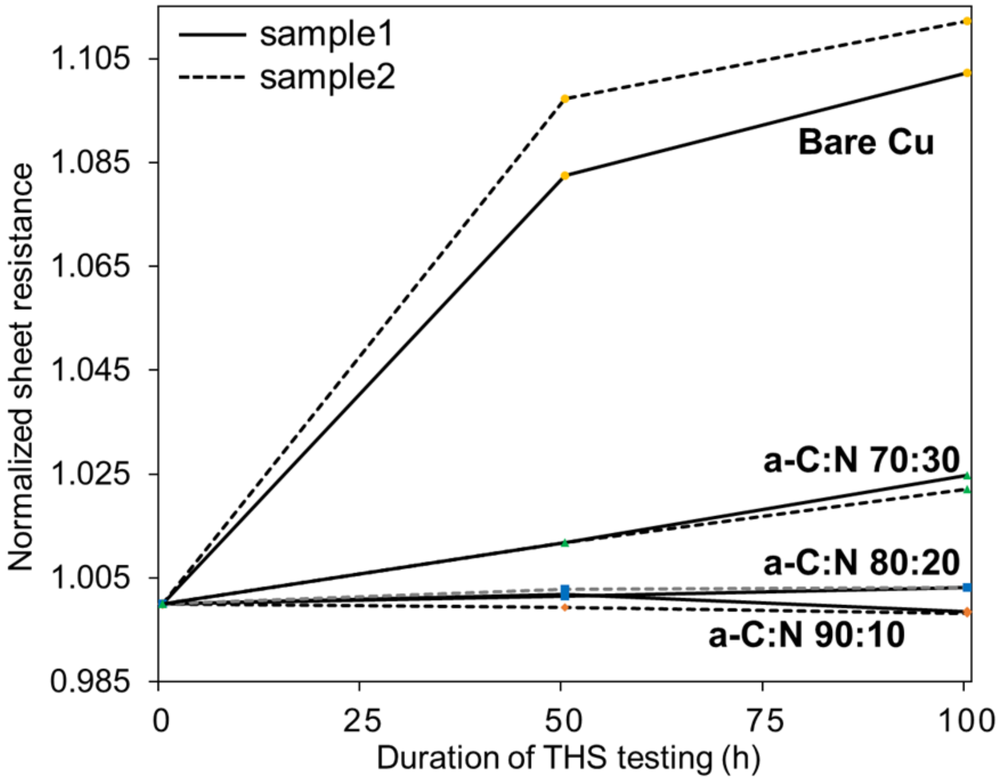

Figure 6.3. Evolution of normalized sheet resistance (*R*) measured on the top surface of all samples measured before and after 50 and 100 h of THS test.

6.3.2.2. Change of surface color observed by OM

At the beginning (0 h), surfaces of the a-C:N-coated Cu samples [Fig. 6.4(b–d)] were typically darker than that of the bare Cu sample [Fig. 6.4(a)]. These color change implied the formation of Cu oxidation. After the THS test (100 h), the surface color of the bare Cu was inherently changed to darker color after exposure to the air, as shown in Fig. 6.4(e). For all cases of the a-C:N coated Cu samples, the surface of the lowest N-doping (a-C:N 90:10) was almost no change along with the THS test [Fig. 6.4(b–f)], and it accorded with the result of almost no increase of *R* as described in Fig. 6.3. At the same time, both cases of the higher N-doping changed their surfaces' color to darker color than those of the beginning [Fig. 6.4(g–h)]. Further analyses were performed to confirm the efficiency of a-C:N 90:10 case and to evaluate the qualitative differences for both cases of the higher N-doping comparing to that of the bare Cu sample.

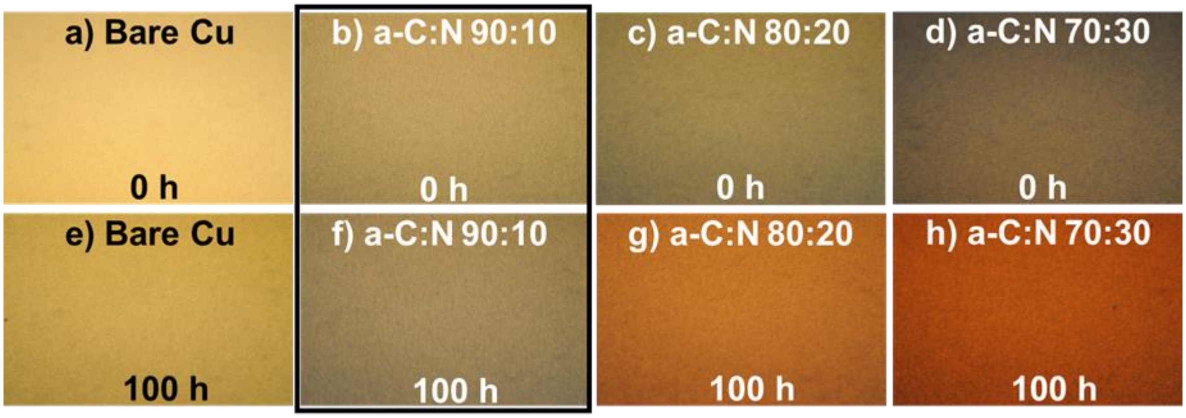

Figure 6.4. Optical images observed on the top surface of all samples comparing between before (a)–(d) and after 100 h (e)–(h) of THS test.

6.3.2.3. Change of surface morphology observed by SEM

Beyond the observation of surface color by OM, surface morphology observation by SEM was also carried out to identify the difference of film features for various conditions of a-C:N comparing between before and after the THS test, as shown in Fig. 6.5. They indicate that there was no significant difference of the surface features for all samples after the deposition in spite of the different concentration of C–C and C–N bonds, as shown in Fig. 6.5(a–c). After 100 h of the THS test, there was no change of the film feature for the lowest N-doping case [Fig. 6.5(d)] comparing to that of the beginning [Fig. 6.5(a)]. For the higher N-doping, a-C:N 80:20 case was found few holes in some areas of the sample surface [Fig. 6.5(e)] and more number of holes were observed for a-C:N 70:30 with a diameter of each spot ~100 nm [Fig. 6.5(f)]. The formation of holes during the THS test was considered as the reason for Cu oxidation for the higher N-doping. It is possible that the dominant composition of C–N bonds from a-C:N 70:30, as shown in Fig. 6.2(b–c), provided a weak barrier against moisture diffusion. During the THS test, moisture diffusion can damage this barrier and penetrate to oxidize the Cu surface underneath, showing a slight increase of R and darker surface color. Even though the Cu surface seems very rough on SEM images, all over the Cu surface was covered with 15-nm thickness a-C:N layer, as displayed in Fig. 6.1(b). It reveals that adopting a smooth surface of Cu would be able to reduce the film thickness of a-C:N further.

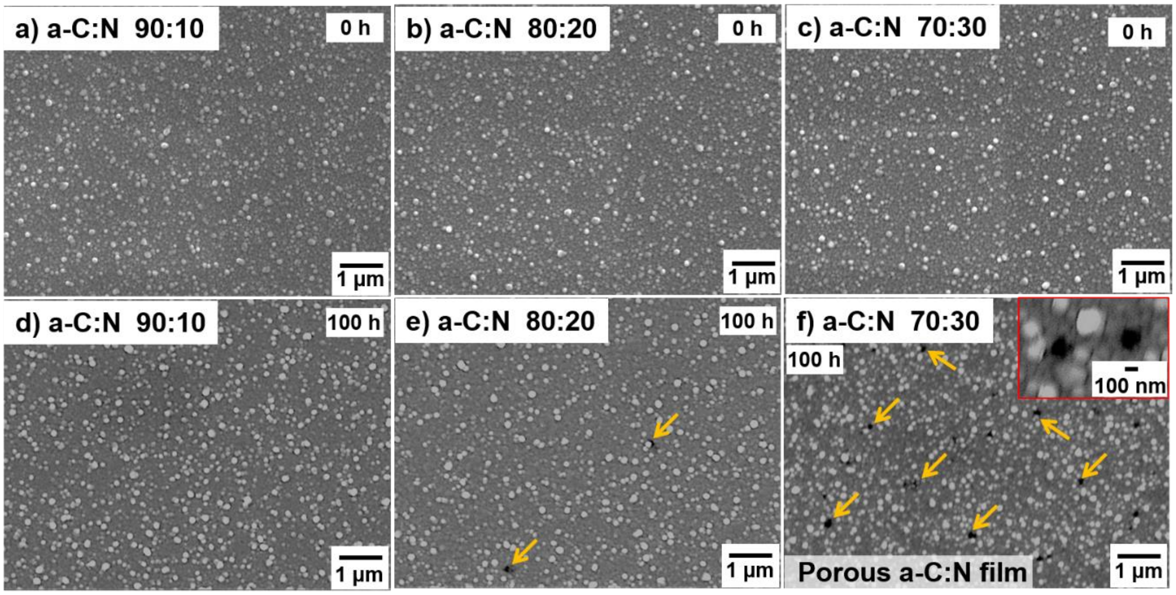

Figure 6.5. Surface morphology observation by SEM for a-C:N samples comparing between before (a)–(c) and after 100 h (d)–(f) of THS test.

6.3.2.4. XPS depth profiling

To clearly investigate the oxidation of Cu surface, XPS depth profiling was conducted after 100 h of the THS test to obtain the compositional depth profiles comprising of C, N, O from Cu_2O+CuO and Cu atoms, as shown in Figs. 6.6 and 6.7. Depth profiling of the bare Cu sample was also carried out for comparison. Firstly, a typical depth profile exhibited the sample structure including the SiO_2/Si substrate, as shown in Fig. 6.6. It confirmed that the O diffusion from the SiO_2 substrate did not affect the Cu surface since there was no O diffusion from the SiO_2 which reached the Cu surface.

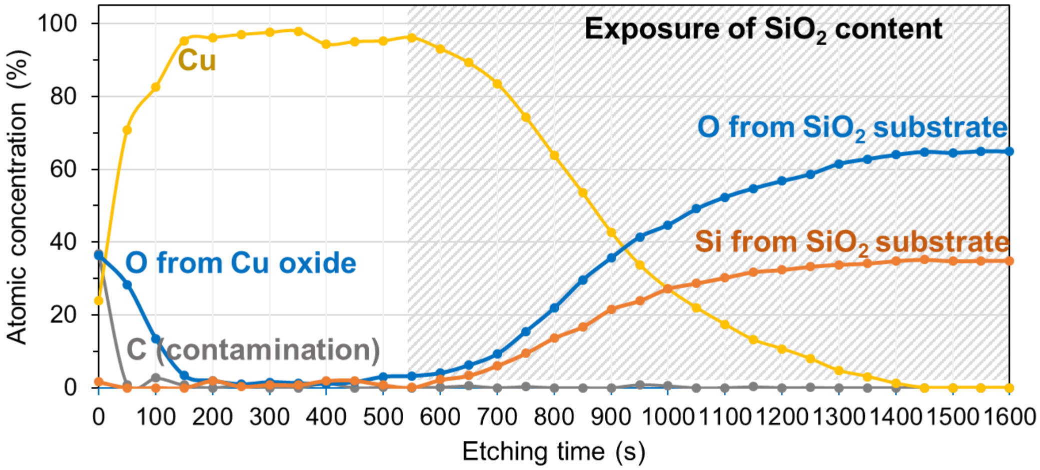

Figure 6.6 XPS depth profile of bare Cu after 100 h of THS test, which comprising of C, N, O, Cu, and Si atoms.

The depth profile of bare Cu, as shown in Fig. 6.7(a), indicates that the Cu surface was highly oxidized by moisture, as showing very large contents of oxidation (~27% of O at the maximum point and the depth corresponding to ~150 s of etching time). Fig. 6.8(a) shows the Cu 2p XPS spectra measured before and after Ar etching. It reveals that the large content of CuO, which located at ~933.6 eV and 944.6–942.4 eV for CuO shake-up peak, was formed on the top surface of bare Cu. After Ar+ etching, it indicates the dominant structure of Cu_2O located at ~932.4 eV.

For all cases of a-C:N coating [Fig. 6.7(b–d)], there were no Cu oxidation under a-C:N layer and it was found only few Cu contents on the top surface. In addition, O atoms from the moisture were considered to adsorb on the surface of a-C:N, as shown in the inset of O 1s spectra [Fig. 6.7(b–d)]. Further analysis of Cu 2p spectra [Fig. 6.8(b–d)] reveal that few Cu atoms diffused through a-C:N layer and they were oxidized by the adsorbed water on the top surface to form the dominant structure of $Cu(OH)_2$, which located at ~934.6 eV, as shown in the insets for all cases of a-C:N [Fig. 6.8(b–d)]. Cu 2p spectra measured on the upper layer of the a-C:N 70:30 layer [Fig. 6.8(d)] were found a high content of Cu_2O due to the higher diffusion of Cu atoms into a-C:N than that of other cases. The deposited films at higher N_2 gas flow, as a-C:N 70:30, are considered to less stable against moisture by showing the pores during THS test because of the chemical composition which included more C–N bonds, as shown in Fig. 6.2(b–c), in spite of the thicker film thickness, as ~25 nm for a-C:N 70:30 measured by TEM.

In the case of a-C coating [9], O atoms penetrated through the a-C layer to oxidize Cu surface after the long-term test as 100 h [Fig. 6.7(e)]. Cu 2p XPS spectra measured after Ar etching [Fig. 6.8(e)] reveal that low oxidation state of Cu_2O was formed on the Cu surface underneath the a-C layer.

These results can confirm the efficiency of a-C:N to prevent the oxidation of Cu surface, especially less N-doping as a-C:N 90:10. It can be a guideline for the future development of the thinner a-C:N layer.

6.3.3. Mechanism of preventing Cu oxidation with a-C:N layer

Regarding the testing results, doping just 10% N_2 flow during sputtering can enhance the efficiency of a-C layer against Cu oxidation. Although few Cu atoms diffused into a-C:N layer and they were oxidized by the adsorbed O atoms on the top surface of a-C:N, these O atoms could not reach the Cu layer below a-C:N layer. These phenomena can be described from a potential perspective based on the chemical properties and testing results, as shown in Fig. 6.9. According to the controlled moist air (85°C/85%RH), Cu oxidation, which generated from the reaction of Cu with both O_2 and H_2O to form Cu_2O, CuO, and $Cu(OH)_2$, leads to the increase of Cu sheet resistance [10–14]. However, the formations of Cu_2O and CuO are more immediately begun after exposure to ambient air and it most commonly happens in real usage with lower humidity [13,14]. Since H_2O was detected only near the a-C:N surface as shown in Fig. 6.8, O atoms were considered as the diffusion species through the a-C:N layer. From the previous report [9], C atoms played an important role to decelerate the downward diffusion of O atoms, but bare a-C was not sufficient yet to prevent the diffusion of O atoms for a long-term test [Fig. 6.7(e)]. It was found that the Cu_2O layer was formed deeply, as an illustrated model in Fig. 6.9(a), according to the XPS depth profile [Fig. 6.7(e)]. Further study will be required to describe the mechanism for deep diffusion of O through a-C layer to oxidize Cu. An appropriate composition of N-doped a-C can suppress the diffusion of O atoms by enhancing the efficient barrier to prevent the diffusion of O atoms in regard to the film density and the mutual electrostatic repulsion between N and O atoms resulting from their strong electronegativity (3.04 for N and 3.44 for O) [15], as an illustrated model in Fig. 6.9(b).

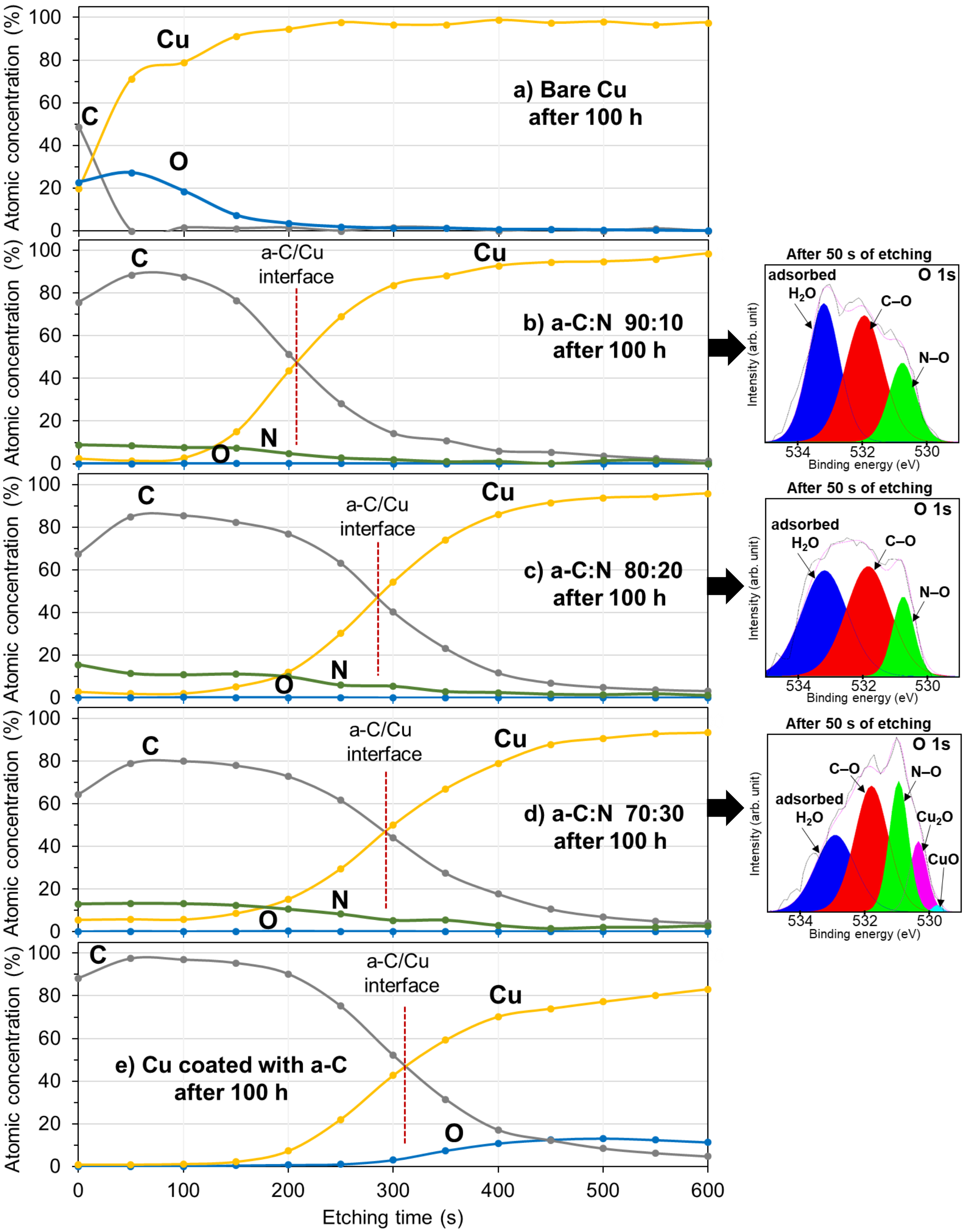

Figure 6.7. XPS depth profiles of (a) bare Cu, (b) a-C:N 90:10, (c) a-C:N 80:20, (d) a-C:N 70:30, and (e) the previous report of a-C coating on Cu surface [9].

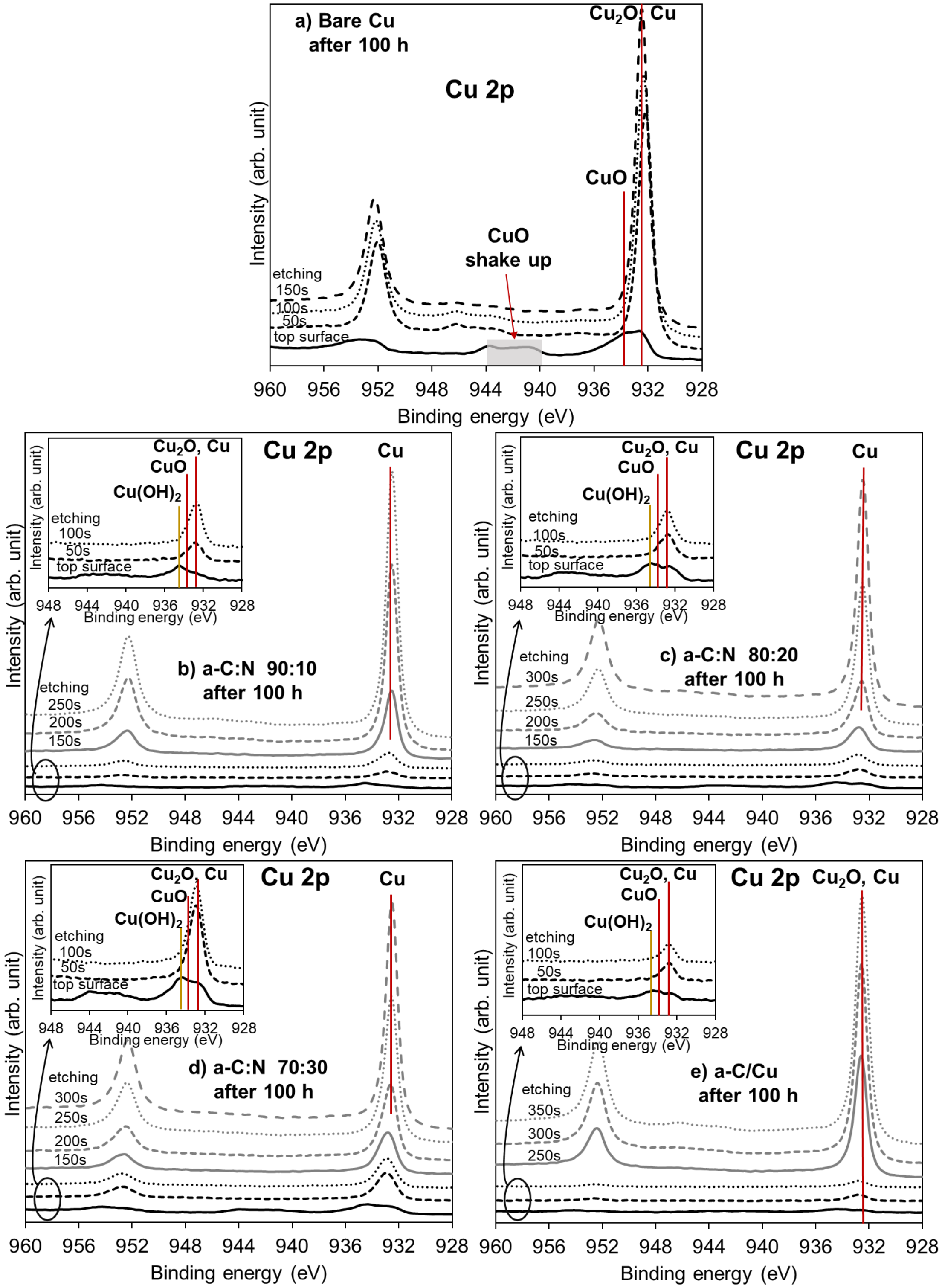

Figure 6.8. Cu 2p XPS spectra of (a) bare Cu, (b) a-C:N 90:10, (c) a-C:N 80:20, (d) a-C:N 70:30, and (e) a-C coating on Cu surface [9] measured before and after each cycle of Ar etching.

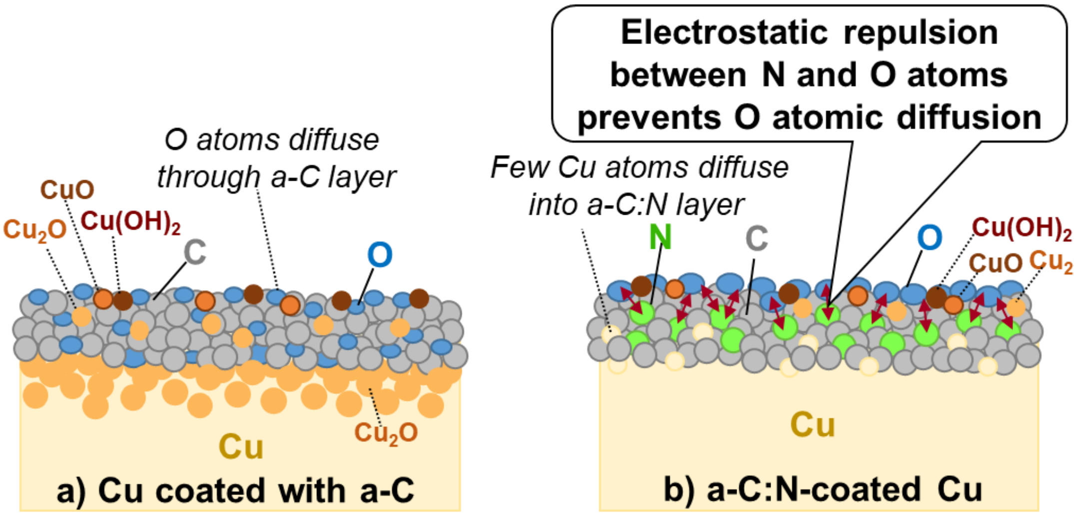

Figure 6.9. Model to explain the effect of N-doping on moisture barrier improvement, (a) a-C without N-doping and (b) a-C:N layer on Cu surface.

6.4. Summary and conclusions

In this chapter, the excellent barrier properties of the sputtered a-C:N layer against moisture was demonstrated to prevent the oxidation of Cu surface. a-C:N film was deposited by sputtering of graphite target in Ar/N_2 ambient at room temperature on the Cu surface, so the thermal budget is compatible with the present processes. The a-C:N material, especially at a sputtering gas ratio of 90:10 (Ar:N_2), can perform as an efficient moisture barrier for preventing the Cu oxidation by showing almost no change of sheet resistance, surface color, and film feature along with 100 h of the THS test under the condition of 85°C/85% RH (~400 years at 27°C/60% RH). XPS depth profiles imply almost no Cu oxidation on the Cu surface below a-C:N layer. The a-C:N layer with appropriate Ar:N_2 conditions can suppress the penetration of O atoms with the potential effects of the strong electrostatic repulsion between N and O atoms and the film density. Because the low-temperature process is compatible with SM fabrication, it would be a practical method to improve the reliability of Cu metallization for long-term storage over 100 years as expected.

References

[1] P. Gomasang, T. Abe, K. Kawahara, Y. Wasai, N. Nabatova-Gabain, N. T. Cuong, H. Ago, S. Okada, and K. Ueno, Jpn. J. Appl. Phys. **57**, 04FC08 (2018).

[2] P. Gomasang, K. Kawahara, K. Yasuraoka, M. Maruyama, H. Ago, S. Okada, and K. Ueno, Sci. Rep. **9**, 3777 (2019).

[3] H. Kamiyama and O. Takai, Trans. Mat. Res. Soc. Jpn. **44,** 45 (2019).

[4] A. P. Dementjev, A. de Graaf, M. C. M. van de Sanden, K. I. Maslakov, A. V. Naumkin, and A. A. Serov, Diam. Relat. Mater. **9**, 1904 (2000).

[5] J. W. Suk, S. Murali, J. An, and R. S. Ruoff, Carbon **50**, 2220 (2012).

[6] S. Xu, S. Kumar, Y. A. Li, N. Jiang, and S. Lee, J. Phys. Condens. Matter **12**, L121 (2000).

[7] K. Yamamoto, Y. Koga, S. Fujiwara, F. Kokai, J. I. Kleiman, and K. K. Kim, Thin Solid Films **339**, 38 (1999).

[8] S. Pöykkö, M. Kaukonen, M. J. Puska, and R. M. Nieminen, Comput. Mater. Sci. **10**, 351 (1998).

[9] P. Gomasang and K. Ueno, Ext. Abstr. Solid State Device and Materials, 2019, p.717.

[10] P. Gomasang, S. Ogiue, S. Yokogawa, and K. Ueno, Jpn. J. Appl. Phys. **58,** SBBC01 (2019).

[11] P. Gomasang, S. Ogiue, K. Ueno, and S. Yokogawa, Proc. IEEE Int. Interconnect Technology conf., 2018, p.112.

[12] T. Fujikawa and T. Yoshikawa, Jpn. J. Appl. Phys. **40**, 1522 (2001).

[13] I. Platzman, R. Brener, H. Haick, and R. Tannenbaum, J. Phys. Chem. C **112**, 1101 (2008).

[14] T. Tamai, IEICE Trans. on Electron. **E90-C**, 1391 (2007).

[15] H. R. Jiang, T. S. Zhao, L. Shi, P. Tan, and L. An, J. Phys. Chem. C **120**, 6612 (2016).

CHAPTER 7

CONCLUSIONS AND FUTURE PROSPECTS

7.1. Overall conclusions

Because of the small atomic radius of carbon, nanocarbon materials, such as graphene and a-C:N, were studied their potential and issues in preventing Cu-oxidation to improve the long-term reliability of Cu metallization used in LSIs, such as interconnects and bonding pads (expected >100 years). By studying graphene against Cu oxidation in principle, the results demonstrate that large-grained SLG is a potential moisture barrier. Nevertheless, areas with grain boundaries and defects create moisture diffusion paths. The results confirm that the stacking of SLG layers, as DLG and TLG, eliminates the grain boundaries. However, high-temperature CVD of SLG (~1000°C) is still not compatible with the current thermal budget of the fabrication process of LSIs. To reach the goal, a practical method of a-C:N-coated Cu, which can be deposited at room temperature by sputtering, was then investigated. The results show that the a-C:N layer with an optimized N-content is an efficient, practical barrier against moisture.

7.2. Conclusions for each chapter

7.2.1. Chapter 3

Because the Cu reliability in terms of protection against oxidation has rarely been studied, the fundamental characteristics of Cu oxidation under accelerated temperature and humidity conditions have been studied. Although the THS test was carried out under conventional conditions (85°C/85% RH), we studied the dependency on the temperature and humidity of Cu oxidation under varying humidity values (between 75% and 95% RH). The results show that the increase in the R at 85% RH is almost the same as that at 75% RH despite the higher oxidation state. The nonlinear phenomena can be explained with the relative volume of the Cu-oxidation states. The results suggest that conditions below 85°C/85% RH are more appropriate for the THS test of the Cu surface without a moisture barrier and lifetime prediction. In the appropriate range of the THS tests, the linear change of *R* depends on the temperature and humidity or vapor pressure; it is more sensitive to the temperature than the humidity. The XPS measurements confirm the increase in the oxidized Cu thickness with increasing *R*. In this chapter, a sample model for the prediction of the Cu lifetime is proposed based on the measured *R* value. It can be used as a guideline to generate a lifetime prediction model for Cu metallization and to improve their reliability in terms of moisture protection.

7.2.2. Chapter 4

The moisture barrier properties of a high-quality large-grained SLG coating on a Cu surface were studied in principle to improve the long-term reliability of Cu with respect to moisture protection. Standard THS test was carried out at 85°C/85% RH for 100 h to accelerate the oxidation of the Cu surface (which corresponds to ~400 years at 27°C/60% RH). The standard THS test can be used because it does not focus on the temperature and humidity dependency. The OM and XPS results obtained after the THS test indicate that large-grained SLG can protect the Cu surface from oxidation; only small areas of Cu close to SLG grain boundaries were oxidized. The first-principles simulation reveals that O atoms do not have enough energy to pass through the SLG structure. The SE was then used to evaluate the correlation between the oxidized Cu thickness and quality of SLG on the Cu surface. The results indicate that high proportions of graphite or graphene in combination with an optimized film structure can prevent the oxidation of the Cu surface. In addition, the a-C layer seems to be a potential moisture barrier based on the low amount of Cu oxidation in some areas. Based on the measurement results and simulation, the increase in the SLG grain size and elimination of grain boundaries are expected to improve the performance of the SLG layer in preventing Cu-oxidation by moisture.

7.2.3 Chapter 5

The formation of Cu-oxide in SLG areas with grain boundaries and defects was investigated by Raman and XPS in comparison with the Cu surface without a SLG barrier. The results after the THS test indicate that the Cu surface in SLG areas with grain boundaries and defects was significantly oxidized, showing a higher Cu-oxide content than the Cu surface without graphene. This is probably due to the formation of galvanic cells in these areas. Based on the long-term THS test (for >50 h at 85°C/85% RH), galvanic cells can induce a high amount of oxidation. In this chapter, a method is proposed to eliminate SLG grain boundaries and defects by stacking the SLG layers and forming DLG and TLG graphene coatings on the Cu surface. Stacking the SLG layers should be coated on Cu surfaces to prevent their oxidation and eliminate the formation of galvanic cells to achieve long-term storage reliability. Stacking of SLGs on the Cu surface was performed to cover the defects and grain boundaries of the underlying SLG layer. The test results reveal that DLG is an efficiently blocks O atom diffusion, although small areas of Cu were still oxidized at the cross points of grain boundaries between the upper and lower SLG layers. The TLG can be used to preserve the Cu film surface for long-term storage. These results were confirmed with a first-principles simulation. The results show that the energy barrier against O diffusion improves with increasing range of graphene film overlapping. Based on the experimental results and simulation, the stacking of large-grained SLG is a promising strategy for improving the moisture barrier properties of graphene-coated Cu film surfaces and long-term storage reliability over 100 years.

7.2.4. Chapter 6

Because the high thermal budget of SLG deposition is still not practical for the current fabrication process of LSIs, N-doped a-C, which can be deposited by room-temperature sputtering of the graphite target, was proposed to reach the goal. The a-C:N layer, especially that obtained at a sputtering gas ratio of 90:10 (Ar:N_2), is an excellent barrier against moisture. The sheet resistance, surface color, and film features insignificantly changed during a 100-hour THS test at 85°C and 85% RH. The XPS depth profiles imply almost no oxidation of the Cu surface underneath the a-C:N layer. The a-C:N layer with appropriate N contents potentially suppresses the penetration of O atoms because of the film density and the strong electrostatic repulsion between N and O atoms. Because the low-temperature process is compatible with LSI fabrication, room-temperature sputtering of a-C:N is a practical method that can be used to improve the reliability of Cu metallization in LSIs in terms of long-term storage (~400 years at 27°C/60% RH).

7.3. Future prospects

The application of large-grained SLG as Cu coating in LSIs will become feasible if an advanced fabrication process can be conducted with a low thermal budget. In addition, the deposition of defect-free SLG with large grains remains challenging.

The a-C:N is an excellent barrier that can be used to protect the Cu surface from oxidation and can be applied to Cu pads. However, the film thickness is still larger than expected. In the future, the film thickness of a-C:N is expected to be reduced and it leads to extend the applications. Furthermore, the potential cause of the electrostatic repulsion between N and O atoms, as speculated in this research, should be identified using simulations or other methods. The efficient a-C:N barrier is expected to be extensively used in other applications.

The obtained results in this research regarding graphene and a-C:N would be a guideline in the development of nanocarbon materials for moisture barrier films.